Title

Exploring protein-membrane interactions through simulation and experiment

Author

Tyagi, Vivek

Publication Date

2022

UNIVERSITY OF CALIFORNIA,
IRVINE

Exploring protein-membrane interactions through simulation and experiment

DISSERTATION

submitted in partial satisfaction of the requirements
for

DOCTOR OF PHILOSOPHY

in Materials Science & Engineering

by

Vivek Tyagi

Dissertation Committee:
Professor Regina Ragan, Chair
Professor Douglas J. Tobias
Assistant Professor Stacy Copp

2022

DEDICATION

To my mother and my sisters, constant sources of inspiration.

TABLE OF CONTENTS

LIST OF FIGURES

LIST OF TABLES

ACKNOWLEDGMENTS

I would like to thank Professor Douglas J. Tobias, Dr. J. Alfredo Freites. and Professor Medha M. Pathak for their continuous support throughout my research and studies. I would also like to acknowledge the generous computing time provided by UCI's high performance computing cluster HPC3, D. E. Shaw Research for their Anton 2 supercomputing cluster managed by the Pittsburgh Supercomputing Center (PSC), and all my funding sources including the R01 NS109810 grant and R01 Diversity Supplement. I would also like to thank my close collaborators and friends, including Alan Ly and Dr. Elianna S. Frank, I am very lucky to have their support.

VITA

Vivek Tyagi

EDUCATION

Doctor of Philosophy in Materials Science & Engineering **2022**
University of California, Irvine *Irvine, California*

Bachelor of Science in Materials Science & Engineering **2014**
University of Washington *Seattle, Washington*

RESEARCH EXPERIENCE

Graduate Research Assistant **2016–2022**
University of California, Irvine *Irvine, California*

TEACHING EXPERIENCE

Teaching Assistant **2016–2021**
University of California, Irvine *Irvine, California*

PEER-REVIEWED JOURNAL PUBLICATIONS

Single-particle tracking and machine-learning classification reveals heterogeneous Piezo1 diffusion **Dec 2022**
Biophysical Journal

Ca^{2+}-dependent interactions between lipids and the tumor-targeting peptide pHLIP **Aug 2022**
Protein Science

Effects of Cardiolipin on the Conformational Dynamics of Membrane-Anchored Bcl-xL **Aug 2021**
International Journal of Molecular Sciences

CONFERENCE PRESENTATIONS

Probing Piezo1 diffusion heterogeneity via single particle tracking and machine learning **Feb 2022**
Biophysical Society Meeting

ABSTRACT

Exploring protein-membrane interactions through simulation and experiment

By

Vivek Tyagi

Doctor of Philosophy in Materials Science & Engineering

University of California, Irvine, 2022

Professor Regina Ragan, PI

Protein/peptide interactions with cellular membranes are highly complex due to a myriad of membrane compositions and environmental variability. This research explores three protein-membrane systems. Bcl-xL, an anti-apoptotic protein that interacts with the mitochondrial outer membrane, is found to be regulated by both lipid composition and ionic conditions. A full-length Bcl-xL protein was built for simulation by combining two well-studied crystallographic structures, one of the soluble head and connective disordered loop, and another of the transmembrane helix which anchors the protein in the membrane. In conjunction with experimentalists, these simulations were able to illuminate the atomistic details of how Bcl-xL orients itself in the membrane and how different ionic conditions and protonation states of residues play a role in the conformation of Bcl-xL. In another study, pH Low Insertion Peptide, pHLIP, was prepared for simulation as a partially disordered structure in solution and as a transmembrane helix embedded in the membrane. These constructs explore changes in peptide conformation before insertion, and peptide orientation and interactions while inserted into the plasma membrane. The pHLIP peptide was shown to have stabilizing interactions between acidic residues and divalent cations in both scenarios. In particular, divalent cations played an important role in coordinating interactions between multiple negative charge centers. In a third study, Piezo1 membrane diffusion was explored by fluorescently tagging the ion channel and generating trajectories via total internal reflectance fluorescence

microscopy, an experimental procedure carried out through collaboration with the Pathak Lab at UCI. Analysis of these single particle tracks via machine learning revealed consistent anomalous diffusion and heterogeneity within the subdiffusive mobile class and changes specific to drug-based perturbations of the ion-channel-membrane system. These works are part of the development of a clear picture of membrane-protein interactions and would advance our understanding of how these interactions regulate different cellular processes.

Chapter 1

Effects of Cardiolipin on the Conformational Dynamics of Membrane-Anchored Bcl-xL

Vivek Tyagi, Victor Vasquez-Montes, J. Alfredo Freites, Alexander Kyrychenko, Douglas J. Tobias, and Alexey S. Ladokhin

1.1 Abstract

The anti-apoptotic protein Bcl-xL regulates apoptosis by preventing the permeation of the mitochondrial outer membrane by pro-apoptotic pore-forming proteins, which release apoptotic factors into the cytosol that ultimately lead to cell death. Two different membrane-integrated Bcl-xL constructs have been identified: a membrane-anchored and a membrane-inserted conformation. Here, we use molecular dynamics simulations to study the effect of the mitochondrial specific lipid cardiolipin and the protein protonation state on the confor-

mational dynamics of membrane-anchored Bcl-xL. The analysis reveals that the protonation state of the protein and cardiolipin content of the membrane modulate the orientation of the soluble head region (helices $\alpha1$ through $\alpha7$) and hence the exposure of its BH3-binding groove, which is required for its interaction with pro-apoptotic proteins.

1.2 Introduction

Apoptotic dysregulation is a common feature of many diseases and contributes to neurodegeneration, immunodeficiency, and cancer[41, 139, 151]. The anti-apoptotic protein Bcl-xL is a crucial component of this pathway as it blocks mitochondrial outer membrane permeabilization (MOMP), thereby preventing cell death[70, 11]. This is achieved by binding the pore-forming proteins BAX and BAK, resulting in non-productive oligomers that can no longer participate in promoting apoptosis[32, 140].

According to the "Embedded Together" model of MOMP regulation, the interactions between Bcl-xL and its target proteins occur on the mitochondrial outer membrane as this is where pore-forming proteins attach to initiate an apoptotic process (Figure 1.1A)[95, 82]. This requires the transition of Bcl-xL from an inactive state in the cytosol to an active state in the bilayer[12, 21]. Two different membrane-integrated forms of Bcl-xL have been identified in vitro: (1) an anchored conformation in which the C-terminal helix of Bcl-xL serves as a transmembrane anchor, while the remaining helices retain their soluble fold (Figure 1.1A, red)[178, 177, 126], and (2) a membrane inserted conformation that involves the interaction of several Bcl-xL regions with the bilayer and extensive refolding, which leads to the release of the N-terminal BH4 helix (Figure 1.1A, blue)[158, 160].

The specific roles of the different membrane-integrated conformations of Bcl-xL and their anti-apoptotic functions remain unclear; nevertheless, each has been linked to a different

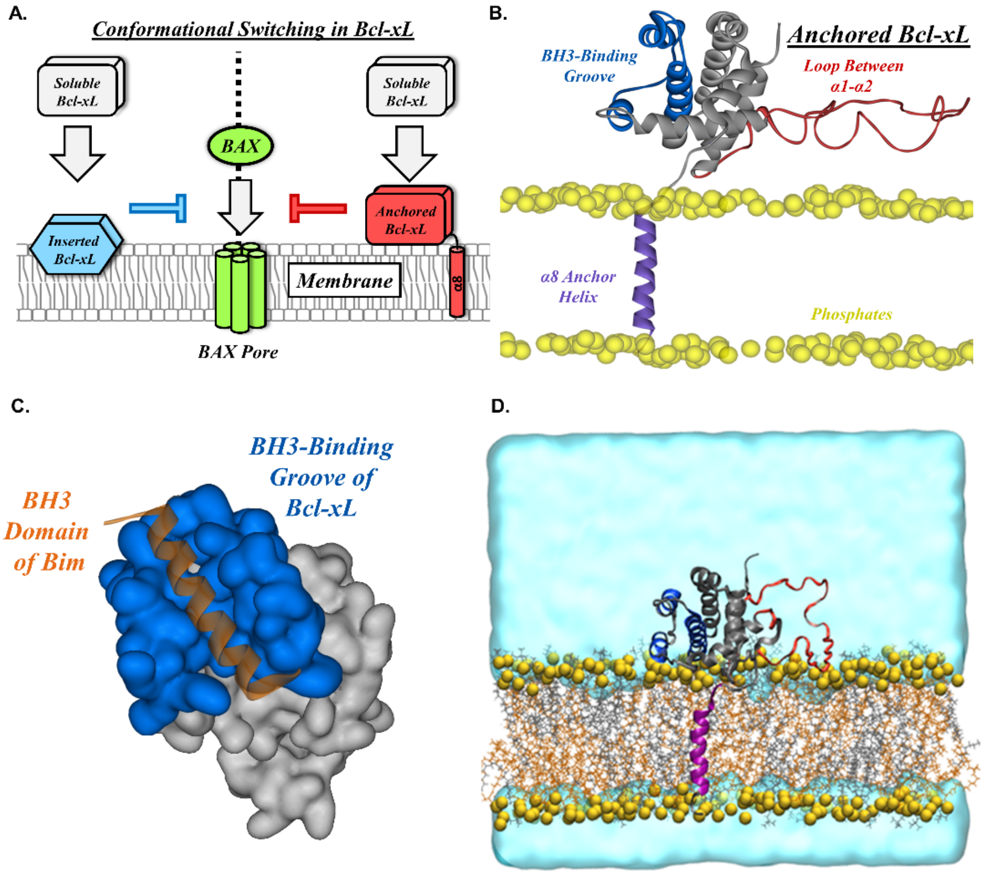

Figure 1.1: Membrane associated Bcl-xL. (A) According to the "embedded together" model, the interactions between the anti-apoptotic protein Bcl-xL and its pro-apoptotic targets (e.g., pore-former BAX) require their transition to the mitochondrial outer membrane[82]. Two different membrane-integrated Bcl-xL conformations have been identified: membrane-inserted and membrane-anchored Bcl-xL. The former is characterized by extensive refolding[158, 160], while the latter retains the fold of the soluble state (aside from the released $\alpha 8$ anchor helix)[178, 177, 126]. Here, we focus on the membrane-anchored conformation of Bcl-xL and the influence of cardiolipin and protonation on its conformational dynamics. (B) The initial configuration of membrane-anchored Bcl-xL used in the all-atom molecular dynamics simulations. The protein is shown in secondary structure representation. The soluble head region (helices $\alpha 1$ through $\alpha 7$) is shown in grey with its BH3-binding groove highlighted in blue. The loop connecting $\alpha 1$ and $\alpha 2$ is shown in red and the $\alpha 8$ anchoring helix is shown in purple in a transmembrane configuration. The lipid phosphate phosphorus atoms are shown as yellow spheres. The rest of the simulation system has been removed for clarity. (C) A surface representation of the BH3-binding groove of Bcl-xL (blue) bound to the BH3 domain of Bim (orange), PDB ID: 3FDL. (D) A cut-away representation of the complete simulation system. The protein and lipid phosphate phosphorus atoms are rendered as in (B), the rest of the lipid molecules are shown in licorice representation (POPC, grey; TOCL, orange), and water molecules are rendered as slabs in cyan.

mode of apoptotic regulation. In the case of the anchored conformation, the lack of refolding of the soluble head region (helices $\alpha1$ through $\alpha7$), as compared to folding in the solution, results in an intact BH3-binding groove[178, 177, 126] (Figure 1.1B,C). BH3 domains are conserved regions in Bcl-xL homologs, such as its targets BAX and BAK, that are used to recognize and bind other apoptotic regulators[95, 12, 21]. Meanwhile, the global refolding in the inserted conformation is likely to disrupt the BH3-binding groove in Bcl-xL, suggesting an alternative mechanism to bind and inhibit its target proteins is possible.

The lipid composition of mitochondrial membranes has a prominent effect on the membrane interactions and refolding of Bcl-xL. The mitochondria-specific lipid cardiolipin is of particular importance because its abundance in mitochondrial membranes presents a preferential distribution, with significant enrichment at mitochondrial contact sites[153, 112, 90]. These cardiolipin-rich regions are often referred to as hotspots for apoptotic regulation and under non-apoptotic conditions they contain an approximate 30% cardiolipin fraction compared to the average 4% of the mitochondrial outer membrane[28, 27]. Additionally, apoptosis-related increases in cardiolipin concentration at the mitochondrial outer membrane (redistributed from the inner mitochondrial membrane)[28, 27] could further modulate Bcl-xL interactions and conformations.

To better understand how the enrichment of cardiolipin affects the membrane-anchored form of Bcl-xL (Figure 1.1B), we performed all-atom molecular dynamics (MD) simulations (Figure 1.1D) in the presence or absence of cardiolipin in a phosphatidylcholine matrix (2:1 PC:CL or 100% PC, respectively). Four simulations were performed with all acidic and histidine sidechains either protonated or deprotonated due to the significance of the protein protonation state on the Bcl-xL membrane interactions[160, 158]. The results from these simulations indicate that cardiolipin and protonation modulate the dynamics of the $\alpha1$-$\alpha2$ loop as well as the orientation of the soluble head region of membrane-anchored Bcl-xL.

1.3 Results

1.3.1 Orientation of the Soluble Head and Accessibility of the BH3-Binding Groove

To evaluate the effect of the mitochondrial specific anionic lipid cardiolipin (1,1,2,2,tetraoleoyl-cardiolipin, TOCL) and protein protonation state on the conformational dynamics of membrane-anchored Bcl-xL, we performed four all-atom MD simulations of Bcl-xL, see Table 1.1 and Figure 1.1D. To summarize, we studied protonated and unprotonated Bcl-xL in a POPC (palmitoyl-oleoyl-phosphatidylcholine) lipid bilayer, as well as protonated and unprotonated Bcl-xL in a 2:1 POPC:TOCL lipid bilayer. Analysis of the Bcl-xL soluble head orientation and corresponding accessibility of its BH3-binding groove were carried out by defining a binding groove vector (see Materials and Methods) and monitoring its orientation during the course of the simulation with respect to the membrane normal, as illustrated in 1.2.

Table 1.1: Summary of microsecond-timescale simulations run on Anton2.

Simulated System	**Protonation State**	**Membrane Composition**
Bcl-xL with 50 nM NaCl	Protonated Bcl-xL	POPC
Bcl-xL with 50 nM NaCl	Unprotonated Bcl-xL	POPC
Bcl-xL with neutralizing	Protonated Bcl-xL	2:1 POPC:TOCL
Bcl-xL with neutralizing	Unprotonated Bcl-xL	2:1 POPC:TOCL

The deviation of the BH3-binding groove vector from the membrane normal, depicted in 1.2A,B, is shown as a function of time in 1.2C,D. Deviation angles above 90° (1.2A) are indicative of a partially occluded binding site and values below 90° (1.2B) are indicative of a more accessible BH3-binding groove. The unprotonated 2:1 POPC:TOCL simulation shows large fluctuations with the deviation angles primarily occupying angles between 90° and 110° (1.2C). The unprotonated POPC simulation shows a similar behavior until around 3.75 µs, where there is a sharp transition from angles above 90° to angles centered approximately at 40°, this configuration is sampled for about 1 µs before transitioning back to an angle above 90° (1.2C). Fluctuations are clearly smaller in the protonated simulations (1.2D) with both simulations exhibiting similar behavior until 2.75 µs, when the cardiolipin-containing simulation gradually converges to lower values under 90° through a sustained rotation of the soluble head over a period of 1 µs (1.2D).

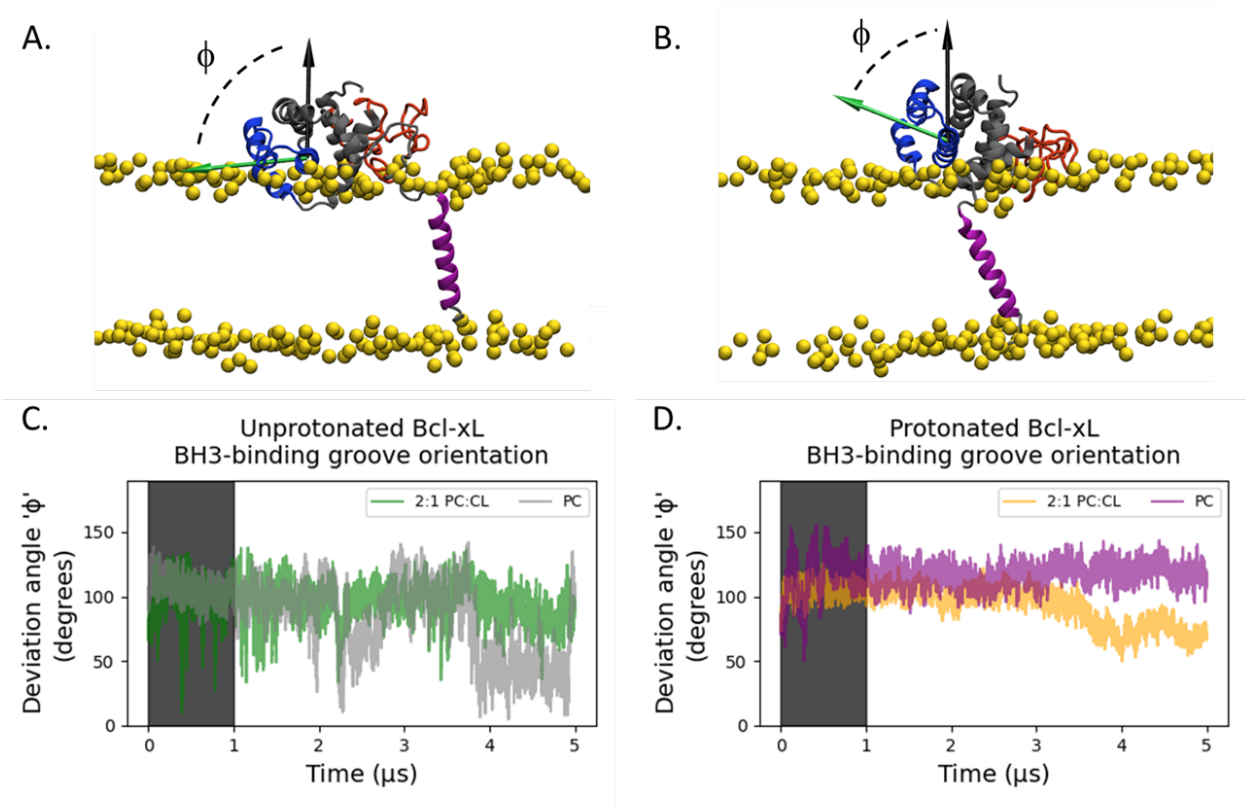

Figure 1.2: Accessibility of the Bcl-xL BH3-binding groove. (A) Configuration snapshot corresponding to a BH3-binding groove vector (green arrow) with a deviation angle from the membrane normal (black arrow), Φ, of greater than 90°, suggesting occlusion of the BH3-binding groove (color scheme as in Figure 1.1B). (B) Configuration snapshot corresponding to a groove vector with a shallower than 90° deviation angle from the membrane normal, suggesting an accessible BH3-binding groove (color scheme as in Figure 1.1B). BH3-binding groove deviation angle as a function of time for (C) unprotonated Bcl-xL in a 2:1 POPC:TOCL lipid bilayer (green) and POPC lipid bilayer (grey), and (D) protonated Bcl-xL in a 2:1 POPC:TOCL lipid bilayer (yellow) and POPC lipid bilayer (purple). The shaded regions (time < 1 µs) represent the non-stationary portion of the trajectories and were not included in further analyses (see also Supplemental Figure 1.8).

In order to investigate the relationship between of groove deviation angle and membrane composition, we considered the corresponding deviation angle distributions over two distinct time intervals exhibiting steady-state behavior (see 1.3). The distributions for both unprotonated systems remain broad and overlap over both sampled time intervals (1.3A,B). Furthermore, in the unprotonated POPC simulation, the BH3-binding groove deviation angle distribution is over the entire allowed configuration space, while in the unprotonated POPC:TOCL simulation, the sampling of large deviation angles is favored. Only the protonated POPC:TOCL simulation shows a separate narrow distribution of deviation angles under 90° (1.3D).

Taken together, these results suggest that protonation of Bcl-xL titratable residues (ten aspartic acids, twenty-one glutamic acids, and four histidines) modulates the conformational dynamics of the Bcl-xL soluble head region in the membrane-anchored configuration. Furthermore, the presence of cardiolipin promotes the re-orientation of the soluble head in protonated Bcl-xL towards a configuration that exposes the BH3-binding groove.

1.3.2 Conformational Dynamics of the α1-α2 Loop

To evaluate the effect of the protein protonation state and the addition of cardiolipin on the conformation of the α1-α2 loop, we computed the distribution of the radius of gyration over the same trajectory interval, from 2.25 µs to 5.0 µs, on all four simulations (1.4). In both the unprotonated (1.4C) and protonated (1.4D) systems, the addition of cardiolipin results in a broader distribution, indicating a more flexible loop. In the POPC simulation systems, protonation results in larger values for the radius of gyration and up-shifts the entire distribution, indicating an extension of the loop. Conversely, in the case of cardiolipin, protonation narrows and results in lower values for the radius of gyration, suggesting a more compact conformation.

To evaluate the membrane interactions of the α1-α2 loop, we determined the distributions of positions of Gly-21 and Gly-70 along the transmembrane direction (1.5). Gly-70 was selected

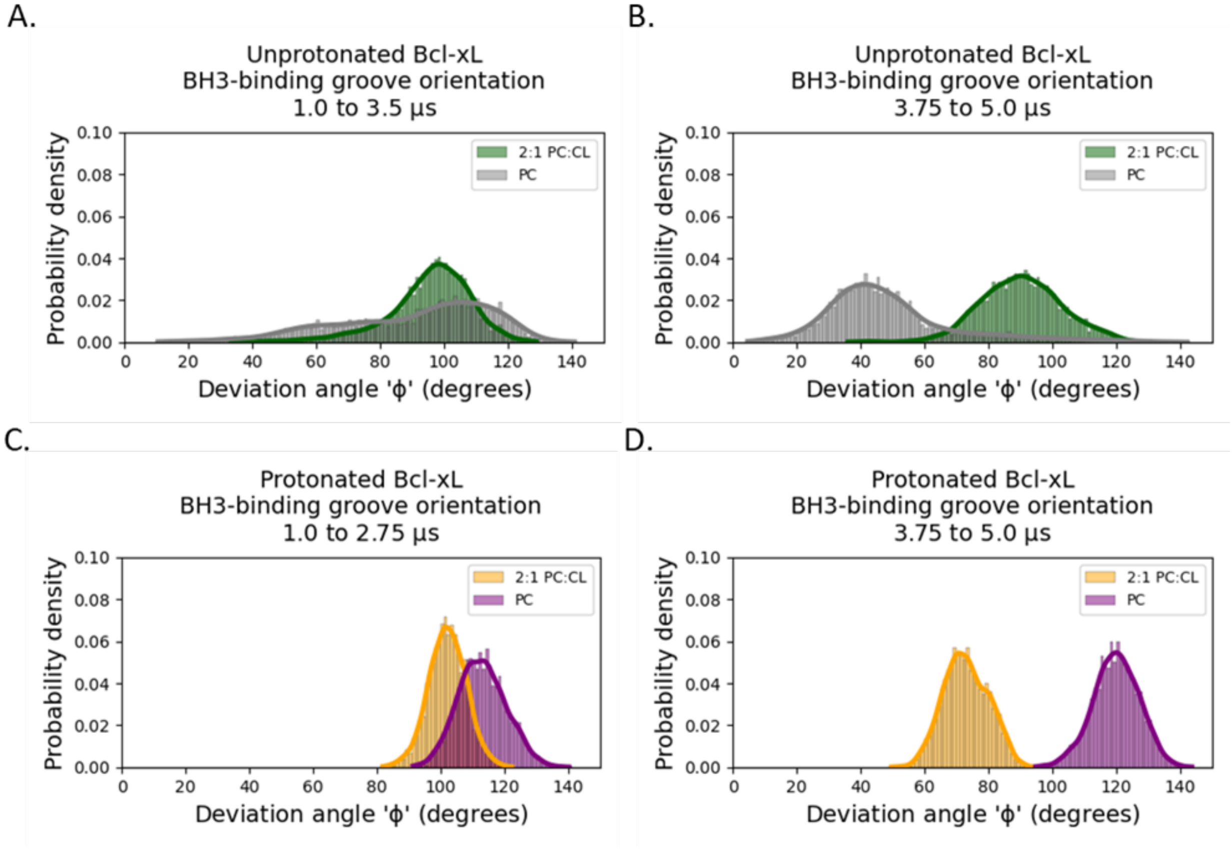

Figure 1.3: Orientational configurations of the BH3-binding groove. The changes in the distributions of the BH3-binding groove deviation angle from the membrane normal over two separate time intervals indicate that the presence of cardiolipin narrows the configurational space sampled by the soluble head and that both protonation of Bcl-xL and cardiolipin favors specific orientations of the soluble head relative to the membrane surface, consistent with accessible configurations of the BH3-binding groove. (A) and (B) Binding-groove deviation angle distributions for unprotonated simulations based on stationary portions of unprotonated PC system. (C) and (D) Binding groove deviation angle distributions for protonated simulations based on stationary portions of protonated 2:1 PC:CL system. All angle histograms are colored as in Figure 1.2C, D.

due to its membrane interaction in the inserted form of Bcl-xL[158]. Its position near the middle of the 61-residue long $\alpha1$-$\alpha2$ loop was compared to Gly-21, which constitutes the first residue in the loop, allowing a detailed analysis of membrane interactions between different regions of the loop in these various systems.

In the unprotonated systems, Gly-21 has a broader distribution closer to the membrane headgroup region in the POPC simulation and a narrower distribution further from the

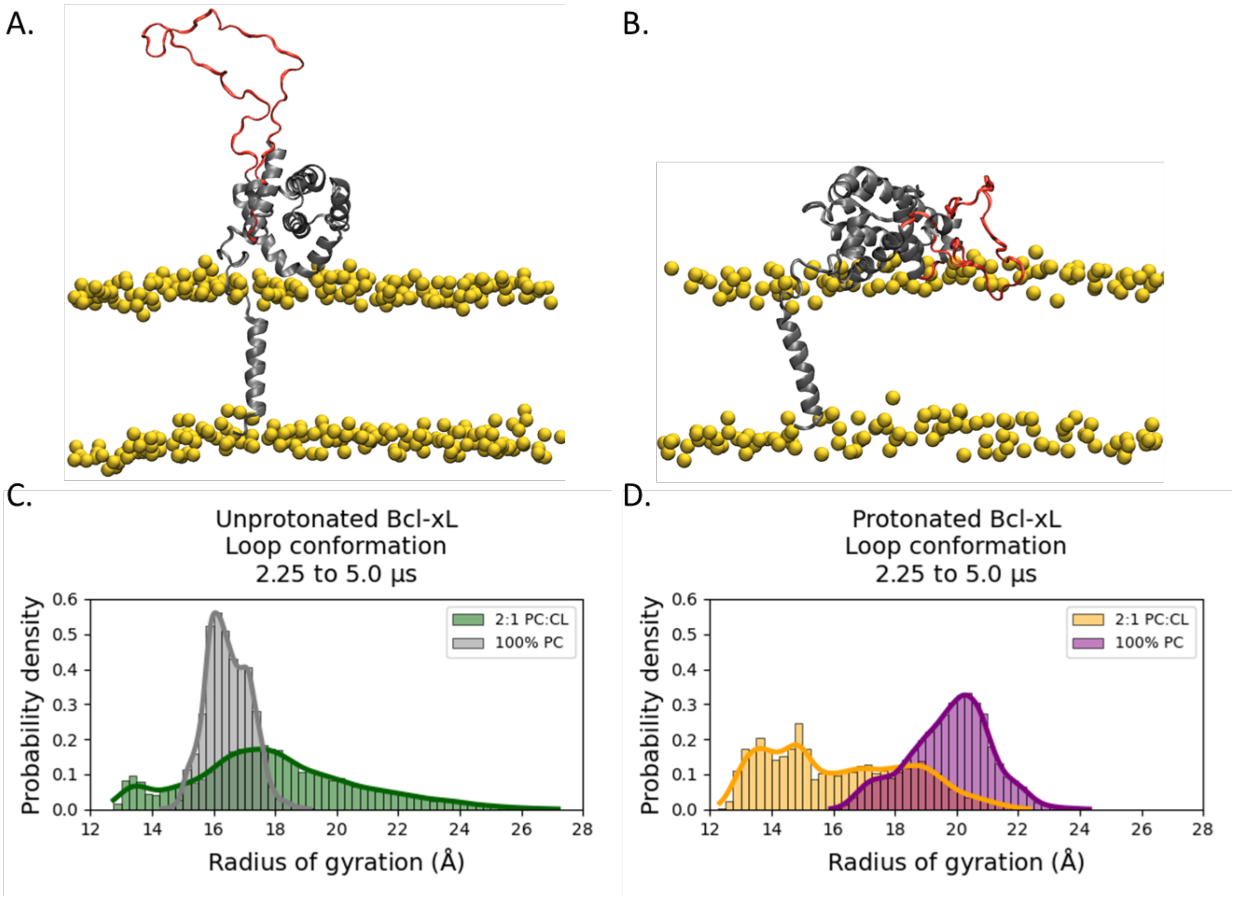

Figure 1.4: Conformation of the $\alpha 1$-$\alpha 2$ loop. (A) Configuration snapshot corresponding to an extended loop conformation in the unprotonated POPC:TOCL system. (B) Configuration snapshot corresponding to a compact loop conformation in the protonated POPC:TOCL system. The protein is shown in secondary structure representation colored gray, except for the $\alpha 1$-$\alpha 2$ loop which is shown in red. The lipid phosphate phosphorus atoms are shown as yellow spheres. The rest of the simulation system has been removed for clarity. The $\alpha 1$-$\alpha 2$ loop radius of gyration is broadly distributed in the POPC:TOCL systems in comparison to POPC, suggesting that the presence of cardiolipin confers more flexibility to the loop. The comparison between the radius of gyration distributions in the unprotonated (C) and protonated (D) systems suggests that protonation of the Bcl-xL titratable residues promotes extended loop conformations in the POPC system and compact loop conformations in the POPC:TOCL system.

membrane surface in POPC:TOCL (1.5C). Protonation of Bcl-xL results in a narrower distribution for both simulation systems. However, in the protonated POPC simulation, Gly-21 was shifted away from the membrane surface and into the bulk solvent, while in the pro-

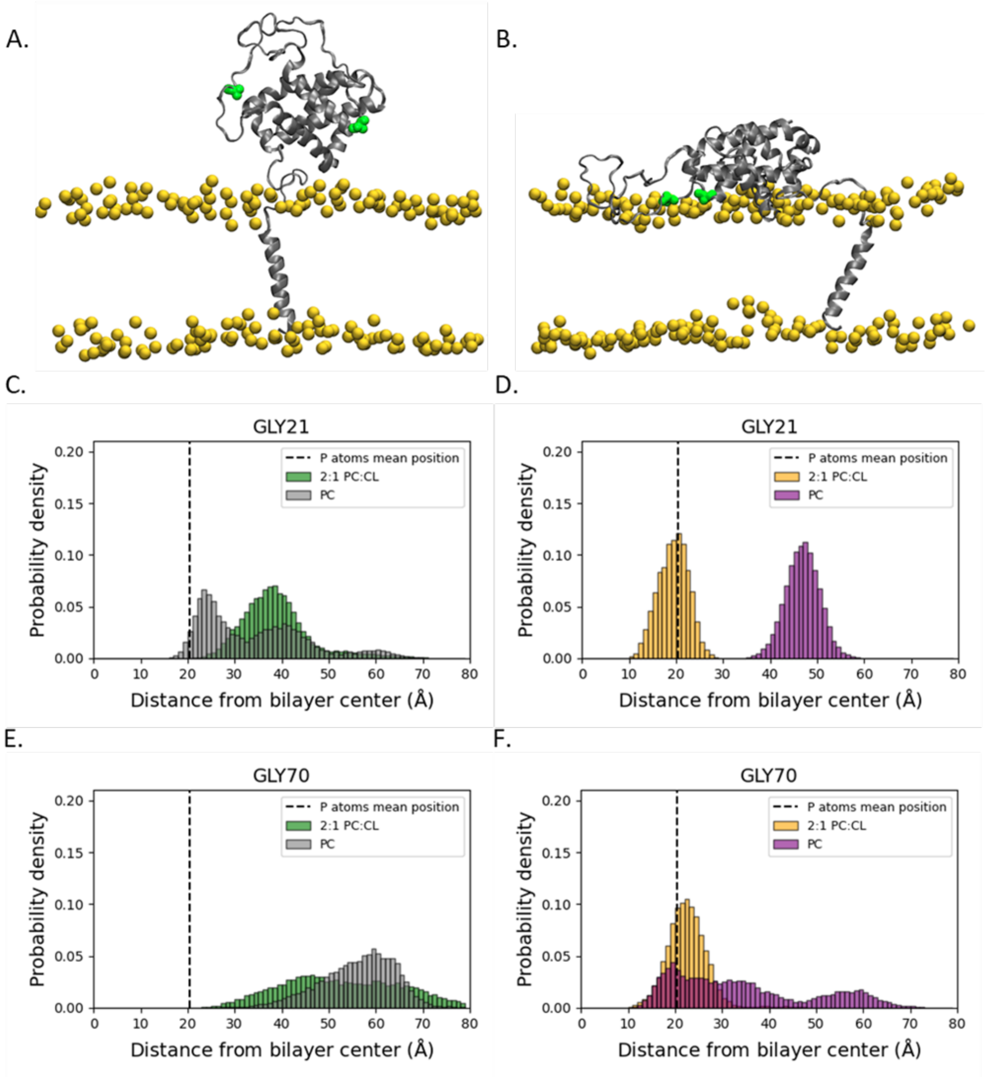

Figure 1.5: Interactions of the $\alpha1$-$\alpha2$ loop with the membrane surface. (A) Configuration snapshot corresponding to a $\alpha1$-$\alpha2$ loop that is not interacting with the membrane surface in the unprotonated POPC:TOCL system. (B) Configuration snapshot corresponding to a membrane-interacting $\alpha1$–$\alpha2$ loop in the protonated POPC:TOCL system. The protein is shown in secondary structure representation colored gray, while Gly-21 and Gly-70 are shown in green as filled-spheres. The lipid phosphate phosphorus atoms are shown as yellow spheres. The rest of the simulation system has been removed for clarity. (C–F). The distributions of two glycines in the $\alpha1$-$\alpha2$ loop (Gly-21 near $\alpha1$ and Gly-70 in the middle of the loop chain) along the transmembrane direction suggest that protonation of Bcl-xL promotes the interactions of the loop with the membrane surface, while the addition of cardiolipin favors the partitioning of the loop residues in the membrane lipid head-group region. The vertical dashed line in the histograms is located at the mean position of lipid phosphate group phosphorus atoms, an indication of the location of the membrane lipid head-group region along the transmembrane direction.

tonated POPC:TOCL simulation, the Gly-21 distribution laid within the membrane lipid headgroup region centered at the level of the lipid phosphate groups (1.5D).

A similar analysis was performed on Gly-70 (1.5E,F) in order to evaluate the membrane interactions near the middle of the disordered loop. In the unprotonated systems, Gly-70 resides in the bulk solvent (1.5E), indicating that Gly-70 is not interacting with the membrane surface. In contrast, the corresponding distributions for the protonated systems suggest that Gly-70 interacts with the membrane surface upon protonation of the Bcl-xL titratable residues (1.5F) with a narrower distribution for protonated Bcl-xL in POPC:TOCL, centered at the depth of the lipid phosphate group as in the unprotonated systems. Taken together, these results show that protonation promotes the interactions of the $\alpha1$-$\alpha2$ loop with the membrane surface, while the addition of cardiolipin promotes the partitioning of the loop residues in the membrane lipid headgroup region.

1.3.3 Transmembrane Helix Orientation

To determine if the conformational dynamics of the transmembrane helix ($\alpha8$) were effected by the changes to our simulated systems, we measured the orientation of the transmembrane helix ($\alpha8$) principal axis vector with respect to the membrane normal as a function of time. The corresponding distributions of deviation angles for all four systems show significant overlap (1.6), which suggests that neither protonation nor the addition of cardiolipin affect the conformational dynamics of $\alpha8$ in a transmembrane configuration.

1.4 Discussion & Conclusions

Apoptosis or controlled cell death is a critically important process in maintaining and developing healthy cell populations and tissues. Dysregulation of apoptosis has been shown

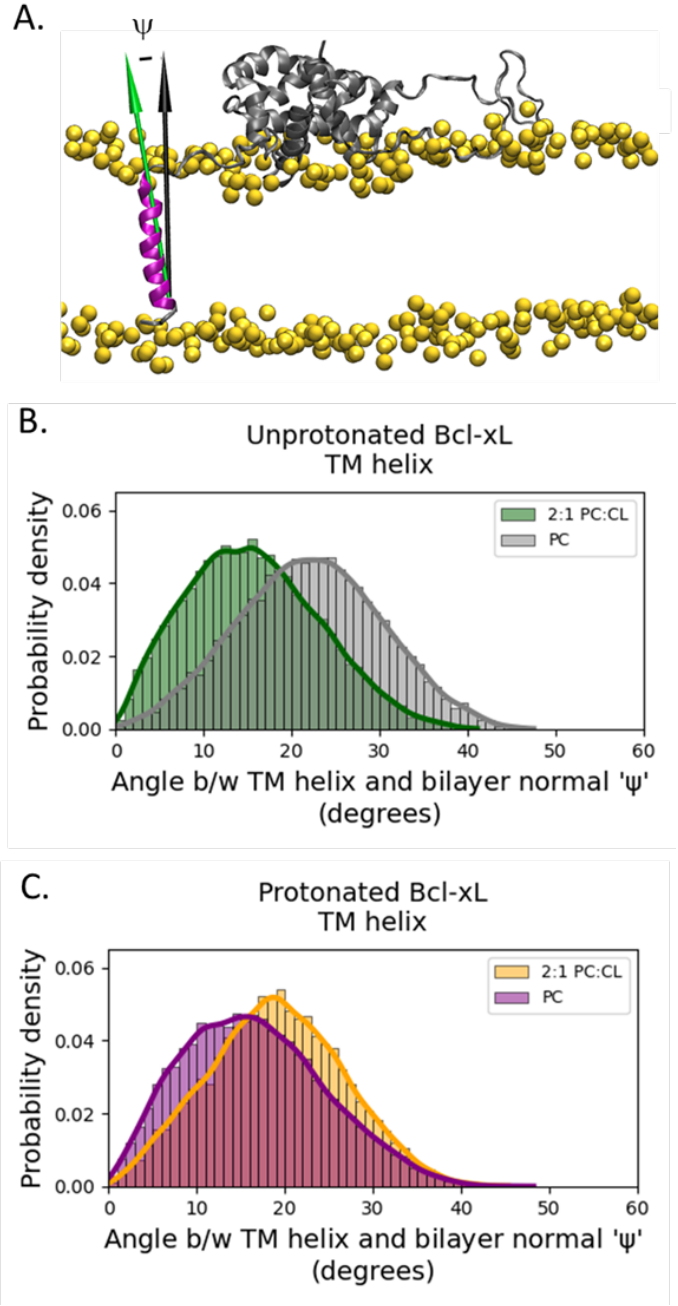

Figure 1.6: Orientation of the transmembrane (TM) helix. (A) The orientation of helix $\alpha8$ was determined by the deviation angle, Ψ, of the helix principal axis (green arrow) from the membrane normal (black arrow). The protein is shown in secondary structure representation colored gray, except for helix $\alpha8$ which is shown in purple. The lipid phosphate phosphorus atoms are shown as yellow spheres. The rest of the simulation system has been removed for clarity. Distributions of TM helix angles for unprotonated (B) and protonated (C) simulations show significant overlap and provide no in-formation correlated with soluble head orientation.

to have significant consequences, from hyperactive apoptosis contributing to neurodegeneration or immunodeficiency, to insufficient apoptosis leading to autoimmunity and cancer[139]. Furthermore, cancer treatment efficacy is reduced by the ability of cancer cells to avoid apoptosis. A key step in triggering apoptosis is the permeabilization of the mitochondrial outer membrane, which releases apoptotic factors into the cytosol and ultimately results in cell death[163, 23]. MOMP is controlled and regulated by the Bcl-2 family of proteins, which directly interacts with the mitochondrial outer membrane to either promote or prevent the formation of oligomeric pores[12, 21, 179]. In the case of Bcl-xL, changes in membrane lipid composition[158, 160, 28, 27], as well as the protonation state of Bcl-xL[158, 160], have also been implicated in its regulation of apoptosis. While protonation changes in proteins are unlikely to be caused by decreases in cytosolic pH, several other factors modulate the pKa of titratable residues. It is well known that the pKa values for D (aspartic) and E (glutamic) residues have a range of 5 pH units depending on factors such as environmental polarity and water exposure[105, 106]. In the case of membrane-active proteins such as Bcl-xL, these changes in pKa could be induced by their water-to-membrane transitions[149, 18]. The anchoring of Bcl-xL to lipid bilayers is therefore hypothesized to modulate the protonation state of its titratable residues, which could affect its membrane interactions and dynamics. Here, we examined Bcl-xL under four different conditions: protonated or unprotonated Bcl-xL embedded in a 100% POPC or 2:1 POPC:TOCL membrane.

The evaluation of the orientation of the soluble head reveals that as individual perturbations, neither the presence of cardiolipin in the membrane nor the protonation of the titratable residues result in exposure of the BH3-binding groove, suggesting that cardiolipin and protonation act in concert to promote a favorable orientation of the soluble head that exposes the BH3-binding site on the microsecond timescale (Figures 1.3 and 1.3). In contrast, the soluble head orientation in the POPC unprotonated system exhibits large fluctuations over the entire possible conformational space, which is inconsistent with the development of a competent binding conformation.

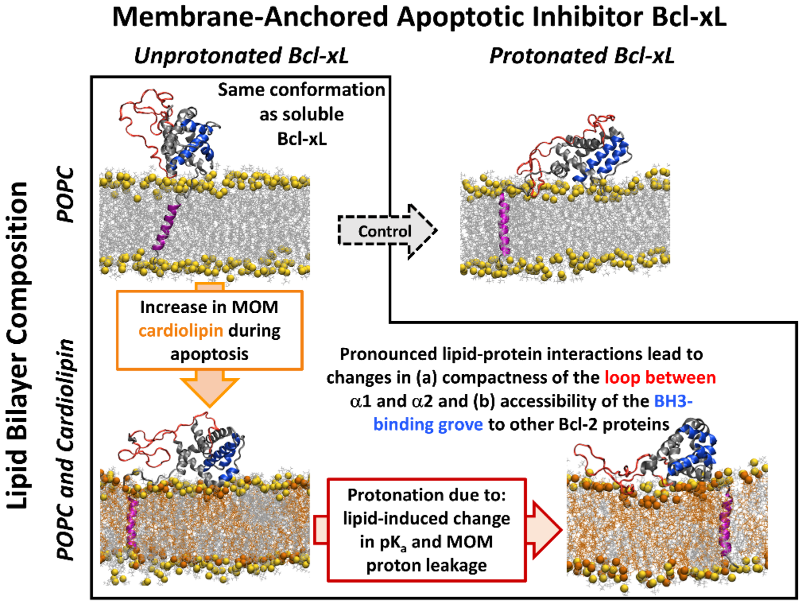

Figure 1.7: Schematic summary of the effects of cardiolipin and protonation on the conformational dynamics of membrane-anchored Bcl-xL studied by MD simulations. Four systems examined in this study are illustrated by the following representative snapshots from microsecond MD trajectories: 2.44 µs for E-, D-, and H+ Bcl-xL in a POPC lipid bilayer (top left); 3.66 µs for E°, D°, and H° Bcl-xL in a POPC lipid bilayer (top right); 4.30 µs for E-, D-, and H+ Bcl-xL in a 2:1 POPC:TOCL lipid bilayer (bottom left); and 3.71 µs for E°, D°, and H° Bcl-xL in a 2:1 POPC:TOCL lipid bilayer (bottom right). In the absence of cardiolipin or protonation (top left), the soluble head domain of the membrane-anchored Bcl-xL does not interact with the lipid membrane surface and largely retains the conformation of the soluble protein[178, 177, 126]. The addition of cardiolipin (bottom left, orange), which corresponds to physiologically observed changes of MOM during apoptosis[28, 27], induces membrane interactions of the soluble head domain of the protein, resulting in protein conformational changes (see Figures 1.3–1.7). These interactions become more prominent upon subsequent protonation of all acidic and His residues (bottom right), resulting in (i) lipid interactions of the loop between helices $\alpha1$ and $\alpha2$ (highlighted in red) and (ii) reorientation of the binding grove (highlighted in blue) that can engage BH3 domains of the other Bcl-2 proteins. Physiologically, it is suggested that protonation corresponds to the bilayer-induced shifts in pKa[158, 160] or proton leakage at the early stages of MOMP[158, 160]. Note that no loop-lipid binding or reorientation of the BH3-binding groove was observed in the control MD simulations of protonated Bcl-xL in the absence of cardiolipin (top right). Conformational changes and lipid interactions induced by cardiolipin and in the membrane-anchored Bcl-xL provide structural insights into the initial protein conformational changes on the pathway towards fully refolded membrane-inserted Bcl-xL[158, 160].

Analysis of the $\alpha1$-$\alpha2$ loop indicates that the addition of cardiolipin results in a more flexible loop (1.4). Protonation is shown to extend the loop in the presence of POPC. However, the extended loop in protonated Bcl-xL results in a narrower distribution of values in the presence of cardiolipin, suggesting a stable and extended disordered loop (1.4D). This is further exemplified when considering individual loop residues. While the position of Gly-21 is constrained by the orientation of the soluble head, as it is located right after helix $\alpha1$, Gly-70 is near the middle of the loop and not constrained by the soluble head (1.5). The distributions in 1.5 E,F support the conclusion that protonation promotes membrane interactions for Gly-70, which is consistent with previous in vitro measurements[158].

In contrast to the rest of the protein, the orientation of the transmembrane helix with respect to the membrane normal remains largely the same across all four systems (1.6), with tilt angle fluctuating in the range of 10–25°. This range is somewhat lower than reported previously[177, 126], but is consistent with the thicker bilayer used in our simulation.

Overall, this work provides structural insights into the dependence of the conformational dynamics of Bcl-xL on protonation states and membrane composition. Protonation and the addition of cardiolipin reorient and stabilize the soluble head in a new configuration with a high probability that the BH3-binding groove is not occluded (1.7). These same conditions also produce a more dynamic $\alpha1$-$\alpha2$ loop that readily interacts with the membrane surface, recapitulating the coupled effect of protonation and cardiolipin content (1.7). The concerted effects of protonation and cardiolipin on the membrane-anchored form of Bcl-xL are consistent with in vitro measurements of the Bcl-xL membrane insertion, which showed that the presence of cardiolipin produces more favorable protonation-dependent insertion free energy[158, 160]. The extent to which cardiolipin modulates the protonation of Bcl-xL by altering the pKa of its titratable residues is, however, a complex issue, the characterization of which will require further studies.

1.5 Future Work

Our current work on Bcl-xL explores the pre-apoptotic and apoptotic pre-MOMP (mitochondrial outer membrane permeation) conditions in the presence of sodium. However, physiologically relevant conditions are highly complex and both protonation of the residues and divalent cations have been implicated in these interactions. As apoptosis proceeds, the mitochondrial outer membrane composition changes to one that supports a greater fraction of cardiolipin. Considering complex changes occurring in this system, there is quite a bit of room for future work.

First, we propose to pursue a more complete picture of the pre-apoptotic and apoptotic pre-MOMP conditions by simulating membrane-anchored, unprotonated Bcl-xL in the presence of Ca^{2+} and Mg^{2+}. Following this study, it would also be relevant to explore Bcl-xL with partial protonation at just the Histidine sites to represent another pre-apoptotic condition. Finally, a set of simulations with membrane-anchored Bcl-xL with all Histidine and acidic residues protonated would represent the apoptotic and post-apoptotic conditions. Currently, the vast majority of these simulations have already been run on Anton2.

1.6 Materials & Methods

1.6.1 Simulation Systems

A model of the full-length Bcl-xL protein in a membrane-anchored configuration was constructed by combining two solution NMR structures: one lacking the C-terminal helix (PDB ID: 1LXL; residues 1–222)[98] and another of the isolated C-terminal helix (PDB ID: 6F46; helix $\alpha 8$, residues 209–231)[115]. After aligning the C-terminal helix along the Cartesian z-axis, the two structures were superimposed and joined at residue Gln-207 to generate a model for the membrane anchored full-length Bcl-xL, where the C-terminal helix is in a transmembrane orientation. For each simulation, Bcl-xL was anchored into the membrane by embedding the C-terminal helix in the lipid bilayer such that the Trp-213 residue was just below the lipid phosphate groups and the soluble folded domain was within 4 Å of the membrane surface. The membrane-anchored Bcl-xL model was incorporated into four different simulation systems, each with one of two protein protonation states to which all Bcl-xL acidic and histidine residue sidechains were protonated or unprotonated (hereafter identified as protonated or deprotonated configurations, respectively); and one of two membrane compositions: 100% 1-palmitoyl-2-oleoyl-*sn*-glycero-3-phosphocholine (POPC) or POPC at a 2:1 ratio with 1,1,2,2,-tetraoleoyl-cardiolipin (2POPC:1TOCL). The simulation system setup was performed with CHARMM-GUI[67, 66, 173, 68, 83, 113]. All simulations are summarized in Table 1.1.

For the unprotonated 100% POPC simulation, Bcl-xL was embedded in a lipid bilayer consisting of 411 POPC, both solvated with 36,055 water molecules and neutralized with 50 mM excess NaCl (43 Na+, 32 Cl-), for a total of 166,907 atoms and an initial simulation cell size of 129.9 Å × 129.3 Å × 124.8 Å. For the protonated 100% POPC simulation, Bcl-xL was embedded in a lipid bilayer consisting of 412 POPC, both solvated with 36,094 water molecules and neutralized, and with 50 mM excess NaCl (32 Na+, 56 Cl-), for a total of 167,206 atoms and an initial simulation cell size of 130.0 Å × 128.1 Å × 125.0 Å. Similarly, for the unprotonated 2:1 POPC:TOCL simulation, Bcl-xL was embedded in a lipid bilayer consisting of 239 POPC and 120 TOCL, both solvated with 46,584 water molecules and neutralizing Na+ (131 Na+), for a total of 205,383 atoms and an initial simulation cell size of 151.1 Å × 143.3 Å × 129.4 Å. For the protonated 2:1 POPC:TOCL simulation, Bcl-xL was embedded in a lipid bilayer consisting of 239 POPC and 120 TOCL, both solvated with 46,586 water molecules and neutralizing Na+ (96 Na+), for a total of 205,389 atoms and an initial simulation cell size of 150.6 Å × 157.9 Å × 127.3 Å.

1.6.2 Initial Molecular Dynamics Simulations

The initial equilibration of the simulation systems was performed with NAMD 2.11[110]. Each system was subjected to 50,000 steps of conjugate gradient energy minimization, followed by a 400-ps run at constant temperature (310 K) and pressure (1 atm) with harmonic restraints on the protein-backbone atoms and the PC carbonyl carbons using a decreasing force constant equal to 10, 5, 2, 1, 0.5, 0.2, 0.1, and 0.05 $\text{kcal}\cdot\text{mol}^{-1}\cdot\text{Å}^{-2}$. Unrestrained dynamics were then run for 10 ns on the unprotonated simulations, 7 ns on the protonated 100% POPC simulation, and 15 ns on the protonated 2:1 POPC:TOCL simulation. The CHARMM36[74, 10] force fields were used for the protein, lipids, and ions, and the TIP3P model was used for water[69]. The smooth particle-mesh Ewald summation method[37, 30] was employed for the calculation of electrostatic interactions. Short-range real-space interactions were cutoff at 12 Å, employing a force-based switching function. A reversible multiple-time step algorithm[45] was used to integrate the equations of motion with a time step of 1 fs for electrostatic forces, short-range non-bonded forces, and bonded forces. A Langevin scheme was used for temperature control and a Nosé–Hoover–Langevin piston[92, 38] was used for pressure control.

1.6.3 Microsecond-Timescale Molecular Dynamics Simulations

After initial equilibration, all simulation systems were transferred to Anton2, a special purpose supercomputer for biomolecular simulations, and run for 5.0 µs each[133]. The CHARMM36 force field[74, 10] was used for the protein, lipids, and ions, and the TIP3P model was used for water[69]. The r-RESPA algorithm[152] was used to integrate the equations of motions with a time step of 3 fs for long-range non-bonded forces and a 1 fs time step for both short-range non-bonded and bonded forces. The k-Gaussian split Ewald method[132] was used for the long-range electrostatic interactions. The SHAKE algorithm[125] was employed to constrain all hydrogen atom bond lengths. Simulations were performed at a constant temperature (310 K) and pressure (1 atm) using Nosé–Hoover chains[91] and the Martyna–Tobias–Klein barostat[92]. The RESPA algorithm, temperature control, and pressure control were implemented using the multigrator scheme[86].

1.6.4 Trajectory Analysis

To evaluate the orientation and accessibility of the Bcl-xL BH3-binding groove, we defined a BH3-binding groove vector as the normal to the plane formed by the principal axis of helix $\alpha5$ (from residue 143 to residue 153) and the vector connecting the geometric center of the α-carbons in residues 143 through 146 in helix $\alpha5$ to the geometric center of the α-carbons in residues 170 through 173 of helix $\alpha6$.

The α-helix principal axes were determined from the moment of inertia tensor of all the Cα atoms of all the residues participating in the helix in the initial configuration.

Analyses were performed with VMD[58] and custom Python scripts. Molecular graphics were generated with VMD.

1.7 Supplementary Information

Effects of Cardiolipin on the Conformational Dynamics of Membrane-Anchored Bcl-xL

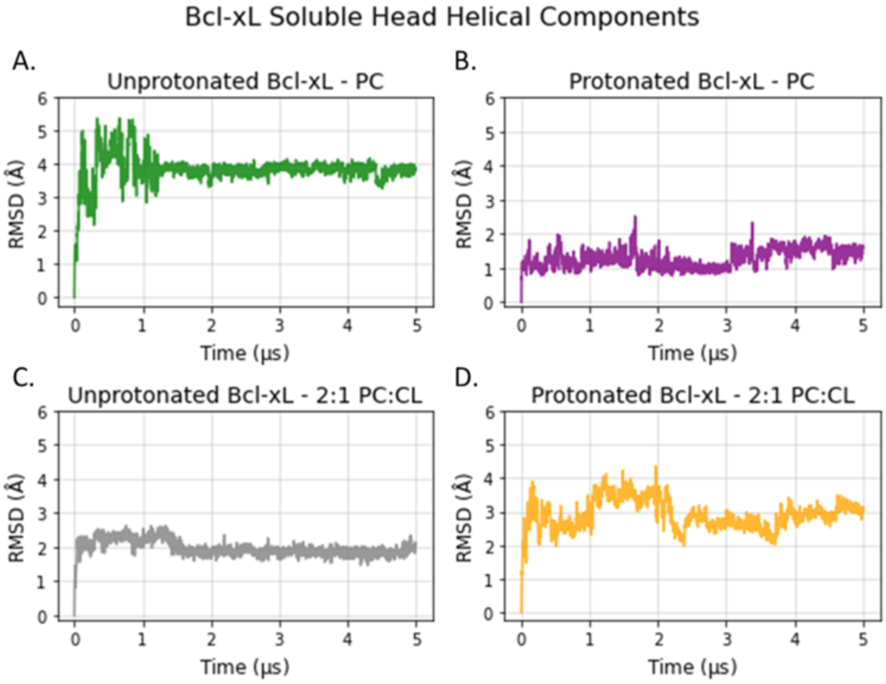

Figure 1.8: RMSD of the soluble head (SH) components of Bcl-xL. RMSDs for all four simulated systems are shown as a function of time. RMSDs were calculated from the backbone (C, N) atoms of the helical residues in $\alpha 1$ through $\alpha 7$ without including any residues in the disordered regions linking the helices.

Chapter 2

Effects of Ca^{2+} and Mg^{2+} on the Conformational Dynamics of Membrane-Anchored Bcl-xL

Vivek Tyagi, Victor Vasquez-Montes, J. Alfredo Freites, Alexander Kyrychenko, Douglas J. Tobias, and Alexey S. Ladokhin

2.1 Abstract

Inhibition of the pore-forming Bcl-2 proteins which target the mitochondrial outer membrane (MOM) is a key process by which apoptosis is regulated to prevent cell death. Bcl-xL, an anti-apoptotic protein, has been shown to interact with these proteins in conjunction with the mitochondrial membrane and cytosolic environment where it serves to sequester pore-forming pro-apoptotic peptides and demonstrably inhibits apoptosis. This function has been shown experimentally to be linked to cellular concentrations of Ca^{2+} and Mg^{2+} as well as

the anionic lipid cardiolipin. Simulated exploration of the role of these divalent cations and lipid systems serve to provide a mechanistic picture for how these variables work together to promote an effective Bcl-xL protein. The acidic residues of Bcl-xL and the anionic lipid cardiolipin have divalent cation bridged interactions that affect the conformation of the highly dynamic Bcl-xL disordered loop which connects alpha helix 1 of the soluble head to alpha helix 2. Furthermore, the tightly held hexa-coordinated waters around Mg^{2+} serve to increase the interaction distance between the divalent charge center and its interactors, allowing for more dynamic ionic behavior while Ca^{2+} exhibits direct interactions that are long-lived and support continuous interactions between specific residues and lipids.

2.2 Introduction

Protein-lipid interactions are prevalent throughout the cell and understanding the essential principles that govern them are key to being able to predict how they will change or be modulated under different conditions. Here, two different ionic systems are explored, Ca^{2+} and Mg^{2+}, in conjunction with an unprotonated, membrane-anchored Bcl-xL protein. The mitochondrial outer membrane (MOM), the native anchoring environment for Bcl-xL, undergoes conversion whereby cardiolipin lipids are transferred from the inner mitochondrial membrane to the outer, thereby increasing the anionic character of the membrane. Both Ca^{2+} and Mg^{2+} have the opportunity to increase the membrane interactions of the acidic residues present in Bcl-xL. Though both ions present a similar +2 charge, their difference in size confers a differing interaction with water resulting in Ca^{2+} being able to directly interact with residues and lipids while Mg^{2+} interacts indirectly and has strongly held, hexa-coordinated water molecules that bridge interactions. This difference in interaction between these divalent cations leads to significantly more interactions between negative charge centers and ions for the Ca^{2+} simulations. The data presented here demonstrates that both Ca^{2+}

and Mg^{2+} strongly influence how protein-lipid interactions occur and the resulting long-term conformations of the Bcl-xL protein. The strong and direct interactions presented by Ca^{2+} imply that divalent cation composition is important in how protein-lipid interactions are mediated.

2.3 Results

2.3.1 Ca^{2+} interactions are consistently long-lived, Mg^{2+} interactions are transient

The membrane mediated spontaneous activation model for Bcl-xL suggests that Bcl-xL achieves ideal conformations to interact with pro-apoptotic pore-formers when sufficient cardiolipin lipids have been transferred from the mitochondrial inner membrane to the mitochondrial outer membrane (MOM). This conversion results in a highly anionic lipid composition for the MOM. Lipid composition and the presence of divalent cations are thought to work in conjunction to produce the most active conformations of the anchored protein. The key to regulating these active conformations is likely the variation in cardiolipin content in the MOM, however divalent concentrations are also relevant since they bridge interactions between the acidic residues on the protein and the anionic lipids on the MOM.

When comparing the interactions of Ca^{2+} and Mg^{2+} with either the anionic mitochondrial membrane or Bcl-xL acidic residues, it is important to consider the proximity of these interactions. While Ca^{2+} can directly interact with negative charge centers, Mg^{2+} interactions are bridged by tightly held, hexa-coordinated water molecules. These water molecules have a residence time around Mg^{2+} that extends beyond 10 μs, making it extremely unlikely that a direct Mg^{2+} interaction (i.e. not bridged by water) would be observed within the time of our simulations (up to 5 μs). This is quantified when viewing the radial distribution

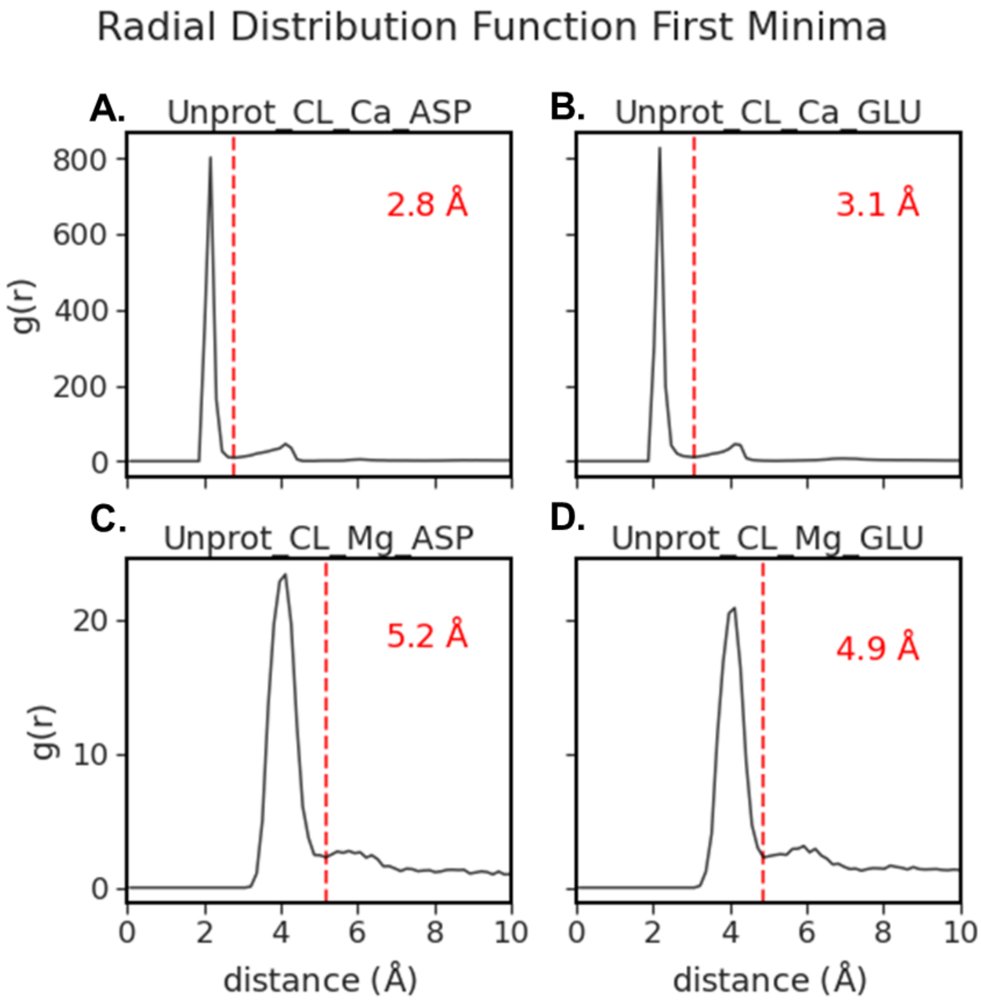

Figure 2.1: Radial distribution function between acidic residue carbonyl oxygen atoms and relevant divalent cation. Panels A & B illustrate the first minima used to quantify the interaction distance of Ca^{2+} with aspartic and glutamic residues respectively. Panels C & D illustrate the first minima used to quantify the interaction distance of Mg^{2+} with aspartic and glutamic residues respectively. The difference between Ca^{2+} and Mg^{2+} is attributed to Mg^{2+}'s tightly held hexa-coordinated water molecules that bridge interactions.

between divalent ions and acidic residues, as shown in 2.1. Ca^{2+} interactions are shown to be roughly 3 Å from acidic residues (2.1A & 2.1B), while Mg^{2+} interactions are shown to be approximately 2 Å greater than that (2.1C & 2.1D), which accounts for the size of the water molecule and the reduction in ionic radius of Mg^{2+} relative to Ca^{2+}.

2.3.2 Ca^{2+} interacts with multiple acidic residues simultaneously, Mg^{2+} interacts with individual acidic residues

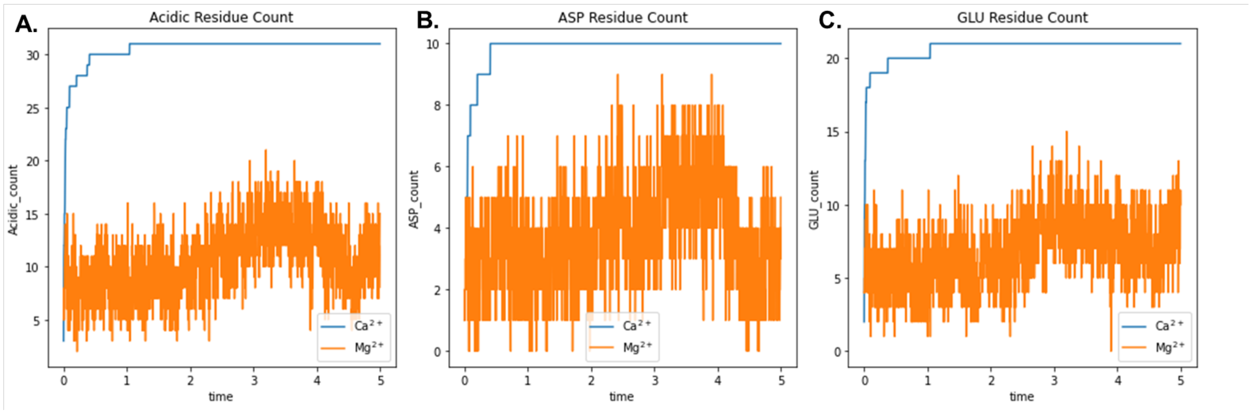

Figure 2.2: Number of acidic residues coordinated with divalent ions as a function of time. Panel A illustrates the number of total acidic residues (Asp: 10; Glu 21; Total: 31) coordinating with Ca^{2+} (blue) and Mg^{2+} (orange). Panels B & C show a similar analysis broken down by Asp or Glu respectively. Ca^{2+} interactions are long-lived after initiation while Mg^{2+} interactions are short-lived and never saturate all acidic residues simultaneously.

Direct interactions with Ca^{2+} and the acidic residues are shown to be long-lived in simulation. Once Ca^{2+} starts interacting with an acidic residue, it appears to remain in that position for the duration of the simulation (2.2, blue). Ca^{2+} interactions are also not limited to single negative charges, meaning they can interact simultaneously with acidic residues and anionic lipids, multiple acidic residues, or multiple anionic lipids. This continuous bridging behavior suggests that Ca^{2+} may be important in achieving idea conformational states. Additionally Ca^{2+} may be involved in localizing anionic lipids, thereby creating hotspots of cardiolipin in the MOM. When viewing Mg^{2+} through a similar lens, simulations show that Mg^{2+} interactions are not as consistent or long-lived as Ca^{2+} (2.2, orange). The observed transient behavior of Mg^{2+} is likely a consequence of the hexa-coordinated water molecules, which effectively create a larger separation for the interacting charges, reducing the likelihood of Mg^{2+} remaining consistently around a negative charge center (2.2, orange).

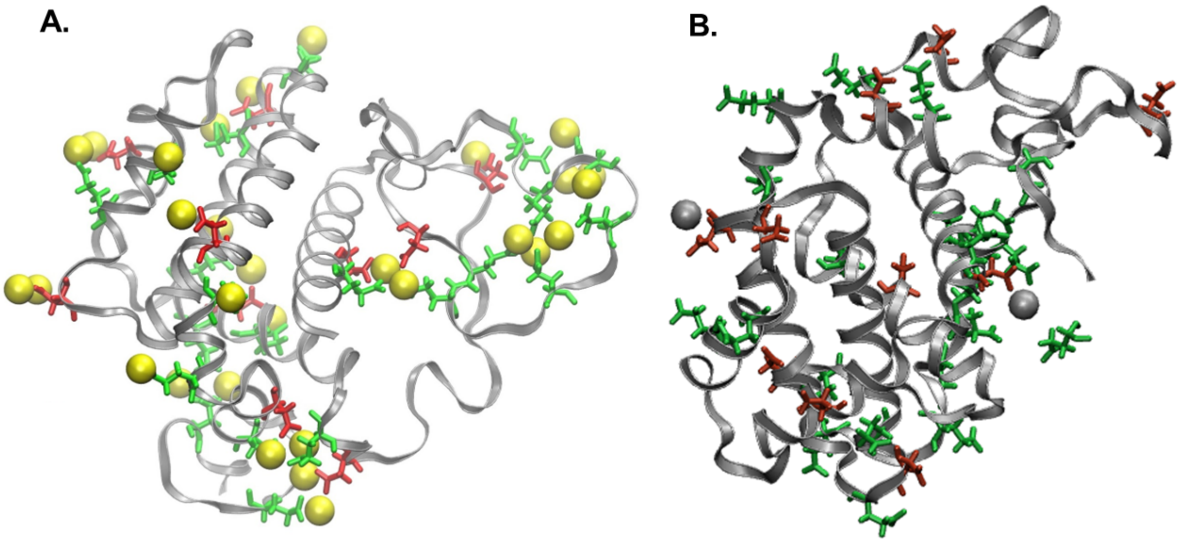

Figure 2.3: Representative simulation snapshots of divalent interactions with Bcl-xL soluble head. Aspartic residues are colored in red and glutamic residues are colored in green. Panel A shows Ca^{2+} ions (yellow spheres) interacting with multiple acidic residues simultaneously and multiple acidic residues interacting with the same Ca^{2+} ion. Panel B shows Mg^{2+} ions (gray spheres) interacting sparsely with the soluble head and occasionally single Mg^{2+} ions interact with multiple acidic residues simultaneously.

Similarly, considering the interactions of divalent cations on the Bcl-xL soluble head, simulation snapshots reveal that multiple Ca^{2+} ions can interact with simultaneously with acidic residues (2.3A). Additionally, multiple acidic residues can interact simultaneously with Ca^{2+} ions (2.3A). Conversely, Mg^{2+} ions are revealed to interact sparsely with Bcl-xL soluble head acidic residues (2.3B). These interactions are typical 1:1, though occasional exceptions exist where, like Ca^{2+}, Mg^{2+} ions interact with multiple residues or acidic residues interact with multiple Mg^{2+} ions. In the case of Mg^{2+} these interactions are very short-lived 2.3B.

The disordered loop of the Bcl-xL protein extends from residues 21 to 88 and links helix $\alpha 1$ to helix $\alpha 2$. The disordered loop is composed of residues that lack well-defined secondary structure, and as such, are highly flexible and can be reoriented easily. Previous analyses have shown that Ca^{2+} has long-lived interactions with acidic residues and can serve as a bridge between neighboring acidic charges. Considering this effect on the disordered loop via a contact map, the divalent simulations reveal that Ca^{2+} ions are a key element in

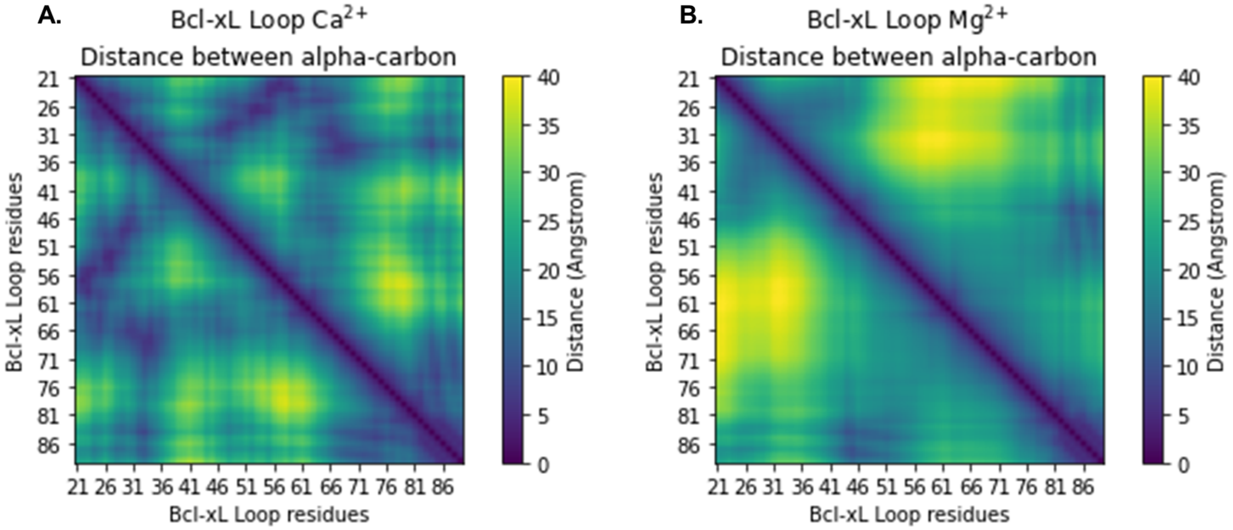

Figure 2.4: Contact map of Bcl-xL disordered loop ($\alpha1 - \alpha2$; residues 21-88) in differing divalent conditions, Ca^{2+} and Mg^{2+}. Panel A shows Ca^{2+} promotes more close interactions between disordered loop residues as shown by the darkened regions. Particularly, residues 21 to 36 interact readily with residues 41 to 66, and residues 66 to 88 interact readily with each other. Panel B shows much more diffuse interactions among the Mg^{2+} simulation as shown by the brighter regions overall.

maintaining a collapsed loop and that residues 21 to 36 interact consistently with residues 41 to 66 and residues 66 to 88 interact readily with each other (2.4A). These interactions are significantly muted in the Mg^{2+} simulation and the transient nature of the Mg^{2+} ion prevent the consistent collapsed formation seen in the Ca^{2+} simulation (2.4B).

2.3.3 Ca^{2+} interactions collapse disordered loop while Mg^{2+} interactions exhibit a dynamic loop

Considering the visual presentation of the disordered loop during simulation, the Ca^{2+} simulation reveals a loop that has condensed onto the soluble head and remains in a collapsed state for long periods of time. Figures 2.5A and 2.5B show the Ca^{2+} simulation at 3.6 Å and 4.4 Å, respectively, and during this entire 0.8 Å time span, the loop remains in a near identical collapsed state. After this period, the loop extends slightly for a few single digit

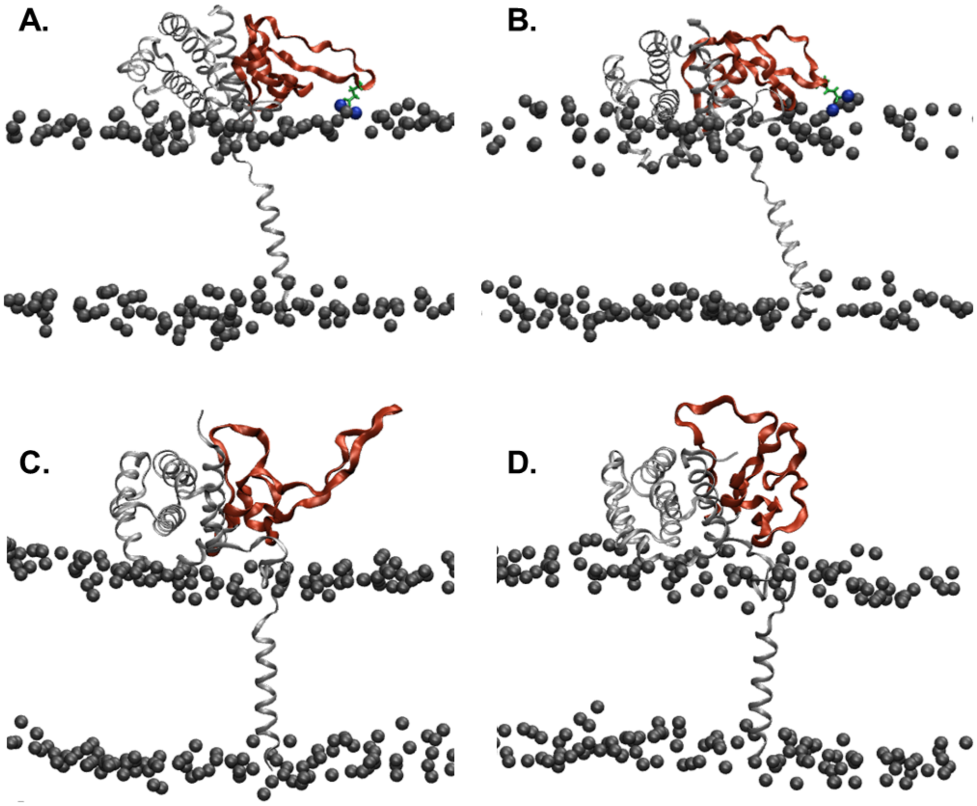

Figure 2.5: Simulation snapshots showing a long-lived, collapsed loop for Ca^{2+} and a more dynamic loop for Mg^{2+}. Panels A & B depict a similar collapsed state of the loop (red ribbon) in the Ca^{2+} condition at 3.6 μs and 4.4 μs, respectively. The loop remained collapsed throughout this 0.8 μs interval and this collapse is relatively consistent throughout the equilibrated portion of the trajectory. Panels C & D depict a fluctuating loop with dynamic character in the Mg^{2+} condition. These panels have a 50 ns differential and show the loop moving from extended to collapsed formation. This fluctuating behavior is consistent throughout the equilibrated portion of the trajectory.

nanoseconds before returning to this same collapsed conformation. Conversely, the Mg^{2+} simulation is observed to undergo rapid fluctuation between an extended and collapsed loop conformations (2.5C & 2.5D). Figures 2.5C and 2.5D represent two snapshots with 50 ns between them and serve to illustrate the fluctuation in conformation for the disordered loop.

The consistent collapse of the disordered loop seen in the Ca^{2+} simulation and the fluctuations between extended and collapsed seen in the Mg^{2+} simulation are further exemplified in Figure 2.6. The radius of gyration of the disordered loop in the Mg^{2+} simulation is seen to have strong and rapid fluctuations that very rarely entire the regime seen in the Ca^{2+}

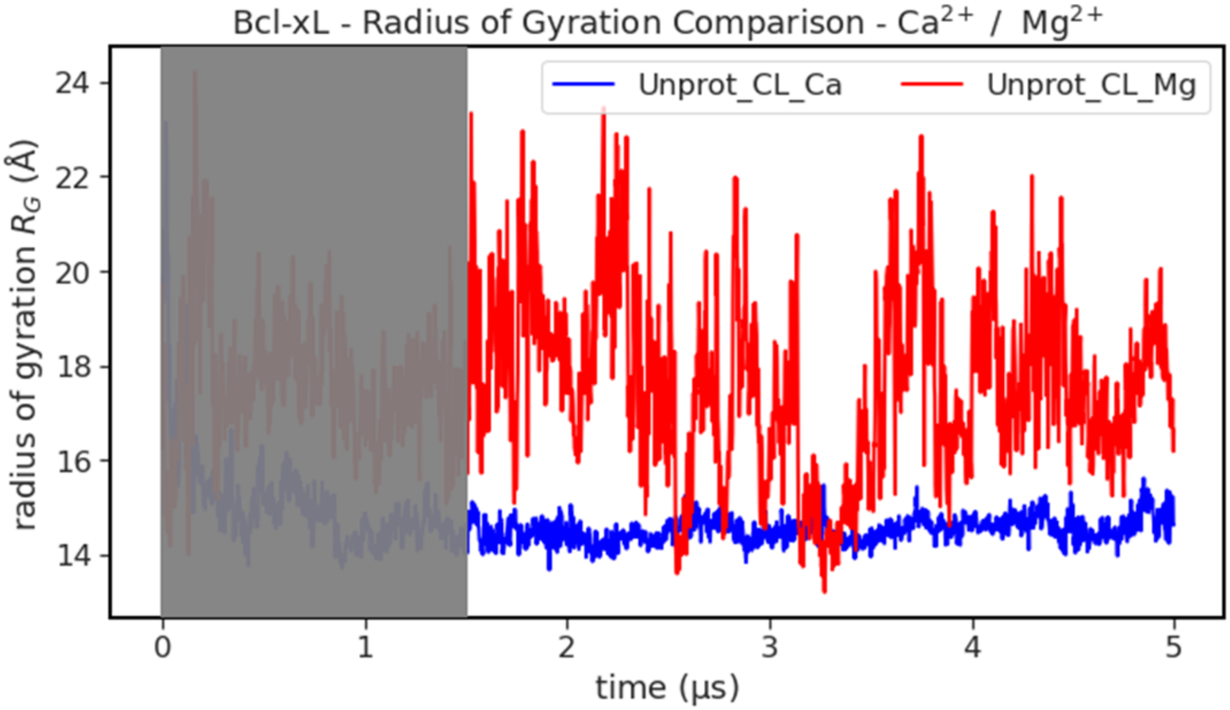

Figure 2.6: Radius of gyration of the Bcl-xL disordered loop for both divalent conditions, Ca^{2+} and Mg^{2+}. Ca^{2+} (blue) shows a consistent low radius of gyration value for the equilibrated portion of the trajectory (non-equilibrated portion blocked out in gray), and suggests a collapsed loop is consistent throughout the simulation. Mg^{2+} (red) shows strong fluctuations in radius of gyration between 23 Å and 13 Å, with most of the values being above that achieved in the Ca^{2+} (blue) simulation. The Mg^{2+} (red) simulation suggests dynamic behavior of the loop, changing between extended and collapsed formation throughout the simulation.

simulation. These differences are likely due to the nature of the direct and long-lived Ca^{2+} interactions as opposed to the water-bridged Mg^{2+} interactions.

2.4 Discussion & Conclusions

While the prevailing models for activation and regulation of Bcl-xL hypothesize that dynamic changes in cardiolipin content in the mitochondrial outer membrane are the most important variables, the role of divalent cations remains relevant due to their strong interactions with anionic lipids and acidic residues on the protein. Both Mg^{2+} and Ca^{2+} serve to bridge interactions between negative charge centers, however Ca^{2+} has much longer lived and consistent interactions due to the direct coupling between Ca^{2+} ions and lipids or residues. The role of Mg^{2+} appears to be bit more nuanced as these interactions are bridged by water, making them weaker and short-lived.

Physiologically, 1 mM to 2 mM of Ca^{2+} or Mg^{2+} are typical, however when considering these interactions in simulation, much higher than physiological concentrations of divalent cations were used in an effort to sample a reasonable amount of ion interactions (100 mM of Ca^{2+} or Mg^{2+}). As such, these simulations provide meaningful evidence of the difference in interactions between these divalent cations, but they do not correlate well with wet-lab experimental conditions, and so it would be prudent to perform studies regarding the conformation of the loop in wet-lab conditions for comparison.

The results presented here provide a rationalization for differences observed in experiments with Ca^{2+} or Mg^{2+} prevalence. Further work is necessary to understand the specific role of changing cardiolipin concentrations within these ionic environments and how changes in anionic lipid concentration affect Bcl-xL activation and regulation. This current work illuminates the difference in effect observed for divalent cations Ca^{2+} and Mg^{2+}.These differences point to the important role that divalent cation concentration can have on protein-membrane binding and the stable conformations of membrane inserted proteins.

2.5 Materials & Methods

2.5.1 Simulation Systems

A model of the full-length Bcl-xL protein in a membrane-anchored configuration was constructed by combining two solution NMR structures: one lacking the C-terminal helix (PDB

ID: 1LXL; residues 1–222)[98] and another of the isolated C-terminal helix (PDB ID: 6F46; helix $\alpha8$, residues 209–231)[115]. After aligning the C-terminal helix along the Cartesian z-axis, the two structures were superimposed and joined at residue Gln-207 to generate a model for the membrane anchored full-length Bcl-xL, where the C-terminal helix is in a transmembrane orientation. For each simulation, Bcl-xL was anchored into the membrane by embedding the C-terminal helix in the lipid bilayer such that the Trp-213 residue was just below the lipid phosphate groups and the soluble folded domain was within 4 Å of the membrane surface. The membrane-anchored Bcl-xL model was incorporated into four different simulation systems, each with one of two protein protonation states to which all Bcl-xL acidic and histidine residue sidechains were protonated or unprotonated (hereafter identified as protonated or deprotonated configurations, respectively); and one of two ion compositions: 100 mM $CaCl_2$ and 100 mM $MgCl_2$. The simulation system setup was performed with CHARMM-GUI[67, 66, 173, 68, 83, 113].

2.5.2 Initial Molecular Dynamics Simulations

The initial equilibration of the simulation systems was performed with NAMD 2.11[110]. Each system was subjected to 50,000 steps of conjugate gradient energy minimization, followed by a 400-ps run at constant temperature (310 K) and pressure (1 atm) with harmonic restraints on the protein-backbone atoms and the PC carbonyl carbons using a decreasing force constant equal to 10, 5, 2, 1, 0.5, 0.2, 0.1, and 0.05 $\text{kcal}\cdot\text{mol}^{-1}\cdot\text{Å}^{-2}$. Unrestrained dynamics were then run for 10 ns on the unprotonated simulations, 7 ns on the protonated 100% POPC simulation, and 15 ns on the protonated 2:1 POPC:TOCL simulation. The CHARMM36[74, 10] force fields were used for the protein, lipids, and ions, and the TIP3P model was used for water[69]. The smooth particle-mesh Ewald summation method[37, 30] was employed for the calculation of electrostatic interactions. Short-range real-space interactions were cutoff at 12 Å, employing a force-based switching function. A reversible multiple-time step algorithm[45] was used to integrate the equations of motion with a time step of 1 fs for electrostatic forces, short-range non-bonded forces, and bonded forces. A Langevin scheme was used for temperature control and a Nosé–Hoover–Langevin piston[92, 38] was used for pressure control.

2.5.3 Microsecond-Timescale Molecular Dynamics Simulations

After initial equilibration, all simulation systems were transferred to Anton2, a special purpose supercomputer for biomolecular simulations, and run for 5.0 µs each[133]. The CHARMM36 force field[74, 10] was used for the protein, lipids, and ions, and the TIP3P model was used for water[69]. The r-RESPA algorithm[152] was used to integrate the equations of motions with a time step of 3 fs for long-range non-bonded forces and a 1 fs time step for both short-range non-bonded and bonded forces. The k-Gaussian split Ewald method[132] was used for the long-range electrostatic interactions. The SHAKE algorithm[125] was employed to constrain all hydrogen atom bond lengths. Simulations were performed at a constant temperature (310 K) and pressure (1 atm) using Nosé–Hoover chains[91] and the Martyna–Tobias–Klein barostat[92]. The RESPA algorithm, temperature control, and pressure control were implemented using the multigrator scheme[86].

2.5.4 Trajectory Analysis

Analyses were performed with VMD[58] and custom Python scripts. Molecular graphics were generated with VMD.

Chapter 3

Ca^{2+}-Dependent Interactions Between Lipids and the Tumor-Targeting Peptide pHLIP

Victor Vasquez-Montes, Vivek Tyagi, Eden Sikorski, Alexander Kyrychenko,
J. Alfredo Freites, Damien Thévenin, Douglas J. Tobias, and Alexey S. Ladokhin

3.1 Abstract

Cancerous tissues undergo extensive changes to their cellular environments that differentiate them from healthy tissues. The changes in cell environment include changes in extracellular pH and Ca^{2+} concentrations, and the exposure of phosphatidylserine (PS) to the extracellular environment, which can modulate the interaction of peptides and proteins with the plasma membrane. Deciphering the molecular mechanisms of such interactions is critical for advancing the knowledge-based design of cancer-targeting molecular tools, such as pHLIP (pH-Low Insertion Peptide). Here, we explore the effects of PS, Ca^{2+}, and peptide protonation state on the interactions of pHLIP with lipid membranes. Cellular studies demonstrate that levels of exposed PS on the plasma membrane promote pHLIP targeting. The magnitude of this effect is dependent on extracellular Ca^{2+} concentration, indicating that divalent cations play an important role in pHLIP targeting in vivo. The targeting mechanism is further explored with a joint study using fluorescence and circular dichroism experiments in model membranes as well as microsecond-timescale all-atom molecular dynamics simulations. Our results demonstrate that Ca^{2+} is engaged in coupling peptide-lipid interactions in the unprotonated transmembrane conformation of pHLIP. The simulations reveal that while the pH-induced insertion leads to a strong depletion of PS around pHLIP, the Ca^{2+}-induced insertion has the opposite effect. Thus, extracellular levels of Ca^{2+} are crucial to link cellular changes in membrane lipid composition with the selective targeting and insertion of pHLIP. The Ca^{2+}-dependent coupling between pHLIP sidechains and PS provides atomistic insights into the general mechanism for lipid-coupled regulation of protein-membrane insertion by divalent cations, relevant to many cellular processes.

3.2 Introduction

Characteristic differences in pH, ionic, and charged macromolecule concentrations between tissues, cells, and organelles can trigger functionally relevant structural rearrangements in protein systems transitioning between different environments. Many membrane-active peptides and proteins undergo conformational switching that is associated with the water-to-membrane partitioning. Proteins in this group include bacterial toxins[109, 87], viral entry proteins[168], antimicrobial peptides[180], cancer-targeting peptides[121, 120, 165], and Bcl-2 apoptotic regulators[139, 159]. Their significant involvement in human disease and treatment makes them fundamentally important to the biomedical field and the focus of many studies. Unfortunately, our knowledge of the basic mechanism of conformational switching in membrane systems is often lacking, impeding our ability to predict protein-lipid interactions and the resulting conformations under physiological conditions. Specifically, the role of lipid composition and divalent cations in modulating these interactions remains under-explored, despite the mounting evidence of their physiological importance in triggering (together with [H+] differences) functionally relevant conformational changes[159, 22, 146, 123, 154, 184, 138, 31, 171].

Our ability to target or manipulate these processes can therefore be beneficial for human health. For example, the membrane insertion of the pH Low Insertion Peptide (pHLIP) has recently been used to target drugs to cancer cells[121, 120, 4, 6, 156]. Because tumors produce slightly acidic extracellular environments[51, 29], it has been assumed that the highly selective cancer-targeting action of pHLIP is solely related to this acid-induced insertion. Solid tumors, however, are also characterized by a well-established dysregulation of plasma membrane lipids that leads to the partial redistribution of the anionic lipid phosphatidylserine (PS) from the inner leaflet of the plasma membrane to the outer leaflet[154, 184]. The extracellular exposure of the PS-containing outer leaflet imparts an anionic character to the cell exterior that differentiates it from the zwitterionic exterior of healthy cells[123, 147]. The impact of exposed PS on the interaction of peptides/proteins with cancer cells remains unclear.

In the case of pHLIP, our recent publications demonstrate that its selective targeting and insertion mechanism involves an intimate coupling between pH, extracellular divalent cations, and membrane lipid composition[76, 160, 157]. Here we expand on these results and investigate the intricate relationship between PS lipids and physiological levels of divalent cations on the tumor targeting and selectivity properties of pHLIP. To this end, we performed a series of cellular and biophysical studies in combination with microsecond timescale all-atom molecular dynamics (MD) simulations. Our results show that the presence of Ca^{2+} is crucial to link the effects of elevated PS levels in cancer cells to the cellular targeting of pHLIP. MD simulations revealed extensive Ca^{2+}-mediated interactions between pHLIP acidic sidechains and membrane lipids that stabilize the unprotonated transmembrane form of pHLIP. They also demonstrate that the pH- and Ca^{2+}-driven insertion, produce different local distributions of PS lipids around pHLIP. These results highlight the significance of divalent cations on protein-membrane interactions and show that they must be considered to understand peptide-membrane interactions in biological settings and the design of membrane interacting peptides.

3.3 Results

3.3.1 Ca^{2+} enhances the effects of phosphatidylserine on pHLIP cellular targeting

The effect of extracellularly exposed phosphatidylserine (PS) on pHLIP cellular targeting was measured by flow cytometry using a fluorescently labeled pHLIP conjugate. Measurements were performed on two cell lines with different levels of exposed PS, as confirmed by Annexin V binding (Fig. 3.6): LNCap cells (high PS) exhibit twice as much PS at its surface than HEK293 cells (low PS), a fold difference consistent with what has been observed between cancerous and non-cancerous cell lines.

At physiological pH 7.4, AlexaFluor488-tagged pHLIP showed minor interactions with cells in the absence of divalent cations, consistent with previously published results[160] (Fig. 3.1). This interaction was, however, enhanced either by the presence of 1.8 mM Ca^{2+} (mimicking total extracellular [divalent cation]) at pH 7.4 or mild acidification to pH 7.0 (resembling tumor tissue pH[51, 29]). The former results in a 3.2-fold increase in pHLIP cellular interactions, while a 1.6-fold increase was observed for the latter regardless of [Ca^{2+}]. The

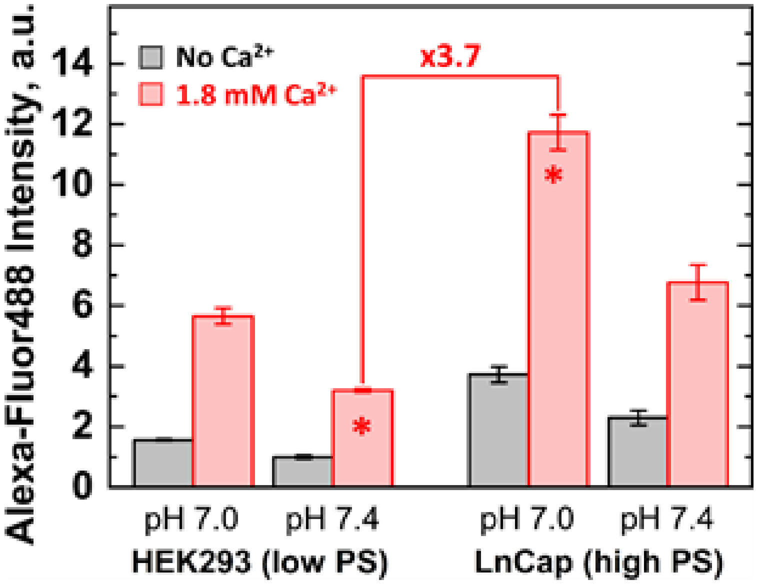

Figure 3.1: Modulation of the cellular targeting of pHLIP by phosphatidylserine (PS) and Ca^{2+}. Flow cytometry measurements of pHLIP N-terminally conjugated to AlexaFluor-488 in cell lines with different levels of exposed plasma membrane PS. Differences in outer leaflet PS levels were determined by Annexin V (Fig. 3.6). Mild acidification alone (in the absence of Ca^{2+}) resulted in an average 1.6-fold increase in pHLIP cellular interactions, while the addition of 1.8 mM Ca^{2+} at pH 7.4 led to a 3.2-fold increase. The substantial increase observed in the presence of Ca^{2+} (red) points to its significant role in the cellular targeting of pHLIP at the pH range produced by tumors. These effects were further enhanced by larger levels of exposed PS in the plasma membrane. A 3.7-fold increase in pHLIP cellular interactions (indicated by the asterisks) was observed under conditions that recapitulate cellular differentiation at 1.8 mM Ca^{2+} to represent extracellular divalent cation levels. “Healthier cells”: Low PS at pH 7.4, “cancerous cells”: High PS at pH 7.0.

Ca^{2+}-induced increase in pHLIP cellular interactions in both cell lines regardless of pH is consistent with its delivery capabilities into MDA-MB-231 cancer cells in the presence of Ca^{2+}[160], confirming the importance of divalent cations on pHLIP cellular targeting.

The magnitude of the Ca^{2+}-dependent and pH-dependent effects are modulated by the content of extracellularly exposed PS at the plasma membrane. The presence of higher levels of exposed PS in LNCap cells resulted in significantly higher pHLIP targeting as compared to HEK293 cells (Fig. 3.1), consistent with our previous observations that the presence of PS promotes pHLIP association with lipid membranes. Notably, the 2- fold increase in pHLIP targeting observed between the two cell lines correlates with the 2-fold difference in the relative level of PS exposure. This is particularly the case in the presence of Ca^{2+} (Fig. 3.1, red), as exemplified by the data indicated by asterisks, which represents changes in cellular conditions during tumor progression: from “healthier tissue” (low PS at pH 7.4) to “cancerous tissue” (high PS at pH 7.0), where a 3.7-fold difference in fluorescent signal was observed between both conditions in the presence of Ca^{2+}.

These results show that changes in the levels of extracellularly exposed PS in the plasma membrane of tumor cells have a substantial role in the cellular targeting of pHLIP and are likely key to its selectivity. The enhanced targeting of PS-rich cells, however, requires the presence of extracellular levels of divalent cations, as their absence in our “cancerous” model (high PS at pH 7.0) only reached 32% of the maximal signal determined in the presence of Ca^{2+}. The effect of exposed PS plus divalent cations on the selectivity of tumor vs healthy cells is expected to be larger in vivo due to the lack of exposed PS in healthy cells[123, 154, 184, 147] (unlike our “healthier” model cells which come from a differentiated cell line with measurable levels of exposed PS).

3.3.2 Low pH and Ca^{2+} induce the same transmembrane state of pHLIP

The combined effects of Ca^{2+} and pH on the bilayer insertion of pHLIP were further analyzed in vitro using a combination of spectroscopic measurements and molecular dynamics (MD) simulations. The membranes contained a 3:1 molar mixture of zwitterionic phosphatidylcholine (POPC) and anionic phosphatidylserine (POPS).

The transmembrane insertion of pHLIP into large unilamellar vesicles (LUV) was determined using Trp fluorescence, taking advantage of its two native Trp residues. The extensive use of Trp fluorescence on pHLIP studies provides well-established benchmarks for its two membrane-associated states (interfacial and transmembrane) in different lipid

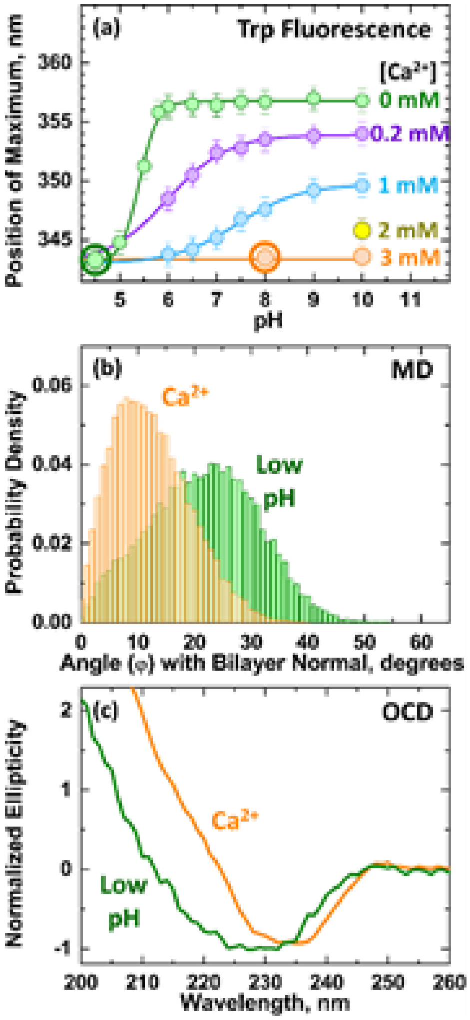

Figure 3.2: Protonation-dependent and independent insertion of pHLIP in anionic membranes (3:1 POPC:POPS). The transmembrane insertion of pHLIP is produced by acidity-induced protonation (green) or the presence of divalent cations (orange). (a) Transmembrane insertion of pHLIP at various [Ca^{2+}] determined by Trp fluorescence. Extracellular levels of Ca^{2+} promote the pH-dependent insertion of pHLIP, resulting in a pK50 shift. Ca^{2+} also induces the protonation independent insertion of pHLIP. Large circles represent two conditions in which the rest of the measurements were performed: low pH (green); neutral pH with Ca^{2+} (orange). (b) Peptide tilt angles (Φ) were calculated by measuring the deviation of the helix axis from the bilayer normal. Differences in width and peak position of the corresponding tilt angle distributions suggest Ca^{2+} promotes a more stable orientation of the helix with small-angle deviations from the membrane normal. (c) Oriented circular dichroism (OCD) spectra of pHLIP at low pH or in the presence of Ca^{2+}. Both conditions produced a single minimum at 230 nm, confirming their transmembrane orientation[16, 174]. The broadening of the low pH sample below 230 nm is consistent with a larger tilt relative to the bilayer normal[16, 174].

compositions[76, 157, 130, 9, 137]. In the case of POPS-containing membranes, the interfacial form of pHLIP is characterized by a Trp λMax 357 nm, while its transmembrane form has a Trp λMax 343 nm[76, 157]. In the absence of divalent cations, the addition of 3:1 POPC:POPS LUVs at pH 10 produced a Trp λMax 356 nm, consistent with its interfacial state (Fig. 3.2a, green). The gradual increase in Ca^{2+} at this pH, however, led to significant decreases in fluorescence maximum values until saturation was achieved at 3 mM Ca^{2+}, where a Trp λMax 343 nm, characteristic of pHLIP's transmembrane state, was obtained (Fig. 3.2a, orange). Acidification to pH 4.5 in the absence of Ca^{2+} produced an equivalent Trp λMax as the one determined at pH 10 and 3 mM Ca^{2+}. The equivalent Trp λMax obtained by acidification or Ca^{2+} indicates that both conditions produce pHLIP conformations in the bilayer that place the Trp sidechains in similar environments.

The presence of Ca^{2+} had the added effect of shifting the pH-dependent insertion of pHLIP towards physiological pH ranges. For example, the presence of 1 mM Ca^{2+} results in a pK50 of 7.3 (Fig. 3.2a, cyan), which corresponds to a 2-pH unit shift compared to the pK50 observed in the absence of Ca^{2+} (Fig. 3.2a, green). The combination of both Ca^{2+}-induced effects results in considerably larger populations of membrane-inserted pHLIP at physiological ranges of pH (7.4 - 7.0) compared with measurements in the absence of Ca^{2+}.

3.3.3 Transverse position of pHLIP at low pH and in the presence of Ca^{2+}

To study the role of divalent cations on the interactions of pHLIP with lipids, we performed two-microsecond timescale all-atom MD simulations of pHLIP embedded in a 3:1 POPC:POPS lipid bilayer: a "low pH" condition, where all pHLIP acidic residues are protonated; and a "Ca^{2+}" condition, where pHLIP is at neutral pH, modeled as a singly protonated aspartate residue (D25) in the presence of 0.1 M $CaCl_2$ (see Materials and Methods). All acidic residues (except D25) were left unprotonated in the latter due to their interfacial positioning in constant-pH simulations of transmembrane pHLIP[16], where they potentially serve as Ca^{2+}-coordinating moieties. Meanwhile, D25 (located near the middle of the bilayer[16]) was set in a protonated state to reduce its thermodynamic penalty to be inserted in the bilayer.

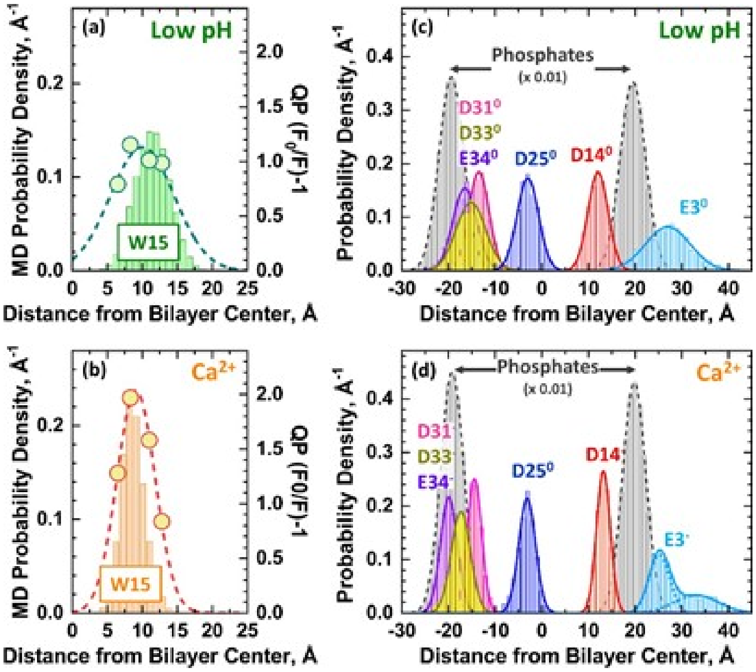

Figure 3.3: Transverse distributions of key residues in transmembrane pHLIP. (a, b) Comparison between experimentally determined W15 bilayer depth penetration by bromolipid-quenching (circles) and its distribution in the bilayer determined by MD (bars). The quenching profile (QP) of pHLIP-W15 (dashed line) indicates the most probable depth of the residue. The profile was obtained by fitting the data to a double Gaussian distribution as described by the distribution analysis methodology[78]. The corresponding probability density histograms from the MD simulations (shown as bars) are highly consistent with the experimental results and recapitulate differences in depth and distribution width at (a) low pH (MD: all E and D protonated, QP: pH 4) and (b) in the presence of Ca^{2+} (MD: protonated D25, QP: 2 mM Ca^{2+} at pH 8). (c, d) The acidic residue distributions from the MD simulations yield equivalent positions for both Low pH and Ca^{2+} conditions. The decrease in distribution width observed for W15 in the presence of Ca^{2+} is also observed in the acidic residues. All of the distribution profiles are well described by a single Gaussian distribution, except for E3 in the presence of Ca^{2+}, which was better represented by a sum of two Gaussians. The corresponding distribution parameters are summarized in Table 3.1. Distributions of phosphates in each bilayer are shown in grey as a visual reference of the bilayer.

First, we compared the topology of transmembrane pHLIP in both simulations using the tilt angles generated between the peptide helical axis and the lipid bilayer normal (Figs. 3.2 and 3.7). The corresponding distributions (Fig. 3.2b) show that pHLIP in the presence of Ca^{2+} adopts a more perpendicular orientation (Fig. 3.2b, orange) than the one observed under the low pH condition (Fig. 3.2b, green). These results were confirmed by oriented circular dichroism spectroscopy (OCD), which allows the differentiation between the transmembrane and interfacial α-helices[16, 174]. OCD measurements at pH 8 in the presence of Ca^{2+} or low pH (pH 4, no Ca^{2+}) yielded spectra with a single minimum around 230 nm (Fig. 3.2c), consistent with transmembrane helices[16, 174] (31, 32). The spectrum measured at low pH, however, presented a broader minimum (Fig. 3.2c, green) as compared to the spectrum in the presence of Ca^{2+} (Fig. 3.2c, orange). Given that measurements at low pH were conducted at pH 4, where pHLIP is in its inserted conformation[101, 5], the spectral broadening was attributed to a higher tilt angle as compared to the spectrum in the presence of Ca^{2+}[16, 174], which is consistent with the MD simulations (Fig. 3.2b).

The MD simulation results were further validated by the experimental determination of the depth of pHLIP penetration in the bilayer at low pH and in the presence of Ca^{2+}. The bilayer depth of W15 was used as a reference point to compare the insertion of pHLIP in the simulations and experiments. W15 represents one of the two native Trp in pHLIP and resides below the phosphate level in the transmembrane form of pHLIP induced by low pH[135]. Experimental determination of Trp depth was performed by depth-dependent quenching using brominated lipids[81], which contain bromine atoms attached at various depths to the acyl chains[77, 78, 80]. (To ensure the selectivity, the other native W9 was replaced with F, which does not affect membrane interactions[71]).

Quenching measurements were performed using POPS-containing LUVs with a 50% molar ratio of brominated PC lipids. The resulting quenching data was compared to the unquenched sample (F0/F-1) and analyzed using the distribution-analysis (DA) methodology[77, 78, 80]. The bilayer penetration of the residues is reported as their distance from the bilayer center (Fig. 3.3a, b). Results from depth-dependent quenching experiments were fitted using a double Gaussian distribution to account for the quenching from the trans leaflet (Fig. 3.3a, b). The resulting quenching profiles (QP) are used to determine the most probable depth (hm) of the measured Trp[77, 78, 80], which corresponded to 10.0 ± 0.7 Å and 9.1 ± 0.1 Å away from the bilayer center at low pH and in the presence of Ca^{2+}, respectively. The distributions of W15 depths determined by the MD simulations were consistent with the quenching results (Fig. 3.3) and captured the decrease in distribution widths in the presence of Ca^{2+}. All calculated parameters are summarized in Table 3.1.

Having validated the MD simulation trajectories with the comparison to spectroscopic measurements, we used the MD simulation results to generate insights into the role of Ca^{2+}-mediated interactions and pHLIP protonation in stabilizing pHLIP in a transmembrane configuration in PS-containing membranes. To further characterize the pHLIP configuration, we compared the bilayer distributions of all acidic residues (E3, D14, 25, D31, D33, and D34) in the low pH and Ca^{2+} simulations (Fig. 3.3c, d). All residues were described by a single Gaussian distribution, except for E3 in the presence of Ca^{2+}, which was best described by a sum of two Gaussian distributions. As in the case of W15 (Fig. 3.3a, b), the distributions of all acidic residues in the Ca^{2+} simulation are narrower than those observed at low pH. This can be attributed to possible stabilizing effects of Ca^{2+}-mediated pHLIP-lipid interactions. Calculated depths and distribution widths are summarized in Table 3.1.

3.3.4 Ca^{2+} mediates interactions between lipids and pHLIP

The pHLIP- Ca^{2+} and pHLIP-Ca^{2+}-lipid interactions were determined from the analysis of the Ca^{2+} first coordination shell in the corresponding radial distribution function between Ca^{2+}-moiety pairs indicated in Fig. 3.4. All charged acidic residues in pHLIP interact

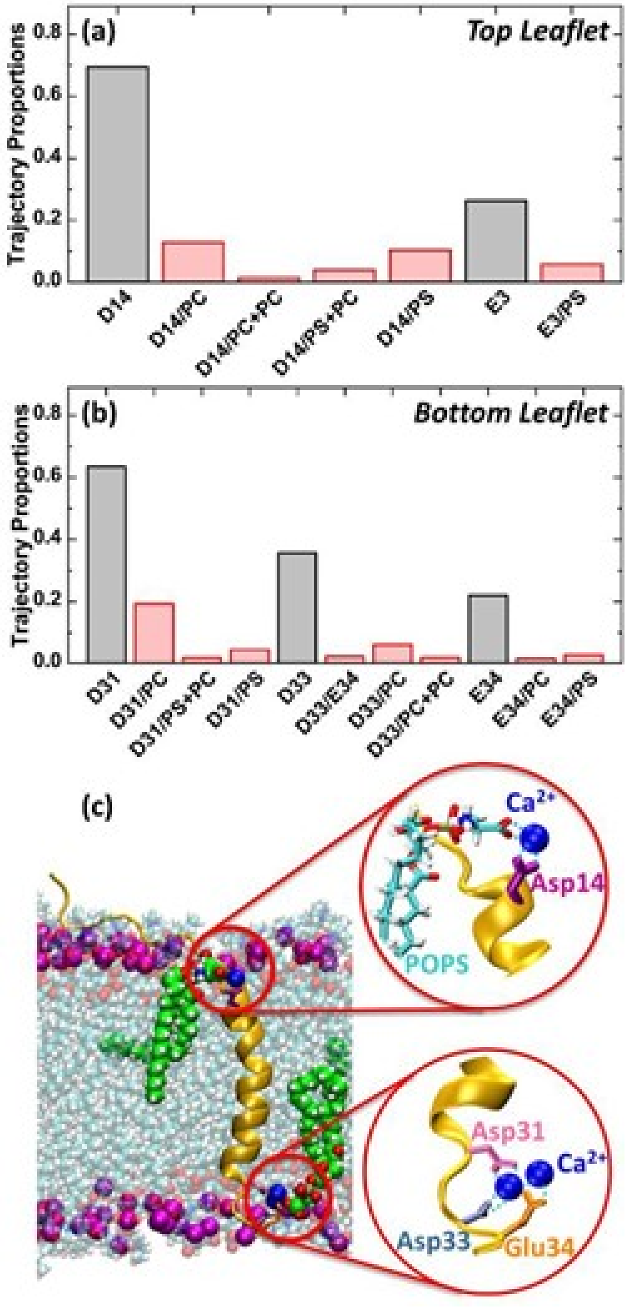

Figure 3.4: Ca^{2+}-mediated coordination of pHLIP and lipids. (a, b) Frequency of pHLIP acidic residue sidechains (gray bars) and both acidic residue sidechains and lipid polar moieties (red bars) in the first coordination shell of Ca^{2+} ions. (c) Simulation snapshot depicting the Ca^{2+}-mediated coordination of acidic residues in pHLIP and lipid polar moieties.

with Ca^{2+}, predominantly without lipid participation (Fig. 3.4a and b, grey). The most frequent interactions involve D14 and D31, both of which are located close to the lipid bilayer polar/apolar interface in either leaflet (Fig. 3.3d). Charged acidic residues were also observed to interact with POPC and POPS lipids through Ca^{2+}-mediated interactions (Fig. 3.4a and b, red; and 4c). The largest number of pHLIP-Ca^{2+}-lipid interactions also involved the acidic residues D14 (top leaflet) and D31 (bottom leaflet), which account for 38% and 36% of all pHLIP-Ca^{2+}-lipid interactions, respectively (Fig. 3.8). The disproportionate number of interactions between D14/D31 and Ca^{2+} compared to shallower residues is likely due to the Ca^{2+}-driven stabilization of unprotonated aspartate and glutamate charges. These interactions would reduce the thermodynamic penalty of positioning charged groups in the membrane and are facilitated by the enrichment of Ca^{2+} near the phosphates and carbonyl oxygen atoms in the bilayer (41). Separating the Ca^{2+}-mediated lipid interactions of pHLIP (Fig. 3.4a and b, red) by lipid species revealed that POPS is involved in 38% of all lipid interactions, despite only comprising 25% of the bilayer lipids, suggesting its enrichment around pHLIP in the presence of Ca^{2+}.

3.3.5 Ca^{2+} modulates PS environment around pHLIP

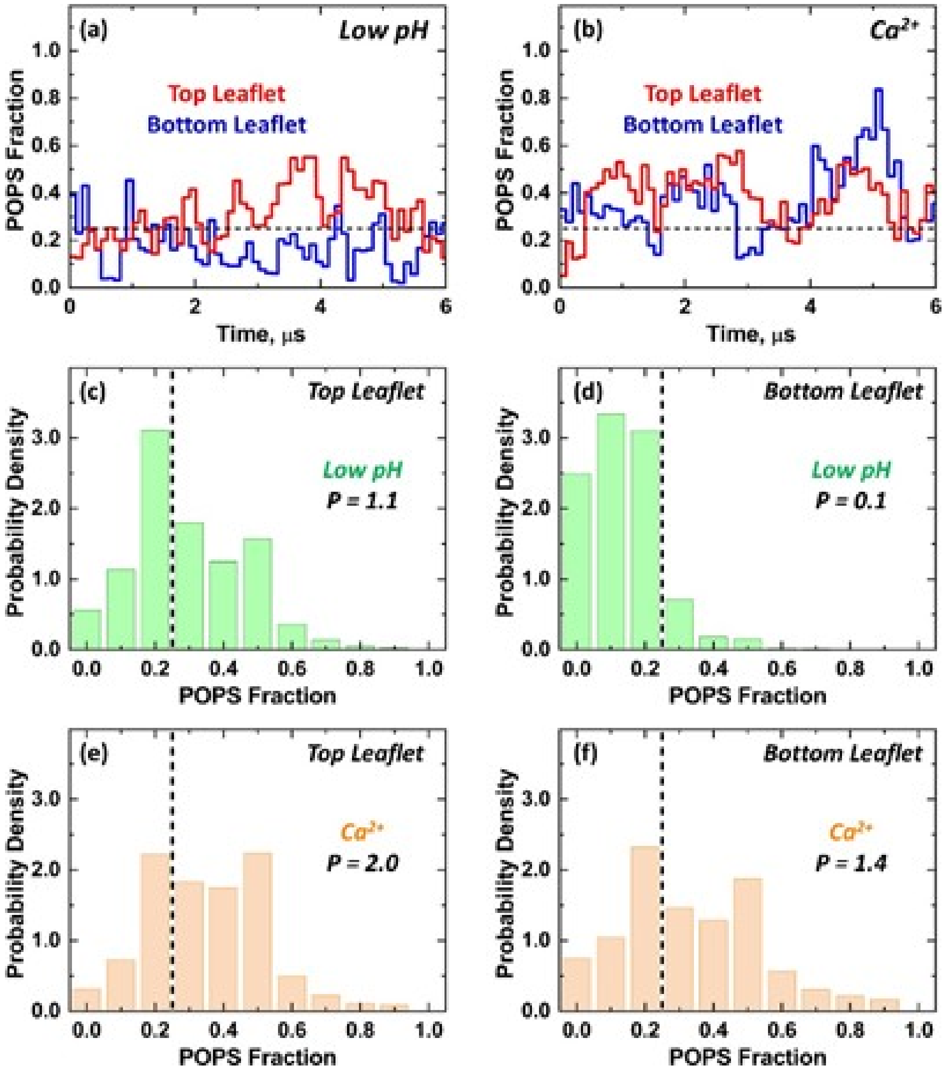

Figure 3.5: Effects of Ca^{2+} and low pH on lipid distribution near pHLIP. (a, b) The POPS fraction within 15-Å of transmembrane pHLIP as a function of time in the top (red) and bottom (blue) leaflets. (c-f) Corresponding POPS distributions at low pH (green) or in the presence of Ca^{2+} (orange). In all panels, the dashed lines indicate the nominal POPS fraction. The P ratio was calculated as a measure of POPS levels in the vicinity of pHLIP in each leaflet as $P = f_{Above}/f_{Below}$, where f_{Above} and f_{Below} correspond to the sum of POPS fractions above and below the nominal level of 25% (indicated by the dashed line).

We then inspected the possible effect of Ca^{2+} on the lipid environment surrounding transmembrane pHLIP, as the content and asymmetry of PS in the bilayer are crucial modulators of pHLIP insertion[76, 157, 130]. The lipid environment in the MD simulations was characterized by calculating the fraction of POPS lipids within a 15-Å radius of the peptide during the course of the simulation (Fig. 3.5). The top and bottom leaflets were treated separately, with the top leaflet helix center measured from the center of mass of residues 13 to 16, while the bottom leaflet helix center was measured from the center of mass of residues 27 to 32. The results were then compared to the nominal fraction of POPS lipids in the simulated bilayer (dashed lines in Fig. 3.5). The time traces and corresponding probability densities for the POPS fraction show significant differences between the low pH and Ca^{2+} simulations with the latter exhibiting larger POPS fractions in the vicinity of pHLIP in both leaflets.

The time traces of POPS fraction show significant differences between the low pH and Ca^{2+} simulations (Fig. 3.5a, b), with the latter exhibiting larger POPS fractions near pHLIP in both leaflets. To describe these differences, we computed the corresponding probability densities for the POPS fraction (Fig. 3.5c-f), and then computed the ratio $P = f_{Above}/f_{Below}$ of the total POPS fraction above (f_{Above}) and below (f_{Below}) the 25% nominal level. A value of P greater or less than one indicates POPS enrichment or depletion in the simulation timescale, The simulation of protonated pHLIP reveals little effect on PS distribution in the top leaflet (P=1.1 Fig. 3.5c) and a ten-fold PS depletion near the peptide in the bottom leaflet (P=0.1 Fig. 3.5d). In contrast, the Ca^{2+} simulation, revealed the enrichment of PS in the vicinity of pHLIP, with P = 2.0 in the top leaflet and P = 1.4 in the bottom leaflet.

3.4 Discussion & Conclusions

The cancer-targeting peptide pHLIP is a promising tool, capable of highly selective delivery of a variety of compounds to cancerous tissues[160, 142, 183, 19, 175]. The traditional model of pHLIP targeting and insertion relies solely on the mildly acidic extracellular environment generated by tumors[121, 5, 118, 119]. Indeed, the ability of the peptide to insert into model membranes at acidic pH has been demonstrated over two decades ago[59]. Our results, however, have demonstrated that the targeting of pHLIP is very complex, relying on the coupling between pH, membrane lipid composition, and extracellular divalent cations (Fig. 3.1, 3.2a and [160]).

The anionic lipid phosphatidylserine (PS) is a prominent modulator of pHLIP membrane interactions[157, 160, 130]. In the plasma membrane of healthy cells, PS is kept on the inner leaflet and is only transferred to the outer leaflet in diseased cells, such as apoptotic or cancerous cells[123, 154, 184, 147]. The exposure of PS imparts an anionic character to the outside of cancer cells that differentiates them from healthy cells and influences protein/membrane interactions. This effect is demonstrated by our cellular data which recapitulate the low targeting of "healthier tissues" (pH 7.4 and low PS) and high targeting to "cancerous tissues" (pH 7.0 and high PS) (Fig. 3.1) observed in animal models[120, 19, 3]. The effect of exposed PS on tumor selectivity is expected to be larger in vivo. Indeed, unlike with the "low PS" cells (HEK293) used in this study (which are differentiated cells with low levels of exposed PS), PS is confined to the cytosolic leaflet of the plasma membrane of healthy cells. Moreover, the effect of PS on pHLIP cellular targeting (and delivery capabilities[160]) is significantly enhanced by the presence of physiological levels of divalent cations (Fig.1, red).

A series of spectroscopic and computational studies were carried out in the presence of Ca^{2+} or at low pH (approximated in the MD simulations by protonating all acidic residues) to study the interactions between pHLIP and PS. All experimental measurements were in good agreement with our MD simulations, e.g., differences in tilt angle between both conditions tested (Fig. 3.2), as well as the depths and distribution widths of W15 (Fig. 3.5).

Together, these measurements show that the presence of Ca^{2+} is crucial to understand pHLIP-membrane interactions in vivo as it introduces several effects to these processes: 1) Ca^{2+} interacts with acidic residues in pHLIP (Fig. 3.4, grey), likely neutralizing their charge and lowering their free energy penalty to reside in the bilayer; 2) The presence of Ca^{2+} facilitates interactions between lipids and unprotonated acidic residues in pHLIP (Fig.

3.4, red). These pHLIP-Ca^{2+}-lipid interactions are likely key to the stability, as well as the proper tilt, of the unprotonated form of pHLIP in the bilayer and link lipid-specific properties to protein-membrane interactions; 3) Ca^{2+} redistributes lipids in the vicinity of pHLIP (Fig. 3.5), which could have implications on the cooperativity of its membrane binding and insertion, particularly, due to the redistribution of PS lipids in cancer cells[123, 154, 184, 147] and the sensitivity of pHLIP to PS asymmetry[130].

The majority of all pHLIP-Ca^{2+} interactions involved D14 and D31 (Fig. 3.4 and 3.8). Both residues have been previously identified to be crucial to the insertion mechanism of pHLIP in the absence of divalent cations. D14, is key to the protonation-dependent insertion of pHLIP and the stability of the transmembrane state[101, 39], while the protonation of D31 is key to the initial insertion steps[104, 48] and transmembrane stability[17]. The critical role of D31 in Ca^{2+}-mediated interactions suggests a possible explanation for the improved tumor selectivity of the clinical variant of pHLIP, pHLIP-Var3[26, 148], where the lack of C-terminal acidic residues (D31, D33, and D34) would prevent the Ca^{2+}-dependent stabilization of its C-terminus in the bilayer at neutral pH, likely reducing its non-specific Ca^{2+}-driven insertion into healthy cells and resulting in a more reliant pH-dependent targeting of cancerous tissues.

Our results highlight the importance of divalent cations such as Ca^{2+} on the interactions, stability, and insertion of peptides into cellular membranes under physiological conditions and indicate that the accurate representation of protein-membrane interactions in vitro require cellular levels of divalent cations. We hypothesize that the stabilizing role of acidic residues in the bilayer by divalent cations is a general mechanism that extends to other systems, facilitating the membrane interaction and insertion of peptides/proteins previously assumed to be unfavorable. For example, the apoptotic regulators Bcl-xL and BAX, previously thought to require activators to transition to lipid membranes, were recently shown to insert into membranes and refold into their active conformations (from soluble states) without the need of canonical activators through a lipid-dependent process that requires cytosolic levels of divalent cations[159].

3.5 Future Work

Our current work on pHLIP focuses entirely on a single membrane composition 3:1 PC:PS, and focuses on the difference between divalent Ca^{2+} and monovalent Na^{+}. Future work on a similar system would attempt to separate those interactions relevant to the divalent cations from those particular to the anionic component of the membrane. In order to accomplish this, we would run simulations of transmembrane pHLIP in 100% POPC membranes with varying ionic conditions, Na^{+}, Ca^{2+}, and Mg^{2+}. This would provide a clearer picture of the effect of different charged cation species.

Another consideration would be running interfacial simulations of pHLIP to better understand the orientation of pHLIP on the membrane prior to insertion. True insertion has been shown to be on the order of seconds in timescales, which is orders of magnitude too long for our most sophisticated simulation systems. However, simulating interfacial pHLIP may still provide key insights into localized lipid behavior, ion-mediated lipid-residue interactions, and orientation and accessibility of pHLIP on the membrane surface.

3.6 Materials & Methods

3.6.1 Materials

POPC (1-palmitoyl-2-oleoyl-*sn*-glycero-3-phosphocholine), POPS (1-palmitoyl-2-oleoyl-*sn*-glycero-3-phospho-L-serine) and all brominated-PC lipids (16:0-18:0(4,5-dibromo) PC, 16:0-

18:0 (6-7BR) PC, 16:0- 18:0 (9-10BR) PC, and 16:0-18:0 (11-12BR) PC) were purchased from Avanti Polar Lipids (Alabaster, AL). AlexaFluor488-maleimide was from Invitrogen (Carlsbad, CA). pHLIP variants used: pHLIP (AAEQNPIYWARYADWLFTTPLLLLDLALLV-DADET), pHLIP-W15 (AAEQNPIYFARYADWLFTTPLLLLDLALLVDADET). Peptides and the fluorescently-labeled conjugate were synthesized, purified, identified, and quantified as previously described[160].

3.6.2 Cell culture

Human embryonic kidney (HEK29) cells were cultured in Dulbecco's Modified Eagle's medium (DMEM) high glucose supplemented with 10% FBS, 100 units/ml penicillin, and 0.1 mg/ml streptomycin. Human prostate adenocarcinoma LNCap were cultured in Rosewell Park Memorial Institute (RPMI) 1640 medium supplemented with % FBS, 100 units/ml penicillin, and 0.1 mg/ml streptomycin. All cells were cultured in a humidified atmosphere of 5% CO_2 at 37°C.

3.6.3 Annexin V quantification

HEK293 and LNCap cells were labeled with AlexaFluor-488 Annexin V (Invitrogen) according to the manufacturer's protocol. Briefly, the cells were harvested and washed once with binding buffer (10 mM HEPES-KOH, 140 mM NaCl, 2.5 mM $CaCl_2$, pH 7.4). The cells were incubated with AlexaFluor-488 Annexin V in binding buffer for 15 minutes at room temperature, washed once with binding buffer, and kept at 4°C until analysis. The amount of bound AlexaFluor-488 Annexin V was analyzed using a BDFacs Canto II flow cytometer equipped with a 488 nm argon laser and a 530/30 bandpass filter. The data was analyzed using FACSDiva version 6.1.1 software. The fluorescence data are expressed as mean arbitrary fluorescence units and were gated to include all healthy mammalian cells.

3.6.4 Cell binding experiments

HEK293 and LNCap cells were harvested and washed with PBS, pH 7.4. AlexaFluor488-pHLIP was solubilized in an appropriate volume of 10 mM HEPES, 19.5 mM NaCl, pH 7.4 so that upon a 2-fold dilution, and after pH adjustment, a treatment concentration of 500 nM was obtained. The cells were incubated with AlexaFluor488-pHLIP at two times the desired concentration for 5 minutes at 37°C. Immediately following the incubation, an equal volume of 10 mM HEPES, 19.5 mM NaCl, pH 7.4 containing either 0 or 3.6 mM calcium was added to bring the final calcium concentration to 0 or 1.8 mM and incubated for an additional for 5 minutes at 37°C. Then, the pH was adjusted using a pre-established volume of 10 mM HEPES buffered with acetic acid, pH 4.0, 19.5 mM NaCl, either 0 or 1.8 mM calcium, and incubated for 10 minutes at 37°C. The cells were then washed at the same pH and calcium concentration as the treatment and fixed with 4% paraformaldehyde (PFA) for 10 minutes at 4°C. The cells were resuspended in PBS and analyzed by flow cytometry as detailed above. Fluorescence was normalized to that observed with HEK293 cells treated at pH 7.4 with 0 mM calcium.

3.6.5 Large unilamellar vesicles (LUV)

The appropriate volume of chloroform lipid stocks was dried using a nitrogen stream and placed under a high vacuum to dry overnight. The dried lipid films were resuspended to a final concentration of 20 mM in 20 mM HEPES buffer + 100 mM NaCl pH 8 and the LUV were prepared by extrusion using a Mini-Extruder (Avanti Polar Lipids, Alabaster, AL) with 0.1 µm nucleopore polycarbonate membranes (Whatman, Philadelphia, PA)[33, 93].

3.6.6 Trp fluorescence spectra

Trp emission spectra were collected on a Fluorolog FL3C-2 Ultrafast steady-state fluorimeter (Jobin Yvon, Edison, NJ) equipped with double-grating excitation and emission monochromators. The experimental temperature was kept at 25°C using a Peltier device from Quantum Northwest (Spokane, WA.). Measurements were performed on 2x10 cuvettes oriented perpendicular to the excitation beam and collected after 20 min incubations using samples containing 2 µM pHLIP and 1 mM LUV.

Samples were excited at 280 nm and Trp spectra were collected between 300-460 nm at 1 nm steps using slits of 2 and 4 nm on the excitation and emission monochromators, respectively. The presented spectra are the average of 3 collected scans. Positions of maximum were determined by fitting the spectra to the log-normal distribution[79].

3.6.7 Depth-Dependent Quenching

Trp fluorescence quenching experiments were performed with the single-Trp pHLIP W15 variant using lipid-attached bromine atoms as the quenching moieties[81]. The change in fluorescence intensity measured with LUV containing brominated lipids located at carbons 4-5, 6-7, 9-10, or 11-12 in the acyl tails of PC lipids residing at known bilayer depths was compared to the unquenched sample (QP(h) = (F0/F(h))-1). The resulting quenching profile was analyzed by distribution analysis[78] which approximates the transverse quenching with a sum of two mirror-imaged Gaussian functions, G(h) where, h_m is the most probable depth of the probe measured from the bilayer center, σ, is the dispersion of the transverse profile, and S corresponds to the overall quenching efficiency.

3.6.8 Oriented Circular Dichroism

Oriented CD (OCD) measurements were performed using a JASCO-810 spectropolarimeter (JASCO, Easton, MD). Spectra were obtained by creating a stack of oriented multilayers on a quartz disc as previously described[160, 170]. Briefly, 0.1 mM pHLIP and a 10 mM lipid mixture containing a 25:75 molar ratio of POPS and POPC were co-dissolved in methanol (1:100 peptide to lipid ratio). The multilayer stack was created by placing 2.5 µL of the peptide/lipid mixture in the center of a 2.5 cm disc. The solvent was then air-dried to a 1 cm diameter and hydrated using warm air at 100% relative humidity. A drop of either 5 mM HEPES buffer pH 4 or 5 mM HEPES buffer pH 8 + 2 mM Ca^{2+} was added in-between each layer of the stack and completely dried before continuing with multilayer stacking. The disc containing the multilayer stack was mounted on a sealed tube with the sample side pointing inwards. An average of 50 scans was collected at eight different orientations at 45° intervals along the central axis. The collected spectra were averaged and the background signal (determined by collecting the spectra of a multilayer stack in the absence of pHLIP) was subtracted. The presented spectra have been normalized to the ellipticity of their respective minimum due to difficulties calculating the peptide concentration along the beam path of each stack.

3.6.9 Simulation Systems

An all-atom model of the pHLIP peptide (AAEQNPIYWARYADWLFTTPLLLLDLAL-LVDADEGG) was generated using the Molefacture Protein Builder plugin in VMD[58]. Residues 14 through 30 were assembled as an ideal α-helix (backbone torsion angles phi = -57°, psi = -47°) based on the prediction by MPEx for the peptide transmembrane region **(MPEx ref)**. Residues 1 through 13, and 34 through 36 were assembled in an extended conformation (backbone torsion angles phi = -180°, psi = 180°), and residues 31 and 32 in a turn conformation (backbone torsion angles phi = -60°, psi = 30°). The model peptide was embedded in a lipid bilayer composed of 1-palmitoyl-2-oleoyl-*sn*-glycero-3- phosphocholine (POPC) and 1,2-palmitoyl-oleoyl-*sn*-glycero-3-phosphoserine (POPS) with a 3:1 POPC:POPS ratio in a transmembrane configuration, with the axis defined by the geometric centers of L21 and D31 parallel to the membrane normal.

Two simulation systems were set up with different solution environments: 0.1 M $CaCl_2$ and 0.1 M NaCl. The simulation system setup was performed using CHARMM-GUI[58]. The $CaCl_2$ simulation system consisted of one pHLIP peptide with D25 protonated, 82 POPC lipids, 28 POPS lipids, 8,557 waters, 30 Ca^{2+} ions, and 28 Cl^- ions, for a total of 40,838 atoms and an initial simulation cell size of 76.8 Å x 73.0 Å x 102.6 Å. The NaCl simulation system consisted of one pHLIP peptide with all acidic sidechains (E3, D14, D25, D31, D33, E34) protonated, 217 POPC lipids, 72 POPS lipids, 17,039 waters, 100 Na^+ ions, and 29 Cl^- ions, for a total of 90,037 atoms and an initial simulation cell size of 107.2 Å x 105.8 Å x 103.6 Å.

3.6.10 Initial Molecular Dynamics Simulations

The initial equilibration of the simulation systems was performed on a conventional high-performance computing cluster using NAMD 2.11[110]. Each system was subjected to 20,000-30,000 steps of conjugate gradient energy minimization followed by a series of eight 80-ps runs at constant temperature (310 K) and pressure (1 atm) with harmonic restraints on the peptide-backbone atoms and the POPC carbonyl carbons with decreasing force constants equal to 10, 5, 2, 1, 0.5, 0.2, 0.1, and 0.05 $\text{kcal}\cdot\text{mol}^{-1}\cdot\text{Å}^{-2}$. Unrestrained simulations were then run for 5-10 ns. The CHARMM36m force field was used to model the peptide[57], the CHARMM36 force field was used for lipids[74, 10], and ions were modeled with the NBFIX terms between Ca^{2+} ions and headgroup oxygens reported by Kim et al.[69]. The TIP3P model was used for water[37]. The smooth particle-mesh Ewald summation method[37, 30] was employed for the calculation of electrostatic interactions. Short-range real-space interactions were cut off at 12 Å, employing a force-based switching function. A reversible time step algorithm[45] was used to integrate the equations of motion with a time step of 1 fs. A Langevin scheme was used for temperature control and a Nosé–Hoover–Langevin piston[92, 38] was used for pressure control.

3.6.11 Microsecond-timescale Molecular Dynamics Simulations

After initial equilibration, both simulation systems were transferred to Anton2, a special-purpose supercomputer for biomolecular simulations, and run for 6 µs each[133]. The same force fields were used for the Anton2 simulations as the equilibration steps. The r-RESPA[152] algorithm was used to integrate the equations of motion with a time step of 7.5 fs for the long-range nonbonded forces and 2.5 fs for short-range nonbonded and bonded forces, and the k-Gaussian split Ewald[132] method was used for the long-range electrostatic interactions. The SHAKE[125] algorithm was employed to constrain hydrogen atom bond lengths. All simulations were performed at constant temperature (310 K) and pressure (1 atm) using Nosé-Hoover chains[91] and the Martyna-Tobias-Klein barostat[92]. The RESPA algorithm, temperature control, and pressure control were implemented using the multigrator scheme[86].

3.6.12 Trajectory analysis

All the distribution analyses were performed on the equilibrated portion of the trajectories, which ranged from 1 µs to 6 µs. The peptide helical axis was defined as the vector connecting the center of mass of pHLIP residues 29 to 31 to the center of mass of residues 21 to 23. The Ca^{2+} coordination shells were defined by the radial distribution function and the center-of-mass of each peptide or lipid moiety. Analyses were performed with VMD (60) and custom python scripts. Molecular graphics were generated with VMD.

3.7 Supplementary Information

Ca^{2+}-Dependent Interactions Between Lipids and the Tumor-Targeting Peptide pHLIP

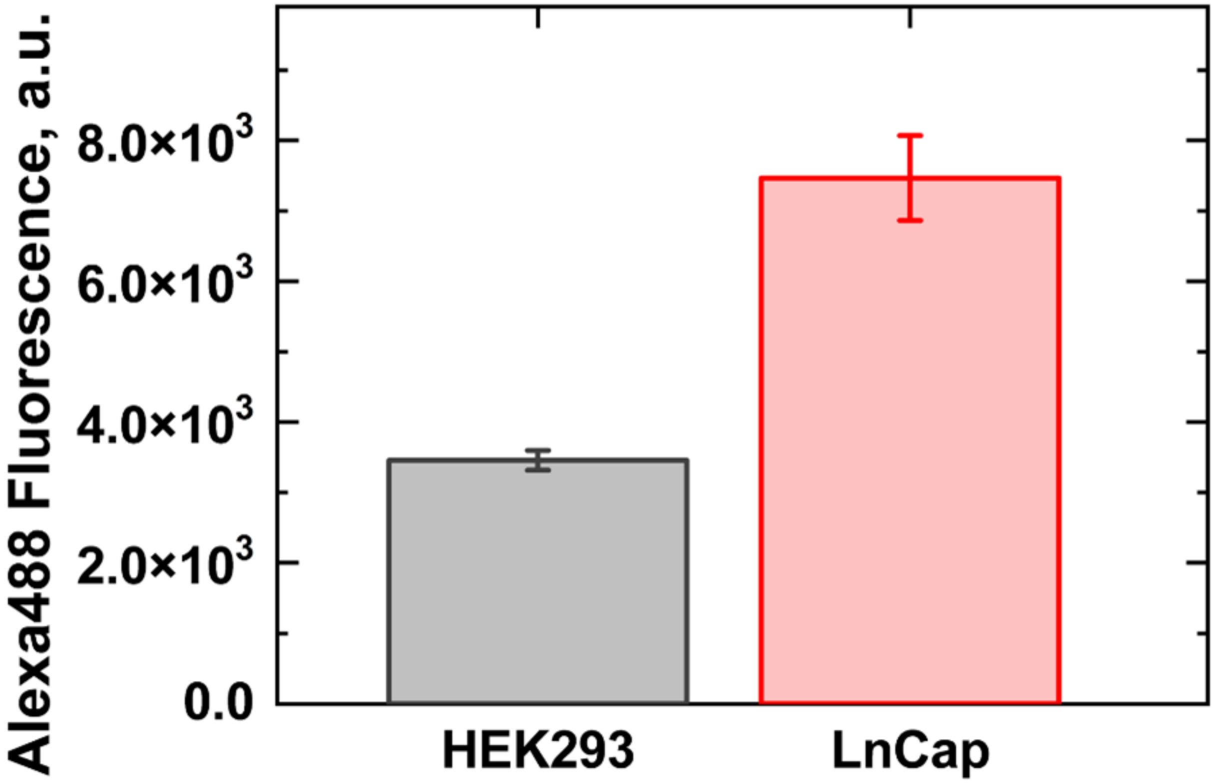

Figure 3.6: Detection of phosphatidylserine (PS) exposure by annexin V binding. Levels of PS on the outer leaflet of HEK293 and LnCap cells were detected by flowcytometry using AlexaFluor488 conjugated Annexin V, as described in the methods section.

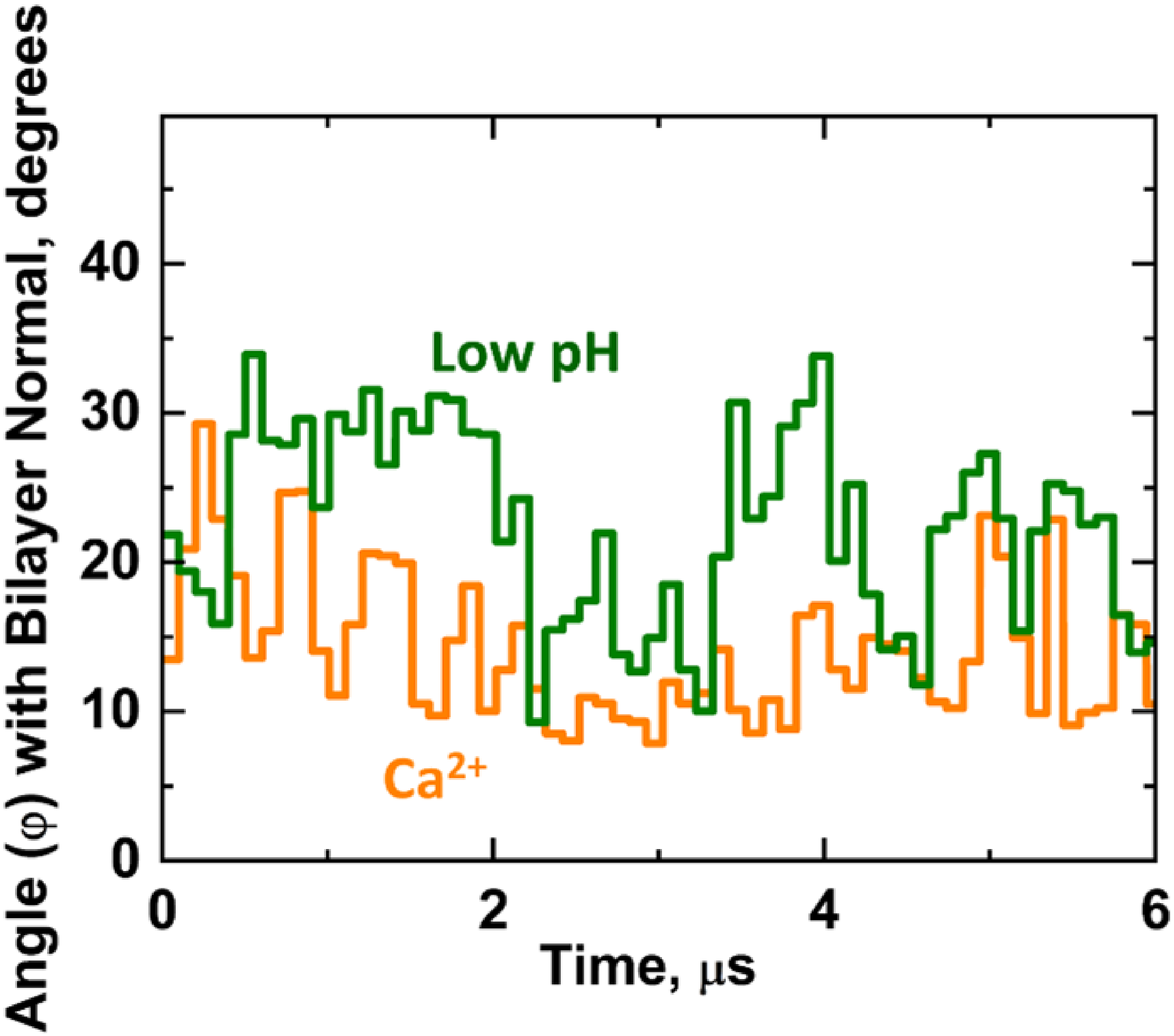

Figure 3.7: pHLIP helix tilt angle as a function of time shown with 100-ns block averaged time-traces. The low-pH (green) simulation shows large fluctuations ranging from 10 to 35 degrees in angle deviation, while the Ca^{2+} (orange) simulation shows fewer large-scale fluctuations suggesting that Ca^{2+} may contribute to enhancing stability of helical orientation in the membrane.

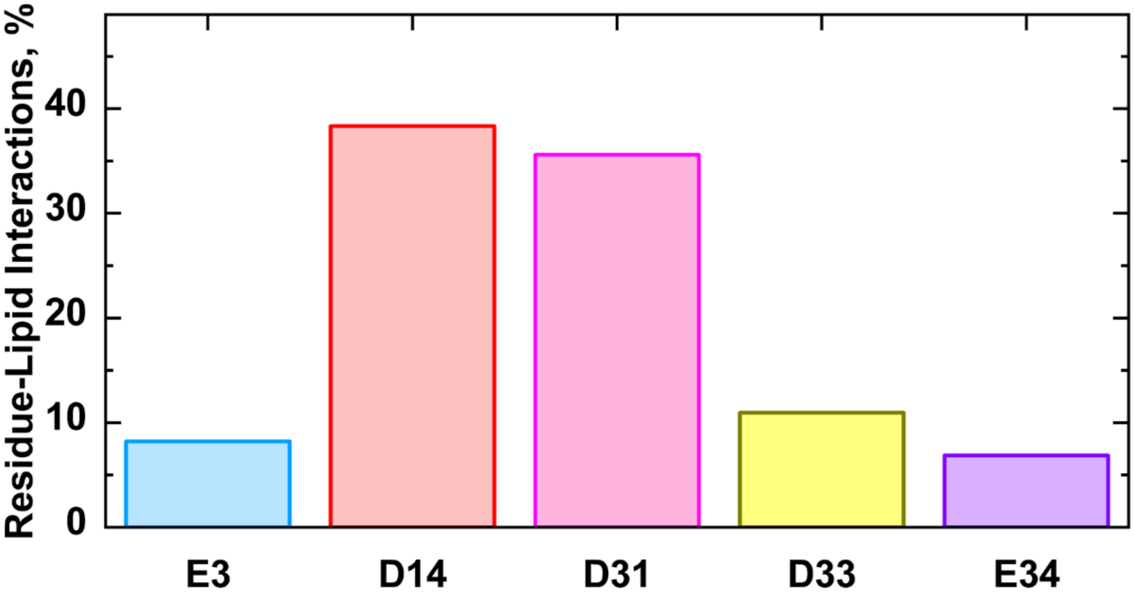

Figure 3.8: Participation of individual residues in Ca^{2+}-mediated pHLIP-lipid interactions. Contribution of all unprotonated acidic residues in pHLIP-Ca^{2+}-lipid interactions. 100% is denoted as the total number of pHLIP-lipid interactions in Fig. 3.4ab as unity proportion, 1.0.

Table 3.1: Gaussian fits of acidic residue distributions in low pH and Ca^{2+} simulations. Parameters were obtained by fitting the MD distributions of the acidic residues shown in Fig. 3.3 to single or double (E3) Gaussian distributions.

Residue	Low pH		Ca^{2+}	
	Distance from Bilayer Center, Å	Full-width at half height, Å	Distance from Bilayer Center, Å	Full-width at half height, Å
E3	27 (Cis Leaflet)	4.8	25.2 & 33 (Cis Leaflet)	2.2 & 3.2
D14	12.1 (Cis Leaflet)	2.2	13.2 (Cis Leaflet)	1.5
D25	3 (Trans Leaflet)	2.3	3.1 (Trans Leaflet)	1.8
D31	13.5 (Trans Leaflet)	2.2	14.4 (Trans Leaflet)	1.5
D33	15.2 (Trans Leaflet)	3.2	17.3 (Trans Leaflet)	1.9
E34	16.5 (Trans Leaflet)	2.5	20 (Trans Leaflet)	1.8

Chapter 4

Single-particle tracking and machine-learning classification reveals heterogeneous Piezo1 diffusion

Vivek Tyagi, Alan T. Ly, Gabriella A. Bertaccini, Elizabeth L. Evans,
J. Alfredo Freites, Medha M. Pathak, and Douglas J. Tobias

4.1 Abstract

The mechanically-activated ion channel Piezo1 is involved in numerous physiological processes. Piezo1 is activated by diverse mechanical cues and is gated by membrane tension. The channel has been found to be mobile in the plasma membrane. We employed single particle tracking (SPT) of endogenously-expressed, tdTomato-tagged Piezo1 using Total Internal Reflection Fluorescence Microscopy in two cell types, mouse embryonic fibroblasts and liver sinusoidal endothelial cells. Application of SPT unveiled a surprising heterogeneity of

Piezo1 mobility in the plasma membrane. Leveraging a machine learning technique, Piezo1 trajectories were sorted into distinct classes (“mobile,” “intermediate,” and “trapped”) by partitioning features that describe the geometric properties of a trajectory. To evaluate the effects of the plasma membrane properties on Piezo1 diffusion, we manipulated membrane composition by depleting or supplementing cholesterol or by adding margaric acid to stiffen the membrane. To address effects of channel activation on Piezo1 mobility, we treated cells with Yoda1, a Piezo1 agonist, and GsMTx-4, a channel inhibitor. We collected thousands of trajectories for each condition, and found that “mobile” Piezo1 in cells supplemented with cholesterol or margaric acid exhibited decreased mobility, whereas Piezo1 in cholesterol-depleted membranes demonstrated increased mobility, compared to their respective controls. Additionally, activation by Yoda1 increased Piezo1 mobility and inhibition by GsMTx-4 decreased Piezo1 mobility compared to their respective controls. The “mobile” trajectories were analyzed further by fitting the time-averaged mean-squared displacement as a function of lag time to a power-law model, revealing Piezo1 consistently exhibits anomalous subdiffusion. This suggests Piezo1 is not freely mobile, but that its mobility may be hindered by subcellular interactions. These studies illuminate the fundamental properties governing Piezo1 diffusion in the plasma membrane and set the stage to determine how specific cellular interactions may influence channel activity and mobility.

4.2 Introduction

The Piezo family of ion channels was discovered over a decade ago and was found to sense and transduce mechanical forces [24]. The importance of Piezo proteins is underscored by the fact that they are highly conserved in many species, including mammals, plants, and protozoa, and are expressed in a wide range of tissues. Piezo channels activate in response to mechanical cues and cause cationic influx [24] and regulate a number of crucial biological processes. These proteins are critical in vascular development [116, 85], lymphatic valve development [103], bone formation [141], blood pressure baroreflex [181], mechanical itch [54] and touch [117, 20], proprioception [172], tactile and mechanical pain [145, 100], skin wound healing [56], and neural stem cell differentiation [107]. Knockouts of Piezo1 are embryonic lethal [116, 85], and Piezo1 mutations are associated with several diseases, including dehydrated hereditary stomatocytosis, and lymphatic dysplasia [65, 88].

The homotrimeric Piezo1, with its triple-blade, propeller-like architecture, has a unique structure compared to other known membrane proteins [127, 40, 47, 182]. The propeller blades consist of repeating four-transmembrane-helix-containing bundles, and are linked to the central pore by the beam and anchor domains [127]. Structural and computational studies of Piezo1 reveal that the channel structure causes local distortion of the membrane, thereby inducing membrane curvature and causing the membrane to adopt a striking bowl-like characteristic [47, 50]. Membrane tension has been shown to gate the channel [84, 143, 25], demonstrating that the channel directly senses forces on the lipid bilayer.

We previously reported that internal cell-generated traction forces from the actomyosin cytoskeleton can activate Piezo1 in the absence of external mechanical stimuli [107, 35]. Using a Piezo1-tdTomato reporter mouse model where the tdTomato fluorophore is knocked in at the Piezo1 C-terminus, we found that the Piezo1 protein is not restricted to focal adhesions, the location of traction forces, and that the channel is surprisingly mobile [35]. Ridone *et al.* similarly found that the channel was mobile using heterologously-expressed Piezo1-GFP, and further showed that cholesterol depletion via methyl-β-cyclodextrin (MBCD) increased channel diffusion and disrupted clustering of Piezo1 [122].

The plasma membrane through which Piezo1 diffuses is a complex environment with considerable structural heterogeneity which may give rise to a variety of interactions between Piezo1 and its surrounding environment [131, 61]. Understanding the nature of Piezo1 mobility can help to elucidate these Piezo1-membrane interactions and thereby the underlying force sensing mechanisms.

Here, we report single-particle tracking (SPT) of endogenously expressed Piezo1-tdTomato channels. Visual examination reveals heterogeneous trajectories that could be classified into three broad categories based on their spatial extent: "mobile" class wherein trajectories displayed relatively large spatial extent, "trapped" trajectories limited to a small area, and an "intermediate" class with a spatial extent in-between the other two categories. We implemented a supervised machine learning approach to objectively classify thousands of trajectories based on their geometric properties. We show that pharmacological perturbations to the lipid membrane composition and to channel activity result in measurable changes to Piezo1 mobility in the "mobile" class of trajectories. The "mobile" class was also found to be subdiffusive across all the tested experimental conditions. Our results demonstrate that membrane composition and channel activity may play a key role in regulating Piezo1 mobility.

4.3 Results

4.3.1 Piezo1-tdTomato puncta exhibit heterogeneous mobility

We imaged with TIRFM endogenously expressed Piezo1-tdTomato in mouse embryonic fibroblast cells (MEFs) harvested from Piezo1-tdTomato reporter mice. Piezo1 channels were visible as distinct puncta as described earlier [35] but with higher fidelity due to improvements in camera technology (Fig. 1A). Visual inspection of videos collected revealed that some puncta were quite mobile while others showed little or no mobility (Fig. 4.1A and Supplemental Video 1 in Supplementary Material). The reduced mobility of some Piezo1 puncta was particularly evident in regions of the cell where Piezo1 puncta appeared to cluster together in structures reminiscent of focal adhesions (Fig. 4.1A, green inset; also compare green and blue insets in Supplemental Video 1), in agreement with reports that Piezo1 is enriched at focal adhesions under certain conditions [176, 46]. We examined the Piezo1 trajectories more closely and found that they could be classified into three categories by visual inspection of their two-dimensional extent: "mobile," where trajectories exhibit a large extent, "trapped," where trajectories are limited to a very small area, and "intermediate," where trajectories are in-between the other two categories (Fig.4.1B).

We were able to consistently classify 1,000 trajectories by visual inspection, but manual classification would be impractical to classify the entire SPT data set of 86,432 trajectories. This motivated the implementation of an algorithmic method for unbiased classification. A number of geometric features have been proposed for automating the classification of trajectories derived from SPT data [162, 53]. We chose a set of six features (net displacement, straightness, radius of gyration, asymmetry, fractal dimension, and kurtosis that are defined in the Supplemental Information). This set of features was able to segregate an initial subset of 1,000-trajectories in a manner consistent with the classification by visual inspection (see Supplementary Fig.4.5).

When computed over the initial 1,000-trajectory data set, the six features exhibited various degrees of pairwise correlation (see Supplementary Fig.4.5), suggesting that additional dimensionality reduction steps were needed. We performed a principal component analysis (PCA) on the six-dimensional feature vectors encoding the 1000-trajectory data set and found that the first three principal components accounted for nearly 90% of the total variance with the first principal component accounting for more than 60% of the total variance (see Supplementary Fig.4.6).

Projecting the six-dimensional feature vectors onto the reduced space of the first three principal components separates the classes assigned by visual inspection, primarily along the first principal component (see Fig.4.2A and Supplementary Fig.4.7, where the 1000-trajectory data are represented as dots). Consistent with this result, three features directly associated to the trajectory spread (net displacement, radius of gyration, and fractal dimension), dominate the first principal component (see Fig.4.2A and Supplementary Fig.4.7, where the individual features are represented as vector arrows). However, the class separation along the first principal component is not without overlaps (see Fig.4.2A). To define boundaries between classes in this three-dimensional subspace, we trained an SVM classifier using the projected features vectors of the visually-classified 1,000-trajectory data set. (Fig.4.2B and Supplementary Fig.4.7).

To validate our classification approach, we performed a control experiment with paraformaldehyde-treated fixed cells, in which Piezo1-tdTomato puncta are rendered immobile. We used the SVM classifier to evaluate the trajectories resulting from the corresponding SPT analysis of these fixed cells. Consistent with the experimental treatment, we found that over 99% of these trajectories were classified as "trapped" with the remainder classified as "intermediate" (see Fig.4.2C and Supplementary Fig.4.8). Furthermore, analysis of Piezo1-tdTomato trajectories obtained from a different cell type, mouse liver sinusoidal endothelial cells (mLSECs), exhibited the three classes seen for MEFs (Fig.4.2C), suggesting that the observed heterogeneity is not limited to Piezo1-tdTomato expressed in MEFs.

4.3.2 Manipulation of the lipid membrane and modulation of channel activity reveals shifts in Piezo1 mobility

Previous studies have shown that changes to membrane composition can affect membrane protein diffusion [102, 13, 1, 122]. In order to explore the relationship between membrane composition and Piezo1 mobility, we used chemical agents to manipulate the membrane in MEFs.

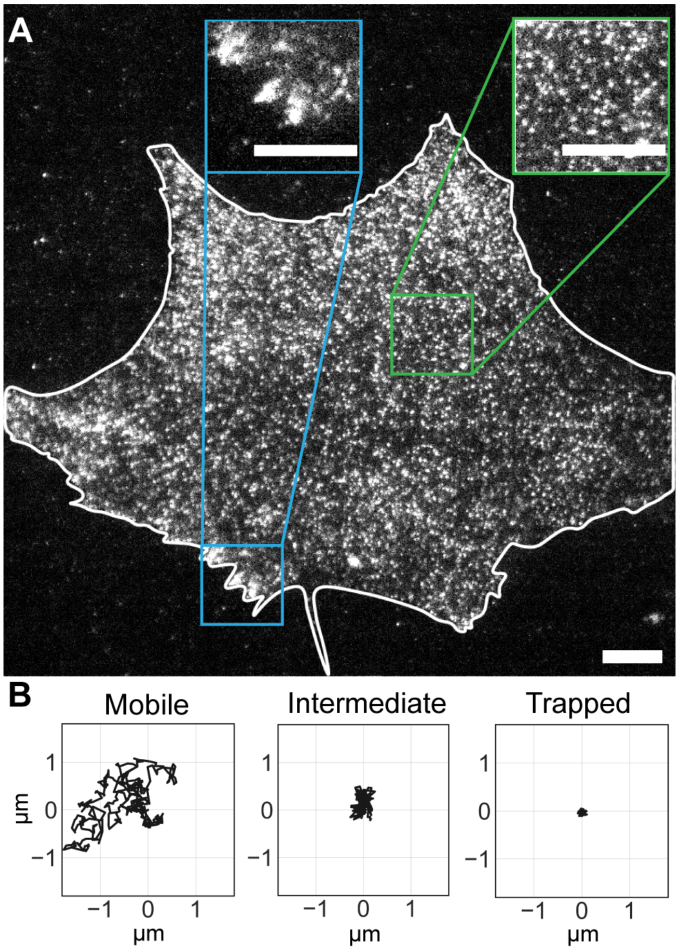

Figure 4.1: TIRF microscopy and single particle tracking reveals heterogeneity in Piezo1-tdTomato mobility. A. Representative fluorescence image of Piezo1-tdTomato puncta in live MEFs harvested from Piezo1-tdTomato reporter mice using TIRFM. The white line denotes the cell boundary. Insets show enlarged regions of interest. B. The trajectories generated from the single particle tracking analysis can be classified by visual inspection into three different classes: those that showed high mobility were nominally identified as "mobile," those exhibiting very small displacements as "trapped," and trajectories with limited spread that were deemed not to belong to either of those categories were labeled "intermediate." See also Supplemental Video 2 in Supplementary Material.
Scale bars = 10 μm.

We treated MEFs with 10 mM MBCD for 15 minutes in order to deplete cholesterol from the membrane and acquired Piezo1-tdTomato TIRFM videos. We then generated and classified Piezo1-tdTomato trajectories from these videos as described above. When we compared the Piezo1-tdTomato trajectories from MBCD-treated cells to those from untreated control cells, MBCD-treated MEFs had a higher proportion of "mobile" trajectories (Supplementary

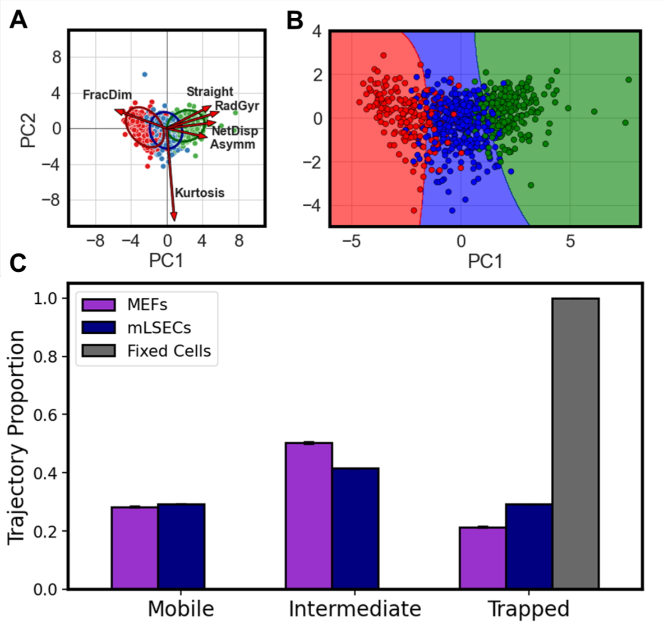

Figure 4.2: Machine-learning methodologies are used to automate the classification of Piezo 1 trajectories. Visual inspection of 1,000 trajectories led us to partition the trajectories into three classes: “mobile”, “intermediate”, and “trapped”. We characterized these 1,000 trajectories using six geometric features, and carried out a principal component analysis to determine a reduced subspace suitable for training a supervised learning algorithm (SVM) for automated sorting of tens of thousands of trajectories into the three classes identified by visual inspection. A. Principal component analysis biplot of a set of Piezo1 trajectories encoded as six-dimensional geometric feature vectors and classified by visual inspection. The 1,000 observations are shown as dots colored by class (“mobile,” green; “intermediate,” blue; “trapped”, red). The three classes are largely separated along the first principal component (PC1) into three overlapping groups, as evidenced by the 95% confidence ellipses for each class. Out of the six geometric features used to describe the trajectories (shown as red arrows), the largest contributions to PC1 are from net displacement, radius of gyration, and fractal dimension, all of which characterize the trajectory spread (see also Supplementary Fig.4.7) B. The set of 1000 trajectories classified by visual inspection was used to train a SVM classifier on the subspace of the feature vectors’ first three principal components. The partition of the PC1-PC2 subspace by the SVM is identified by the background colors in this version of the 1000-trajectory training set scatter plot. C. The automated classification of Piezo1-tdTomato trajectories from mouse embryonic fibroblasts (MEFs, purple) and mouse liver sinusoidal endothelial cells (mLSECs, blue) both show distribution into the three classes “mobile,” “intermediate,” and “trapped”, suggesting that the observed heterogeneity is not restricted to MEF cells. Almost all the trajectories in a SPT data set from MEFs fixed with paraformaldehyde (gray), containing immobile Piezo1-tdTomato, are identified as “trapped”.

Fig.4.9A). To quantify the effect of the MBCD treatment on the mobility of Piezo1 puncta, we use the trajectory’s radius of gyration, R_g, one of the dominant features in the classification

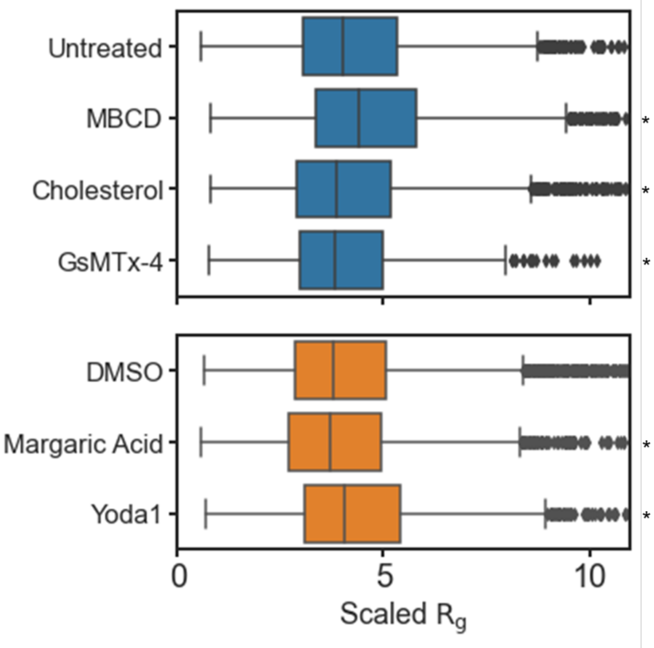

Figure 4.3: "Mobile" Piezo1-tdTomato exhibits changes in trajectory spread consistent with perturbations to membrane composition and channel activity. (*top*) 10 mM methyl-β-cyclodextrin (MBCD), 100 µg/mL cholesterol and 4 µM GsMTx-4 compared to untreated MEFs as control. (*bottom*) 150 µM margaric acid and 4 µM Yoda1 compared to DMSO-treated MEFs as control. All treatments affecting membrane composition or channel activity induce statistical significant changes in the distribution of the scaled R_g in a two-sample Kolmogorov-Smirnov test relative to the corresponding control (* $p < 0.05$).

(Fig.4.2 and Supplementary Fig.4.7A), defined as

$$R_g^2 = \frac{1}{N}\sum_{i=1}^{N}(\vec{x}_i - \langle\vec{x}\rangle)^2 \tag{4.1}$$

where $\vec{x}_i$ is the particle's position at the i-th point of the trajectory, N is the total number of trajectory points, and $\langle\vec{x}\rangle$ is the mean position. To account for variability in step lengths across different trajectories, we scaled R_g by the trajectory's mean step length, $\langle s\rangle = \frac{1}{N-1}\sum_{i=1}^{N-1}|\vec{x}_{i+1} - \vec{x}_i|$, where $|\vec{x}_{i+1} - \vec{x}_i|$ is the Euclidean distance between two consecutive points of the trajectory (see Supplemental Information for details). The resulting scaled R_g ($R_g/\langle s\rangle$) can be used as a consistent measure of trajectory spread.

Compared to the untreated control, application of MBCD increased the scaled R_g of Piezo1 "mobile" trajectories (Fig.4.3), suggesting that cholesterol depletion increases Piezo1 puncta mobility. To determine how the inverse – increasing cholesterol content of the membrane – affects puncta diffusion, we supplemented MEFs with 100 µg/mL cholesterol-MBCD for 1 hour. Utilizing the same methods that we applied to MBCD-treated MEFs, we compared trajectories from untreated control cells to those supplemented with cholesterol-MBCD, and found that cholesterol-MBCD treatment resulted in a lower proportion of mobile trajectories (Supplementary Fig.4.9B). Similarly, the scaled radius of gyration for cholesterol-MBCD-treated "mobile" Piezo1 trajectories decreased compared to untreated control (Fig.4.3), suggesting that the Piezo1 puncta mobility decreases when cholesterol is increased in the membrane.

Cholesterol supplementation stiffens the membrane, and we next investigated how membrane stiffening through other agents affects diffusion. We incubated cells for 24 hours in 150 µM margaric acid, a fatty acid known to stiffen the membrane [124]. We then compared the margaric acid-treated trajectories to the DMSO-treated control trajectories and found that, like cholesterol-MBCD treatment, margaric acid decreased the proportion of "mobile" trajectories (Supplementary Fig.4.9C), albeit to a lesser extent. Similarly, the scaled R_g of margaric acid-treated Piezo1 "mobile" trajectories decreased compared to the DMSO-treated control (Fig.4.3). Interestingly, margaric acid is also known to inhibit Piezo1 activity [124]. To explore whether Piezo1's activation state may also affect its mobility, we next examined the effect of drugs that modulate Piezo1 activity.

GsMTx-4, a spider venom-derived peptide, blocks cation-selective stretch-activated channels and has been shown to inhibit Piezo1 activity [7]. We incubated MEFs in 4 µM GsMTx-4 for 15 min to inhibit Piezo1 channels. We found that the proportion of "mobile" GsMTx-4-treated Piezo1-tdTomato trajectories was lower than the untreated control cells (Supplementary Fig.4.9D). The scaled R_g of GsMTx-4 treated puncta was also decreased compared to that of the untreated control (Fig.4.3). Thus, inhibition of Piezo1 appears to reduce its mobility.

We next examined the effect of Yoda1, a chemical activator of Piezo1, on mobility. We imaged cells treated with 4 µM Yoda1 for 15 minutes, and found that the proportion of "mobile" Piezo1 puncta was greater than those treated with DMSO (Supplementary Fig.4.9E). Yoda1-treated Piezo1 also exhibited higher scaled R_g than the DMSO-treated control (Fig.4.3), further suggesting that active channels are more mobile. Together, these results indicate that the diffusion of the Piezo1-tdTomato mobile class is sensitive to changes in membrane composition as well as to the activation state of the Piezo1 channel.

4.3.3 The mobile class is subdiffusive

The available evidence from fluorescence correlation spectroscopy, fluorescent recovery after photobleaching, and SPT indicates that Brownian motion is not the prevalent diffusive behavior of proteins in the membrane environment (reviewed in [55, 94, 61]). Although the mechanistic details of Piezo1 diffusion in the plasma membrane have yet to be elucidated, the underlying assumption made so far in the literature is that Piezo1 diffusion can be described as Brownian motion [122, 155]. With the tagged particle's trajectory denoted as $\vec{x}(t)$, diffusive behavior can be characterized by the so-called time averaged mean squared displacement (TAMSD) [94]

$$\overline{\delta^2(\Delta)} = \frac{1}{T-\Delta}\int_0^{T-\Delta} (\vec{x}(t+\Delta) - \vec{x}(t))^2 dt \tag{4.2}$$

where T is the trajectory's total length in time and Δ is the lag time.

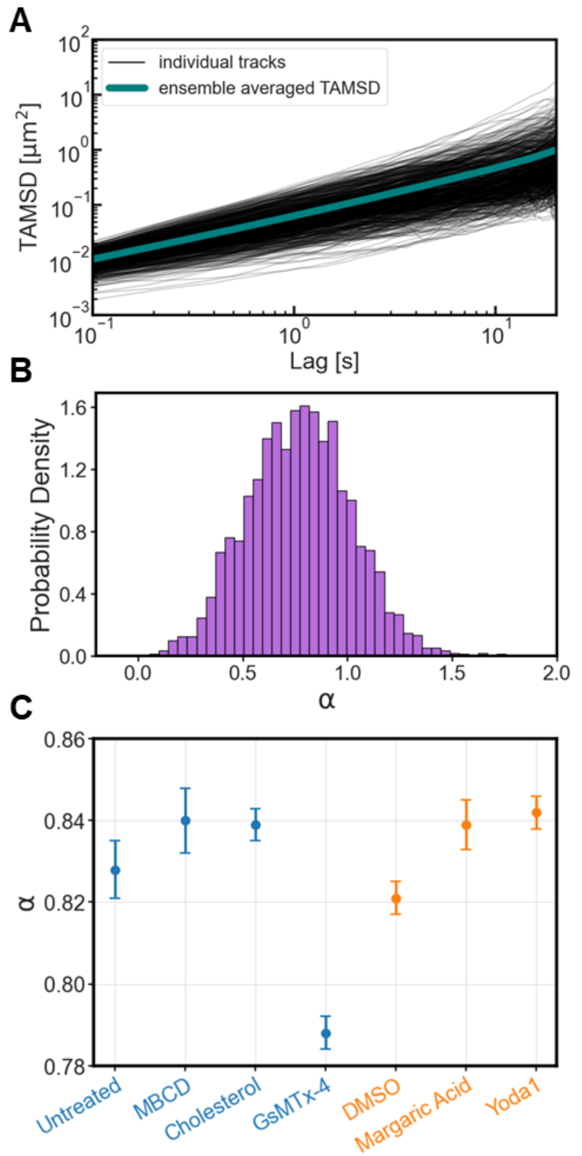

Figure 4.4: “Mobile” Piezo1-tdTomato trajectories are heterogeneous and exhibit anomalous subdiffusion. A. TAMSD as a function of lag time of Piezo1-tdTomato expressed in MEFs (individual trajectories, black; ensemble average, green). Only the untreated condition is shown here; similar results for all tested conditions are shown in Supporting Fig.4.10). B. The corresponding anomalous exponents from individual Piezo1-tdTomato trajectories are broadly distributed. C. The mean estimates of the anomalous exponent distributions indicate subdiffusive behavior across all tested conditions. Line ranges are 95% confidence intervals. The mean estimates from all treatments are different from their corresponding control at this confidence level (blue, treatments using untreated MEFs as control; orange, treatments using DMSO-treated MEFs as control).

Unrestricted Brownian motion is characterized by a linear time dependence of the TAMSD

$$\overline{\delta^2(\Delta)} = K\Delta \tag{4.3}$$

where K is a constant. Deviations from this linear behavior, termed anomalous diffusion, are commonly observed in SPT experiments and modeled using a power-law form

$$\overline{\delta^2(\Delta)} = K_\alpha \Delta^\alpha \tag{4.4}$$

where α, the so-called anomalous exponent, is a positive real constant. A time dependence of the TAMSD that is slower than linear ($0 < \alpha < 1$) is called subdiffusion, while a time dependence that is faster than linear ($\alpha > 1$) is called superdiffusion.

We computed the TAMSD of the individual Piezo1 trajectories in the "mobile" class (see Fig.4.4A). Fitting the individual TAMSDs to a power law (Eq. 4.4) yields a broad distribution of anomalous diffusion exponents, α (Fig.4.4B). Similar results were observed across all the conditions reported in the previous section (Supplementary Fig.4.10). These results are not unexpected. SPT is a time limited recording of a stochastic process. Therefore, estimates of the anomalous diffusion exponent may vary significantly among trajectories collected from the same experiment. A common practice is to perform an additional average of the TAMSD over an ensemble of N collected trajectories,

$$\langle \overline{\delta^2(\Delta)} \rangle = \sum_{i=1}^{N} \overline{\delta_i^2(\Delta)}. \tag{4.5}$$

The resulting ensemble-averaged TAMSD (EA-TAMSD) (shown as green traces in Fig.4.4A and Supplementary Fig.4.10) is sufficient to eliminate the variability associated with time limited measurements and random errors, but it fails to account for measurement noise as well as the intrinsic variability in the particles' diffusing behavior [73, 89]. Accurate estimates of the mean and width of the distribution of anomalous exponents for the ensemble of particles can be obtained from the EA-TAMSD after correcting for these systematic errors as described in [73]. The results for the Piezo1 “mobile” class indicate a consistent subdiffusive behavior across all the experimental conditions (see Fig.4.4C).

In contrast to the trajectory spread analysis reported in (Fig.4.3), where changes to the scaled R_g distribution can be directly associated to changes in Piezo1 mobility upon membrane composition and channel activation state perturbations, an interpretation of the small but statistically significant changes to the anomalous exponent would require a detailed modeling of the diffusion mechanisms, which is beyond the scope of the present TAMSD analysis. Nevertheless, the persistence of alpha well below unity indicates that anomalous diffusion is a consistent property of Piezo1 mobility under a variety of conditions.

4.4 Discussion & Conclusions

Here, we follow up on our previous finding that Piezo1 channels are mobile [35] by performing single-particle tracking (SPT) of endogenously expressed Piezo1-tdTomato channel puncta. We observed that Piezo1 exhibits multiple modes of diffusion in two different cell types, MEFs and mLSECs. Through visual observation of the trajectories, we classified the trajectories into three classes based on their spatial extent - “mobile”, “intermediate” and “trapped.” We then implemented a supervised machine approach algorithm to automate this classification for thousands of trajectories, and examined the effect of specific pharmacological perturbations on Piezo1 mobility.

Our findings are consistent with a large body of experimental evidence indicating that the lateral motion of membrane proteins in the complex environment of the plasma membrane is dependent on the local structure and regulatory signals encountered by each individual protein or cluster of proteins [62, 129, 61]. This behavior is put in full display by the spatiotemporal resolution of SPT of tagged proteins [129, 134]. Trajectory classification is thus a prerequisite for the interpretation of the Piezo1 SPT data.

Almost all of the schemes proposed in the literature for the classification of SPT trajectories of membrane proteins are based on descriptions of the motion itself or on more detailed diffusion models [136, 114, 96, 52, 43, 75, 166, 44, 64, 99]. We have taken an approach to trajectory classification that relies only on geometrical aspects of the trajectories without input from diffusion models at any level of the classification process. A similar approach was proposed recently by Pinholt et al. and shown to effectively identify distinct diffusion modes in a wide variety of systems [111]. In contrast to Pinholt et al., our set of descriptive features for classification does not include quantities associated with the MSD analysis of the trajectory. By separating the trajectory classification from the description of the underlying diffusive process, we can in the future interrogate each class separately using experimental methods to probe specific connections between channel activity and mobility and use diffusion models in the interpretation of those results. Here, we have begun to address the first part of this program, by developing a reliable automated classification scheme.

According to our classification scheme, a class of trajectories nominally identified as “mobile” exhibit high mobility in the plasma membrane compared to the other two classes, “trapped” or “intermediate.” A recent pre-print by Vaisey et al. reporting SPT on endogenous Piezo1 in red blood cells also observed heterogeneity in Piezo1 trajectories [155]. Our detailed analysis of this class suggests that Piezo1 mobility is sensitive to changes in membrane composition and that activity may modulate the channel’s diffusion. Supplementation of the membrane with cholesterol or margaric acid decreases Piezo1 mobility, while cholesterol depletion via MBCD increases mobility. These results are consistent with findings from several ion channel diffusion studies. Removal of membrane cholesterol reduces the population of confined Orai1, an ion channel that causes extracellular calcium influx upon internal calcium store depletion, and causes the channels to move in a linear pattern [13]. Similarly, both serotonin transporters [8] and dopamine transporters [2] increase in lateral mobility following MBCD treatment. Ridone *et al.* also found that cholesterol depletion increased the diffusion of overexpressed Piezo1 in HEK293T cells [122].

Our results demonstrate that drug-induced changes to the channel state affect channel mobility in MEFs. Margaric acid has been shown to stiffen the plasma membrane and inhibit Piezo1 activation. When we treated cells with margaric acid, Piezo1-tdTomato trajectories were less mobile than DMSO-treated control trajectories. Romero et al. had previously proposed that margaric acid's inhibitory effect on Piezo1 could be a result of the drug's role in membrane remodeling [124]. Another channel inhibitor that partitions into the membrane, the amphipathic tarantula venom peptide, GsMTx-4 [7], has been posited to disrupt transfer of force to the channel in the plasma membrane, thereby inhibit Piezo1 activation [42]. While GsMTx-4 treatment results in a decrease in mobility relative to the untreated control, suggesting that closed channels may be less mobile, the observed shifts in mobility could also be a result of potential shifts in local membrane tension rather than channel conformational changes. Conversely, we have shown that Yoda1, a Piezo1 agonist [144], increases mobility. However, it is important to note that while Yoda1 activates the Piezo1 channel and results in greater mobility, chemically-driven activation by Yoda1 may not necessarily be analogous to the behavior of channels activated by an increase in local membrane tension. Yoda1 has been shown to stabilize the open state [144, 169], and it has been proposed that Yoda1 acts as a molecular wedge when bound to Piezo1, affecting both the channel's mechanosensitivity and flexibility of the blades [14]. It is unknown whether this steric modification may be enough to affect channel diffusion. Future studies simultaneously monitoring the activity and mobility of Piezo1 are needed.

Our MSD analysis of the "mobile" class of Piezo1 revealed a consistent subdiffusive behavior across all experimental conditions, suggesting that this may be a fundamental characteristic of Piezo1 mobility in the plasma membrane. Although the underlying physical mechanisms may vary, a wealth of experimental evidence suggests that subdiffusion is a ubiquitous mode of motion for submicron particles in the cell membrane [55, 94, 52, 43, 97, 61]. Subdiffusion may be the result of the lateral heterogeneity of the membrane environment sampled by the channel or it may reflect transient associations with other membrane components [129, 150, 61]. Specific hypotheses in the case of Piezo1 will require detailed modeling of the diffusion process, which is the subject of a future study.

Piezo1 mobility has several important implications. Channel mobility may allow fewer channels to explore a larger domain of the cell to efficiently transduce mechanical forces. Mobility may also function as a mechanism for channels to dynamically adjust the cellular response to mechanical forces. Mechanical forces can act upon a cell at any time, from anywhere, and Piezo1's mobility in conjunction with its activation state may aid the cell in adjusting to these responses. Additionally, open and closed channels may exhibit different mobilities, providing specific mechanisms through which the cell can modulate mechanotransduction. For instance, closed channels may be more mobile than open channels. This would allow closed channels to explore the cell in search of mechanical cues, and for open channels to linger at cellular regions experiencing mechanical stimuli. Conversely, open channels may be more mobile than closed channels. In this case, when the channel experiences mechanical forces, open-mobile channels may move away from persistent mechanical stimuli, thereby closing the channel and terminating the mechanotransduction. Our findings set the stage for future work examining Piezo1 mobility in the context of channel activity.

4.5 Future Work

Our current work explores Piezo1 by perturbing the actin cytoskeleton or by modulating the membrane. As a mechanically-activated ion channel, the most interesting aspects of Piezo1 are linked to its activation/deactivation. To this end, we have prepared future data from experiments where the tdTomato-tagged, endogenously expressed Piezo1 is treated with an activator drug, Yoda1, and a deactivator, the spider toxin GsMTx4. These drugs will provide relevant insights into changes in diffusion profile related to activity.

The Pathak lab has also been experimenting with a new, more resilient tag, HaloTag. This fluorotag would greatly enhance the throughput of our experiments by extending collection time by 100% without sacrificing the fluorescent tag to bleaching events. The realization of such data would allow us to perform statistical analyses with greater confidence due to the increased robustness of the data. It is also possible that longer collection times may reveal hitherto unknown aspects of Piezo1 diffusion or mobility.

Finally, it would be extremely useful to apply a physics based analysis to the diffusive behaviors under investigation via Piezo1. We have a great pipeline that extends from experiment, to data procurement, to machine learning classification. It would be quite an achievement to extend this pipeline to include an analytical component that could use mathematical models to identify distinct types of diffusion or at least hallmarks/fingerprinting evidence of a specific diffusive process.

4.6 Materials and Methods

4.6.1 Mouse Embryonic Fibroblast (MEF) Harvesting and Culture

MEF cells were isolated from a reporter mouse (JAX stock 029214) with a tdTomato knock-in at the C-terminus of the endogenous Piezo1 channel [116]. Mice were considered embryonic day 0.5 upon vaginal plugging. Fibroblast cells were harvested from embryos by separating the head, limbs, and tail from the embryo at embryonic day 12.5 in 33 mM D-(+)-glucose (Sigma-Aldrich, G-6152) and 1% Penicillin-Streptomycin (10,000 U/mL; Gibco, 15140122) in Dulbecco's Phosphate-Buffered Saline (Gibco, 14-190-250). The remaining tissue was spun at 260g for 5 min, and the supernatant was aspirated. These cells were cultured in DMEM (ThermoFisher Scientific, 11960-051) with 15% fetal bovine serum (Omega Scientific, FB-12), 1x GlutaMax (ThermoFisher Scientific, 35050-061), 1 mM sodium pyruvate (ThermoFisher Scientific, 11360-070), and 1x non-essential amino acid solution (ThermoFisher Scientific, 11140-050) in a sterile environment at 37°C with 5% CO_2. Cells were plated in a T-25 cell culture flask (Eppendorf, 0030710126) coated with 0.1% gelatin solution (Fisher Scientific, ES-006-B). Media was changed 1 hour after plating. MEF cells containing Piezo1-tdTomato were passaged using TrypLE Express (ThermoFisher, 12604013) to dissociate the cells and were spun at 260g for 5 min. Cells were then counted using a hemocytometer and 7,500-10,000 cells between the passages of 3-7 were plated on the 14mm glass region of #1.5 glass-bottom dishes (Mat-Tek Corporation) coated with 10 µg/mL fibronectin (Fisher Scientific, CB-40008A). Media was changed following 2h and every 48h until imaging experiments. Cells were maintained in a 5% CO_2 incubator at 37$^{\underline{o}}$C for at least 72h prior to imaging.

4.6.2 Mouse Liver Sinusoidal Endothelial (mLSEC) Isolation and Culture

mLSECs were isolated using an immunomagnetic separation technique. A mouse liver was thoroughly minced using scalpel blades and resuspended in a dissociation solution containing 9 mL 0.1% collagenase II, 1 mL 2.5 U ml-1 dispase, 1 µM $CaCl_2$ and 1 µM $MgCl_2$ in Hanks Buffer solution. The tissue-dissociation mix was incubated at 37$^{\underline{o}}$C for 50 mins in a tube rotator to provide continuous agitation. Following this enzymatic digestion, the mix was passed through 70 and 40 µm cell strainers to remove undigested tissue. Cells were washed twice in PEB buffer containing phosphate-buffered saline solution (PBS), EDTA 2mM and

0.5% BSA, pH 7.2. The washed pellets were resuspended in 1 mL PEB buffer and 30 µL CD146 microbeads (Miltenyi Biotech) at 4ºC for 15 min under continuous agitation. CD146 is a membrane protein marker for endothelial cells and is highly expressed in mLSECs. Following incubation, the solution was passed through an LS column (Miltenyi Biotech) primed with PEB buffer. The column was washed 3 times with 5 mL PEB buffer and the CD146 negative eluate was removed. CD146 positive cells were retained in the column and flushed with 5 mL warmed EGM-2 growth medium supplemented with EGM-2 bullet kit (Lonza) into a separate tube. Cells were spun at 300g for 5 min, diluted in 1 mL EGM-2 media and counted using a hemocytometer. 30,000-40,000 cells were plated on the 14 mm glass region of #1.5 glass-bottom dishes (Mat-Tek Corporation) coated with 10 µg/mL fibronectin (Fisher Scientific, CB-40008A). Media was changed after 2h and every 48h until imaging experiments. Cells were grown in a 5% CO_2 incubator at 37ºC for at least 72h prior to imaging.

4.6.3 Imaging Piezo1-tdTomato

Mobility of native Piezo1-tdTomato channels was imaged using Total Internal Reflection Fluorescence (TIRF) microscopy at 37°C. Piezo1-tdTomato MEFs and mLSECs were washed with phenol red-free DMEM/F12 (Invitrogen, 25116001) thrice and incubated in imaging solution, composed of 148 mM NaCl, 3 mM $CaCl_2$, 1 mM KCl, 2 mM $MgCl_2$, 8 mM Glucose, 10 mM HEPES, pH 7.30, and 316 mOsm/L osmolarity for 5 min. An Olympus IX83 microscope fitted with a 4-line cellTIRF illuminator, an environmental control enclosure and stage top incubator (Tokai Hit), and a PLAPO 60x oil immersion objective NA 1.45 was used to image cells. A programmable motorized stage (ASI) was used to identify samples throughout imaging. Images were acquired using the open source software µ-Manager [34]. Cells were illuminated with a 561 nm laser and images were acquired using a Hamamatsu

Flash 4.0 v2+ scientific CMOS camera at a frame rate of 10 frames/second with a 100 ms exposure time.

Piezo1-tdTomato cells (MEFs) were fixed using a 4% paraformaldehyde (Electron Microscopy Sciences, 15710), 1x PBS, 5 mM $MgCl_2$, 10 mM EGTA, 40 mg/mL sucrose buffer for 10 min at room temperature. The cells were washed thrice with PBS for 5 minutes.

4.6.4 Drug Treatment

Methyl-β-cyclodextrin-treated cells were incubated in 10 mM methyl-β-cyclodextrin (Sigma-Aldrich, C4555-5G) for 15 min before imaging. Cholesterol-MBCD-treated cells were incubated in 100 µg/mL cholesterol-water soluble, containing methyl-β-cyclodextrin (Sigma-Aldrich, C4951-30mg) and were incubated for 1 hour. Cells treated with 150 µM margaric acid (NuChek N-17-A) were incubated overnight at 37°C for 24h. Cells treated with 4 µM Yoda1 (Tocris 558610) or 4 µM GsMTx-4 (Tocris 4912) were incubated for 15 min. Margaric acid and Yoda1 were dissolved in Dimethyl sulfoxide (DMSO, Sigma Aldrich 276855-100ML). As such, DMSO was used as a control for margaric acid and Yoda1. All cells were imaged for 30 min post-treatment as described above.

4.6.5 Piezo1-tdTomato Trajectory Generation

Single particle tracking of Piezo1-tdTomato puncta was done using the open-source image processing and analysis program Flika [36]. A difference of Gaussians algorithm was used as a spatial bandpass filter on the image stacks to detect the Piezo1-tdTomato punctae. The resulting enhanced stack was then thresholded using a manually selected threshold value to generate a binary image stack. Spatially-continuous pixels above this threshold were considered a single particle. A two-dimensional Gaussian function was used to determine the centroid of each particle to subpixel precision. Particles within three pixels of consecutive frames were assumed to represent the same Piezo1-tdTomato puncta. These particles were then linked to generate trajectories. Skipped frames were handled by inserting a placeholder value (numpy.nan) for missing coordinates [35, 49]. A conversion factor equivalent to the length of a single pixel, 0.1092 µm, was used to transform two-dimensional coordinates in pixel units to microns. We limited our analysis to trajectories that were at least 20 seconds in length, which at a frame rate of 100 milliseconds, guaranteed a minimum of 200 positions per trajectory.

4.6.6 Trajectory Feature Selection and Analysis

A precursory scan of plotted trajectories from untreated MEFs revealed three visually distinct trajectory types: trajectories with a large extent ("mobile"), those with a very tight puncta ("trapped"), and trajectories that appeared to be between these two categories ("intermediate"). The large size of the trajectory data sets prompted us to develop a workflow for automated classification using supervised learning [63]. The task of supervised learning is finding a model that maps input variables to an output variable based on paired input-output observations. In the context of classification, the output variable is a discrete set of classes, the input variables are termed *features* and the input-output pairs are termed the *training set* [63].

In the context of classification of SPT trajectories using supervised learning methods, a trajectory feature is generated by mapping the trajectory's spatial coordinates to a single scalar that is invariant to rigid-body motions of the entire trajectory [53]. Among the trajectory features reported in the literature [53, 162], we only considered those that described geometric aspects of the trajectories.

To further examine each one of the candidate features, we classified a set of 1,000 trajectories of Piezo1-tdTomato untreated MEFs by visual inspection (as described in the next section), we then mapped each trajectory onto the feature under examination, and checked whether the corresponding feature distribution was partitioned by our classification scheme (see Supplementary Fig.4.5). Following this approach, we selected six features: net displacement, straightness, radius of gyration, asymmetry, kurtosis, and fractal dimension, which are described in detail in the Supplemental Information.

Each one of the six selected features computed over the 1,000-trajectory data set was normalized using a Box-Cox transformation [15]. A principal component analysis was performed on the transformed data set of six-dimensional vectors. Nearly 90% of the variance was explained by the first three principal components. The projection of the transformed data set on this reduced three-dimensional principal component subspace was used as the training set for the classification.

All feature calculations and analyses were carried out with in-house Python scripts using the Numpy [49], SciPy [161], and Pandas [167] libraries. Data visualization was performed with Matplotlib [60] and seaborn [164].

4.6.7 Trajectory Labeling

The 1,000 trajectories randomly sampled from the 11,794 trajectories of Piezo1-tdTomato untreated MEFs indicated above were visually classified (labeled) as “mobile”, “trapped”, or “intermediate” by three different researchers. This was a blind process where each researcher independently performed their own labeling, without knowledge or influence from the other parties. Through this process, each of the 1,000 trajectories was assigned three possible labels, from which the majority label was chosen as the final class for each trajectory. This three-party labeling process was an effort to reduce bias in the initial subjective classification.

4.6.8 Support Vector Machine Training

A support vector machine (SVM) is a supervised learning algorithm designed to maximize the margin of separation between sets of features with different labels by identifying dividing hyperplanes. The features in this context are nonlinear transformations of the original observations performed with one of several so-called kernel functions. Kernel functions have adjustable parameters that are usually chosen by performing a search over the parameter space, performing a cross-validation with the training set on each specific choice of parameters, and selecting the one with the highest accuracy. Here, the Radial Basis Function (RBF, a Gaussian function) was chosen as kernel function. An SVM with an RBF kernel has two tunable parameters, a regularization parameter, C, and a curvature or shape parameter, γ, which were selected based on a six-fold cross-validation carried out via grid search of the parameter space. Briefly, the training set was split 80:20 for training and testing/validation. For each point in the grid, the SVM was trained on the same 80% of training data, and then evaluated against the remaining 20% via cross-validation. For cross-validation, the 20% hold out set was randomly split into 6 subsets and then stratified to balance class representations in each set. The SVM performance was evaluated and averaged for all 6 subsets and compared across all grid search configurations with the best parameters determined by the highest F1-score averaged over the three classes. The F1-score is a measure of a binary classifier's accuracy, defined as the harmonic mean of the classifier's *precision* and *recall*. Precision is the total number of correctly predicted observations divided by the total number of predictions. Recall is the total number of correctly predicted observations divided by the total number of observations. The final values of $C = 4\ 0.0$ and $\gamma = 0.03$ were chosen, corresponding to an average F1-score of 87% (Supplementary Fig.4.11). The was SVM implemented with in-house Python scripts, using the Numpy [49], Pandas [167] and Scikit-Learn [108] libraries. The training set split was performed using the test-train-split module in the Scikit-learn library. Confusion matrices for the test and train portions, along with table of accuracy metrics are available in the Supplementary Information.

4.7 Supplementary Information

4.7.1 Mapping SPT trajectories to geometric features

In the context of SPT, the trajectory of a tagged particle is represented by an ordered sequence of N two-dimentional position vectors sampled at a constant time interval, Δt,

$$\vec{x}(t) = \{\vec{x}_1, \vec{x}_2 \ldots, \vec{x}_N\} \tag{4.1}$$

where $\vec{x}_i = (x_i, y_i) \in R^2$ is the position vector at time $t = i\Delta t$, $i = 1 \ldots N$.

A trajectory *step* is the difference between consecutive position vectors $\vec{s}_i = \vec{x}_{i+1} - \vec{x}_i$. Therefore, a trajectory can also be described by the sequence of the $N-1$ corresponding steps,

$$\vec{x}(t) \equiv \{\vec{s}_1, \vec{s}_2 \ldots, \vec{s}_{N-1}\} \tag{4.2}$$

We mapped each SPT trajectory to a six-dimensional *feature* vector: $(\Delta x, S, R_g, a, k, D_f)$, whose components (net displacement, straightness, radius of gyration, asymmetry, kurtosis, and fractal dimension) describe different geometric aspects of the trajectory.[53, 162]

Net Displacement

Net displacement, Δx, is the Euclidean distance of the trajectory final position to the initial position,

$$\Delta x = \sqrt{(x_N - x_1)^2 + (y_N - y_1)^2} \tag{4.3}$$

Straightness

Straightness, S, is a measure of the average direction change between consecutive steps, defined as [53]

$$S = \frac{1}{N-2} \sum_{i=1}^{N-2} \frac{\vec{s}_i \cdot \vec{s}_{i+1}}{|\vec{s}_i||\vec{s}_{i+1}|} \tag{4.4}$$

Radius of Gyration and Asymmetry

The trajectory's gyration tensor is the covariance matrix [128],

$$\mathrm{T} = \begin{pmatrix} \langle x^2 \rangle - \langle x \rangle^2 & \langle xy \rangle - \langle x \rangle \langle y \rangle \\ \langle xy \rangle - \langle x \rangle \langle y \rangle & \langle y^2 \rangle - \langle y \rangle^2 \end{pmatrix} \tag{4.5}$$

where $\langle \ldots \rangle$ denotes the mean of its argument (e.g. $\langle x \rangle = \sum_{i=1}^{N} x_i$). The gyration tensor is a symmetric 2-by-2 matrix,

$$\begin{pmatrix} T_{xx} & T_{xy} \\ T_{xy} & T_{yy} \end{pmatrix}$$

with eigenvalues

$$\lambda_{1,2} = \frac{(T_{xx} + T_{yy}) \pm \sqrt{(T_{xx} - T_{yy})^2 - 4T_{xy}^2}}{2} \tag{4.6}$$

The radius of gyration, R_g, is a measure of the overall extent of the trajectory, defined by

$$R_g^2 = \lambda_1 + \lambda_2 \tag{4.7}$$

Substituting (4.6) in (4.7) leads to

$$R_g^2 = (\langle x^2\rangle - \langle x\rangle^2) + (\langle y^2\rangle - \langle y\rangle^2) \tag{4.8}$$

which is equivalent to equation (4.1) in the main text.

The asymmetry, a, measures the elongation of the trajectory. We use the definition proposed by Helmuth et al. [53]

$$a = -\log\left(1 - \frac{(\lambda_1 - \lambda_2)^2}{2(\lambda_1 + \lambda_2)^2}\right) \tag{4.9}$$

Kurtosis

Kurtosis, k, is the standardized central fourth moment of a probability distribution. It measures whether a distribution is heavy-tailed in reference to a normal distribution. Here, we use it as a descriptor for the distribution of trajectory steps projected onto the gyration tensor's major principal axis. The major principal axis is the direction of the eigenvector $\vec{v}$ corresponding to the largest eigenvalue. In this case, $\mathrm{T}\vec{v} = \lambda_1\vec{v}$. The kurtosis feature is then given by:

$$k = (N-1)\frac{\displaystyle\sum_{i=1}^{N-1}(s_i - \langle s_i\rangle)^4}{\left(\displaystyle\sum_{i=1}^{N-1}(s_i - \langle s_i\rangle)^2\right)^2} \tag{4.10}$$

where $s_i = \vec{s}_i \cdot \vec{v}$ and $\langle s_i\rangle = \frac{1}{N-1}\sum_{i=1}^{N-1} s_i$.

4.7.2 Fractal Dimension

The trajectory's fractal dimension is defined as [72]

$$D_f = \frac{\log(N-1)}{\log(N-1) + \log(\frac{d}{L})} \tag{4.11}$$

where d denotes the largest distance between any two trajectory positions, and $L = \sum_{i=1}^{N} s_i$ denotes the total length of the trajectory. It is a measure of the degree to which the trajectory is space-filling. A straight line has $D_f = 1$; any other planar curve will have $D_f > 1$. A two-dimensional random walk has $D_f = 2$. A trajectory constrained to a limited area may have multiple overlaps and therefore will have $D_f > 2$.

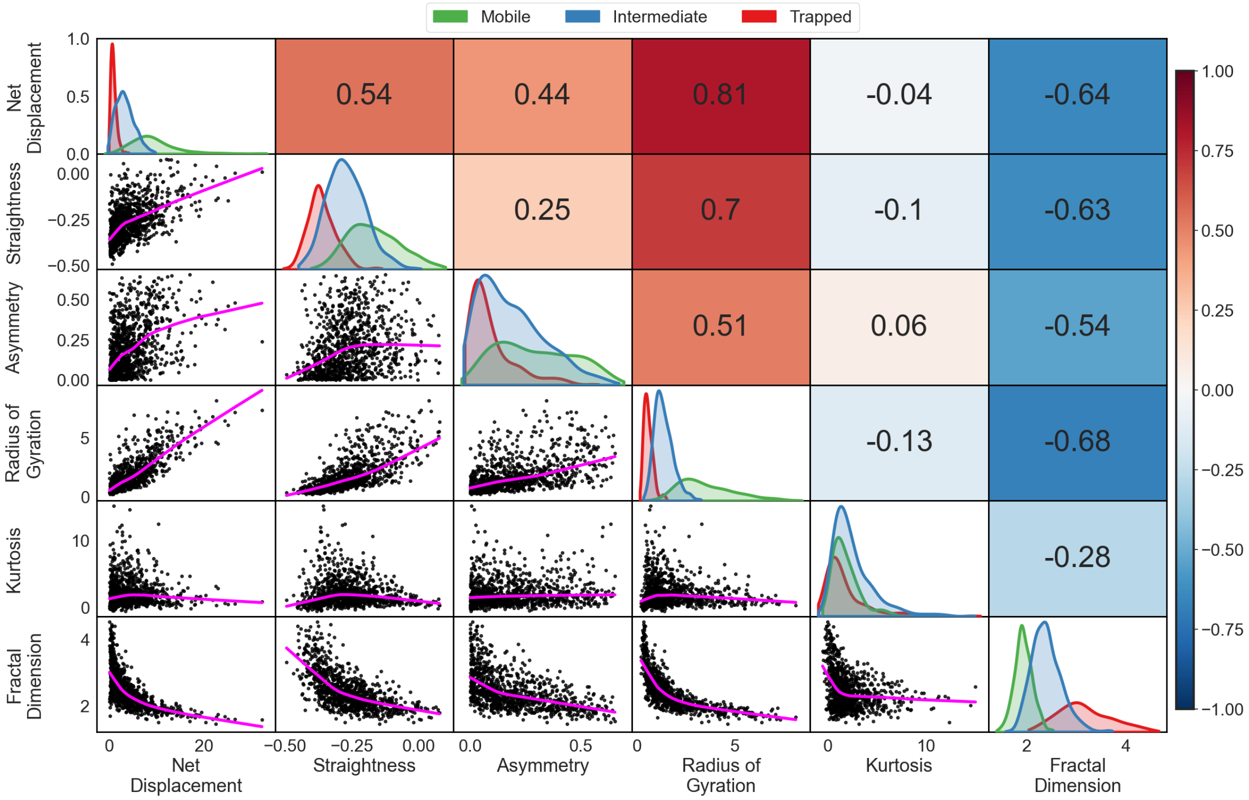

Supplementary Figure 4.5: Correlation matrix plot of geometric features used for automated trajectory classification calculated from a 1000-trajectory data set classified by visual inspection. The diagonal elements show kernel density estimates of of each feature distribution separated by their labeled class (“mobile,” green; “intermediate,” blue; “trapped,” red). The relationships between pairs of features are shown as scatter plots below the diagonal. A locally weighted scatterplot smoothing trend line is shown in magenta. The corresponding Pearson correlation coefficients are shown above the diagonal colored according to a BWR color scale.

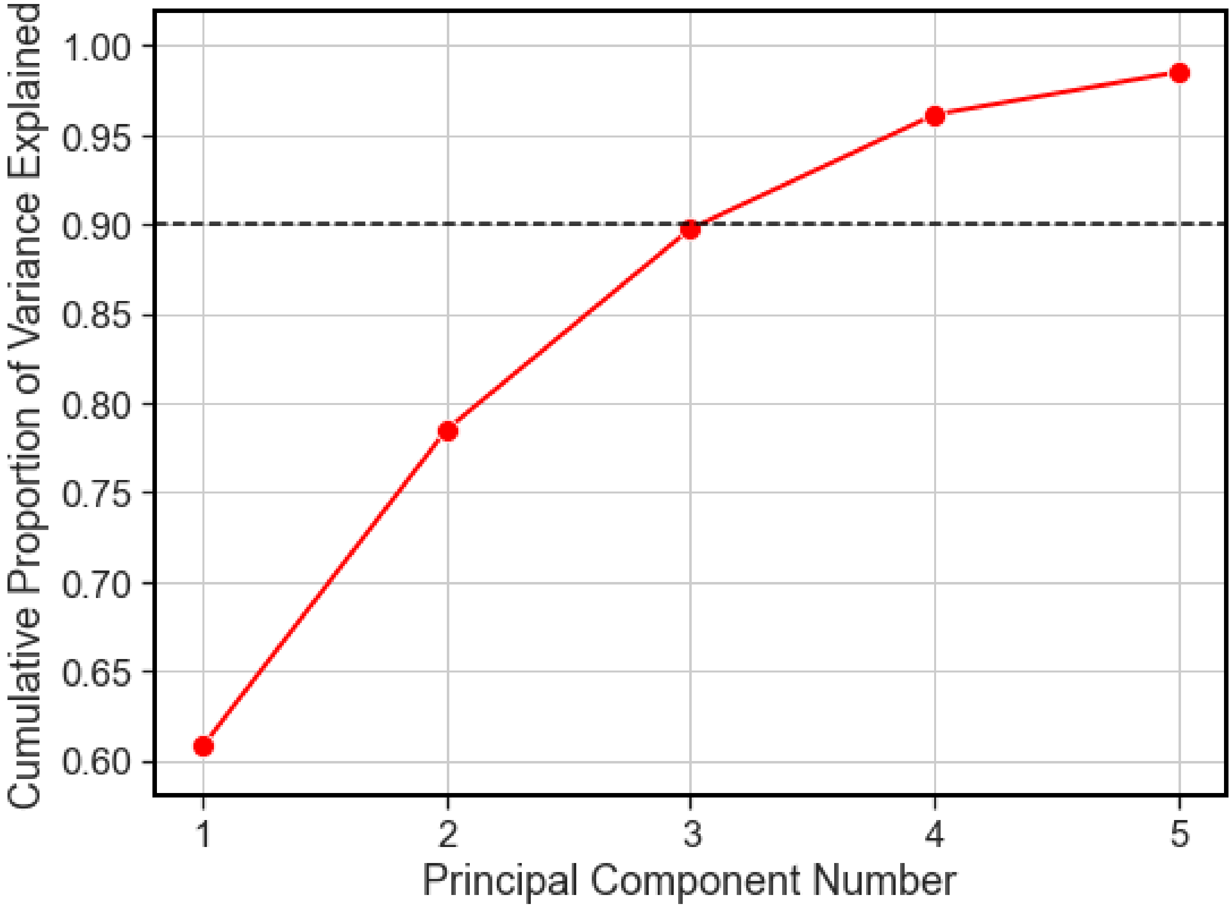

Supplementary Figure 4.6: Cummulative proportion of variance explained by the principal components of the six-dimensional geometric feature vectors generated from the 1000-trajectory data set classified by visual inspection. The horizontal dashed line indicates that 90% of the variance six-dimensional data set is explained by the first three principal components.

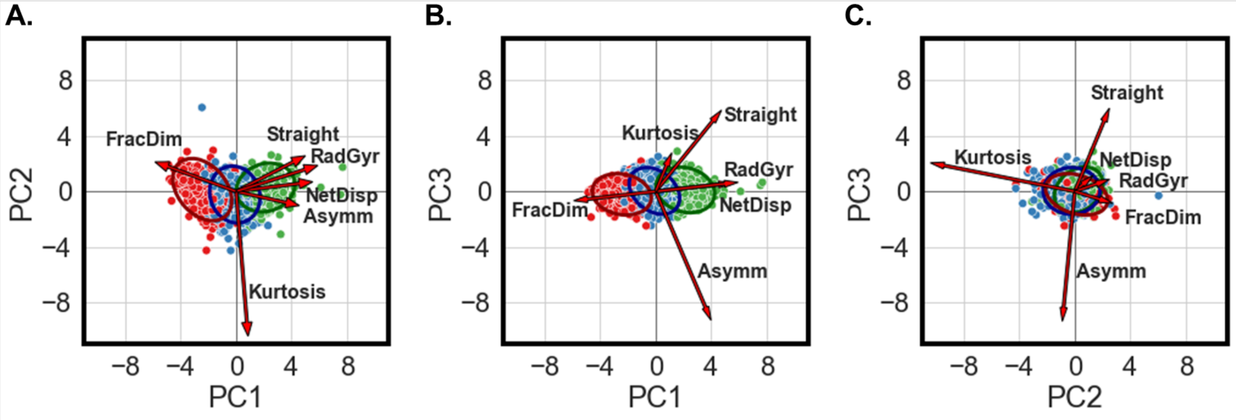

Supplementary Figure 4.7: Principal component analysis biplots of the six-dimensional geometric feature vectors generated from the 1000-trajectory data set classified by visual inspection. The projections of the 1000 observations onto each subspace are shown as dots colored by class (“mobile,” green; “intermediate,” blue; “trapped”, red). The three classes are largely separated along the first principal component (PC1) into three overlapping groups, as evidenced by the 95% confidence ellipses for each class with limited contributions from PC2 and PC3. The red arrows show the projection of the original features onto each subspace (scaled up by a factor of 10). The largest contributions to PC1 are from net displacement, radius of gyration, and fractal dimension, all of which characterize the trajectory spread. Limited separation between classes in the PC2-PC3 plane (panel C) indicates that including additional principal components would not improve trajectory segregation, justifying the choice of a three-dimensional principal components subspace for training. Panel A is also shown in Figure 4.2A

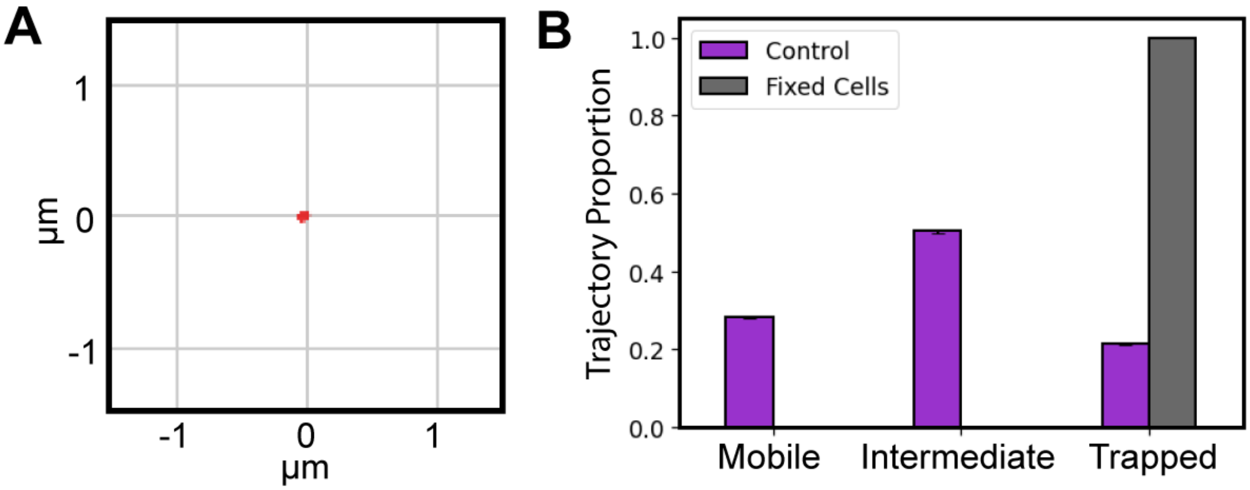

Supplementary Figure 4.8: Piezo1-tdTomato in fixed MEFs are classified as “trapped” by the SVM. A. Representative Piezo1-tdTomato trajectory (red) from a fixed Piezo1-tdTomato MEF showing a highly limited spatial extent. B. Almost all the trajectories from a fixed Piezo1-tdTomato MEF data set are identified as “trapped” by the SVM. Also shown in Fig.4.2C

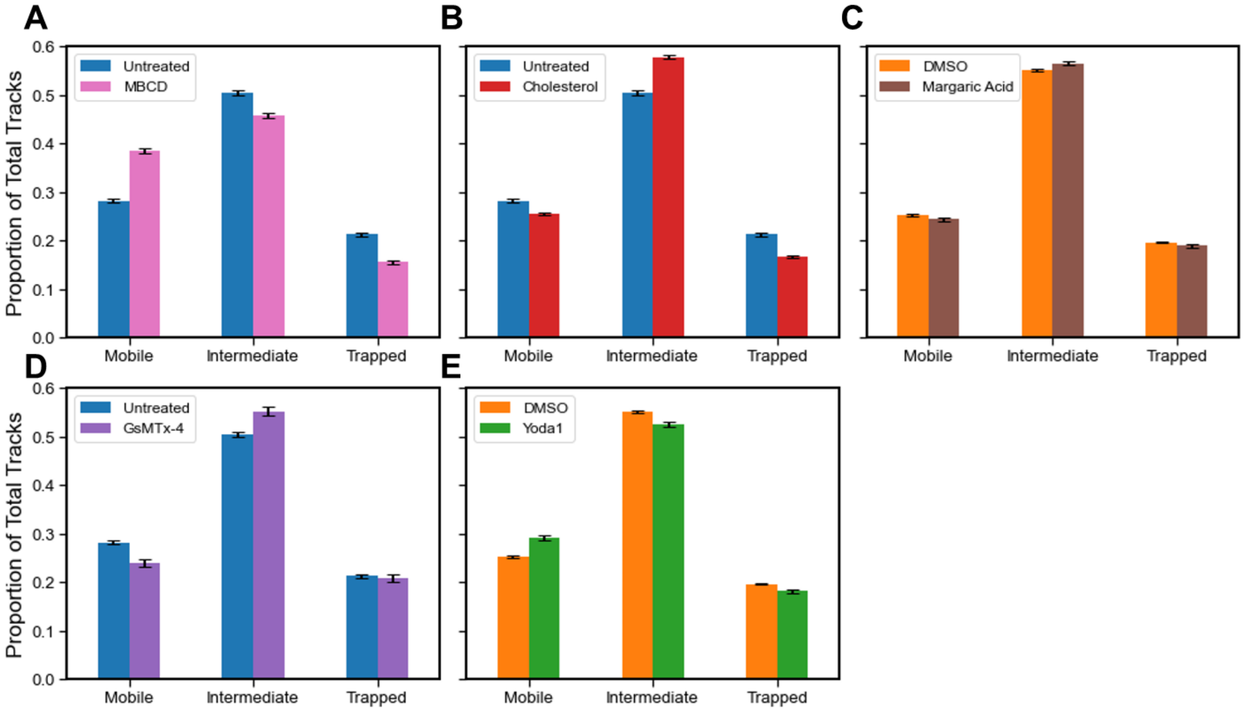

Supplementary Figure 4.9: Trajectory proportions resulting from the SVM classification of Piezo1-tdTomato trajectories under various conditions. A. MBCD treatment (pink) results in an increase in the “mobile” proportion of trajectories relative to the untreated control (blue). B. Cholesterol-MBCD treatment (red) results in a decrease in the “mobile” proportion of trajectories relative to the untreated control (blue). C. Margaric acid treatment (brown) results in a decrease in the “mobile” proportion of trajectories relative to the DMSO control (orange). D. GsMTx-4 treatment (purple) results in a decrease in the “mobile” proportion of trajectories relative to the untreated control (blue). E. Yoda1 treatment (green) results in an increase in the “mobile” trajectories relative to the DMSO-treated control (orange). The SVM was trained as three separate binary classifiers. Thus, we interpret the bar heights within one plot as the sample proportions for each class. The error bars are the corresponding standard errors.

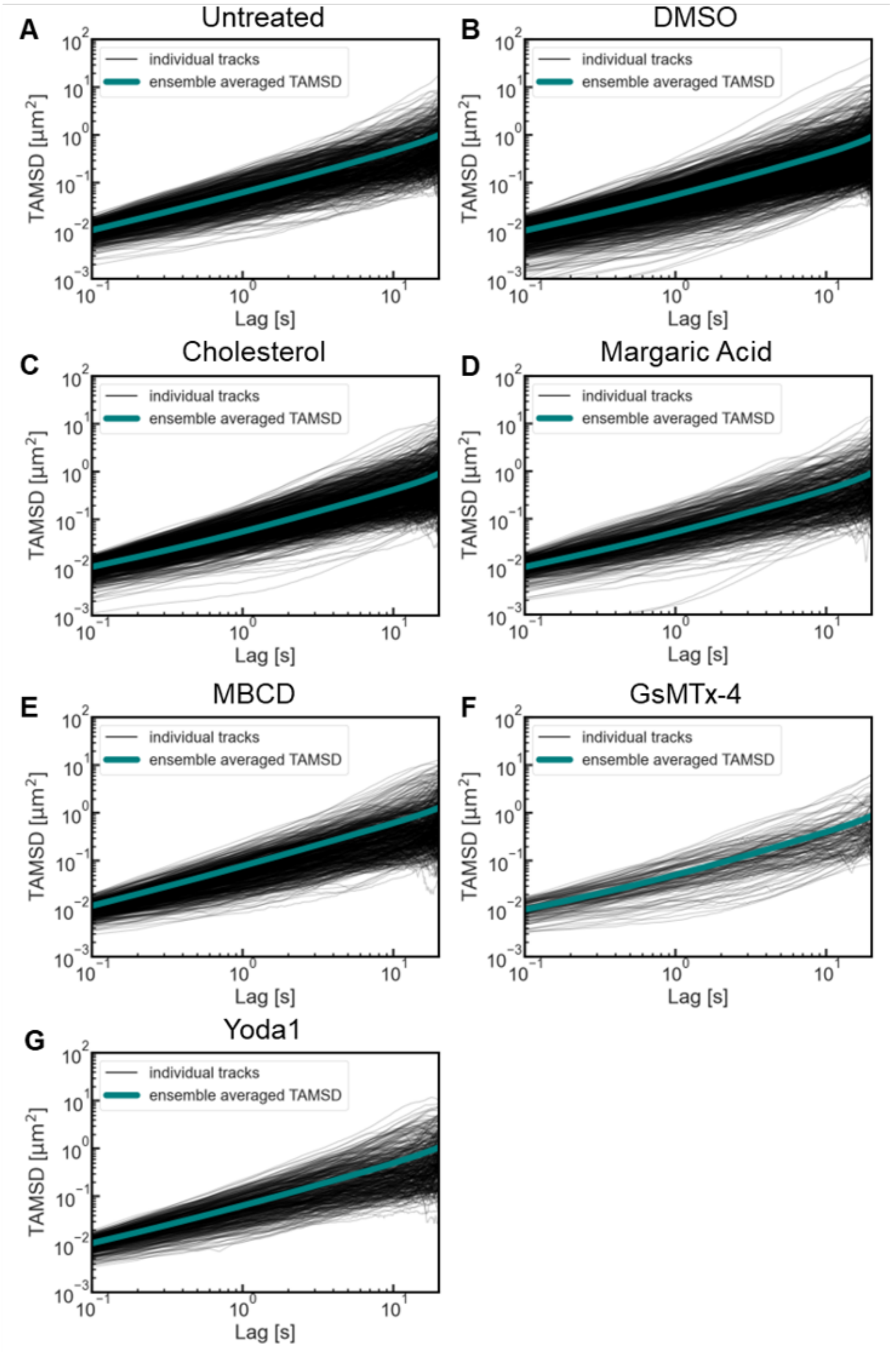

Supplementary Figure 4.10: TAMSD as a function of lag time of Piezo1-tdTomato expressed in MEFs (individual "mobile" trajectories, black; ensemble average, green). A. Untreated MEFs (also shown in Fig.4.4A). B. DMSO-treated. C. 100 µg/mL cholesterol-MBCD-treated. D. 150 µM margaric acid-treated E. 10 mM MBCD-treated. F. 4 µM GsMTx-4-treated and G. 4 µM Yoda1-treated.

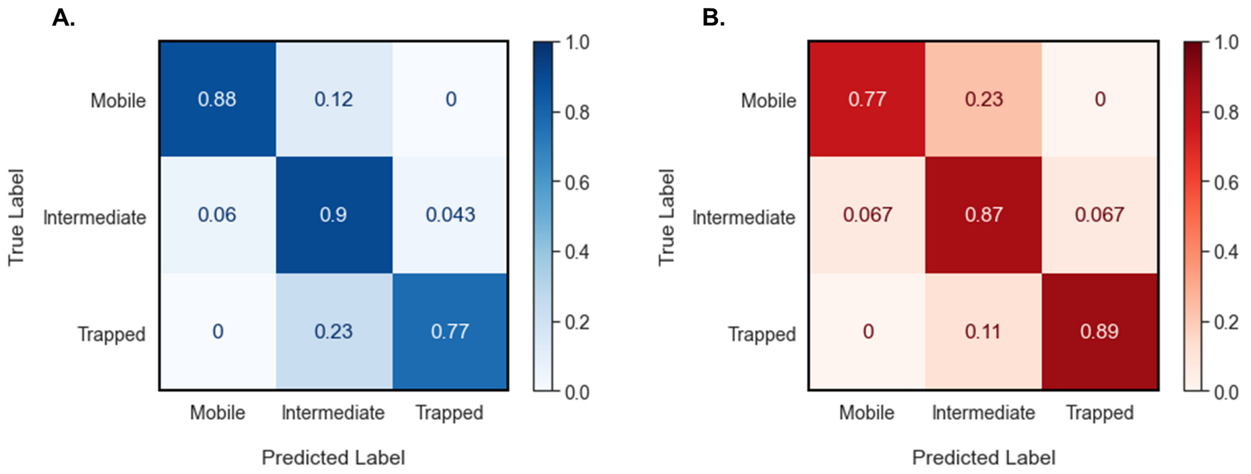

Supplementary Figure 4.11: SVM performance evaluation via confusion matrices. Confusion matrices for testing (A), and training data (B) show adequate separation between classes with an average F1-score of 0.87.

Bibliography

[1] A. Abu-Arish, E. Pandzic, J. Goepp, E. Matthes, J. W. Hanrahan, and P. W. Wiseman. Cholesterol modulates CFTR confinement in the plasma membrane of primary epithelial cells. *Biophys. J.*, 109(1):85–94, July 2015.

[2] E. M. Adkins, D. J. Samuvel, J. U. Fog, J. Eriksen, L. D. Jayanthi, C. B. Vaegter, S. Ramamoorthy, and U. Gether. Membrane Mobility and Microdomain Association of the Dopamine Transporter Studied with Fluorescence Correlation Spectroscopy and Fluorescence Recovery after Photobleaching. *ACS Biochemistry*, 46(37):10484–10497, August 2007.

[3] O. A. Andreev, A. D. Dupuy, M. Segala, S. Sandugu, D. A. Serra, C. O. Chichester, D. M. Engelman, and Y. K. Reshetnyak. Mechanism and uses of a membrane peptide that targets tumors and other acidic tissues in vivo. *Proceedings of the National Academy of Sciences of the United States of America*, 104(19):7893, may 2007.

[4] O. A. Andreev, D. M. Engelman, and Y. K. Reshetnyak. Targeting diseased tissues by pHLIP insertion at low cell surface pH. *Frontiers in physiology*, 5, 2014.

[5] O. A. Andreev, A. G. Karabadzhak, D. Weerakkody, G. O. Andreev, D. M. Engelman, and Y. K. Reshetnyak. pH (low) insertion peptide (pHLIP) inserts across a lipid bilayer as a helix and exits by a different path. *Proceedings of the National Academy of Sciences of the United States of America*, 107(9):4081–4086, mar 2010.

[6] A. Anemone, L. Consolino, L. Conti, P. Irrera, M. Y. Hsu, D. Villano, W. Dastrù, P. E. Porporato, F. Cavallo, and D. L. Longo. Tumour acidosis evaluated in vivo by MRI-CEST pH imaging reveals breast cancer metastatic potential. *British Journal of Cancer 2020 124:1*, 124(1):207–216, dec 2020.

[7] C. Bae, F. Sachs, and P. A. Gottlieb. The mechanosensitive ion channel Piezo1 is inhibited by the peptide GsMTx4. *Biochemistry*, 50(29):6295–6300, jul 2011.

[8] D. M. Bailey, M. A. Catron, O. Kovtun, R. L. Macdonald, Q. Zhang, and S. J. Rosenthal. Single Quantum Dot Tracking Reveals Serotonin Transporter Diffusion Dynamics are Correlated with Cholesterol-Sensitive Threonine 276 Phosphorylation Status in Primary Midbrain Neurons. *ACS Chem. Neurosci*, 9(11):2534–2541, May 2018.

[9] F. N. Barrera, J. Fendos, and D. M. Engelman. Membrane physical properties influence transmembrane helix formation. *Proceedings of the National Academy of Sciences of the United States of America*, 109(36):14422–14427, sep 2012.

[10] R. B. Best, X. Zhu, J. Shim, P. E. Lopes, J. Mittal, M. Feig, and A. D. MacKerell. Optimization of the additive CHARMM all-atom protein force field targeting improved sampling of the backbone ϕ, ψ and side-chain $\chi 1$ and $\chi 2$ Dihedral Angles. *Journal of Chemical Theory and Computation*, 8(9):3257–3273, sep 2012.

[11] L. P. Billen, C. L. Kokoski, J. F. Lovell, B. Leber, and D. W. Andrews. Bcl-XL inhibits membrane permeabilization by competing with Bax. *PLoS Biology*, 6(6):1268–1280, jun 2008.

[12] C. Bogner, B. Leber, and D. W. Andrews. Apoptosis: Embedded in membranes, dec 2010.

[13] A. Bohórquez-Hernández, E. Gratton, J. Pacheco, A. Asanov, and L. Vaca. Cholesterol modulates the cellular localization of orai1 channels and its disposition among membrane domains. *Biochim. Biophys. Acta*, 1862(12):1481–1490, Dec. 2017.

[14] W. M. Botello-Smith, W. Jiang, H. Zhang, A. D. Ozkan, Y.-C. Lin, C. N. Pham, J. J. Lacroix, and Y. Luo. A mechanism for the activation of the mechanosensitive piezo1 channel by the small molecule yoda1. *Nat. Commun.*, 10(1):4503, Oct. 2019.

[15] G. E. P. Box and D. R. Cox. An analysis of transformations. *J. R. Stat. Soc. Series B Stat. Methodol.*, 26(2):211–243, July 1964.

[16] J. Bürck, P. Wadhwani, S. Fanghänel, and A. S. Ulrich. Oriented Circular Dichroism: A Method to Characterize Membrane-Active Peptides in Oriented Lipid Bilayers. *Accounts of chemical research*, 49(2):184–192, feb 2016.

[17] V. Burns and B. Mertz. Using Simulation to Understand the Role of Titration on the Stability of a Peptide-Lipid Bilayer Complex. *Langmuir : the ACS journal of surfaces and colloids*, 36(41):12272–12280, oct 2020.

[18] J. R. Casey, S. Grinstein, and J. Orlowski. Sensors and regulators of intracellular pH, jan 2010.

[19] C. J. Cheng, R. Bahal, I. A. Babar, Z. Pincus, F. Barrera, C. Liu, A. Svoronos, D. T. Braddock, P. M. Glazer, D. M. Engelman, W. M. Saltzman, and F. J. Slack. MicroRNA silencing for cancer therapy targeted to the tumor microenvironment. *Nature*, 518(7537):107, feb 2015.

[20] A. T. Chesler, M. Szczot, D. Bharucha-Goebel, M. Čeko, S. Donkervoort, C. Laubacher, L. H. Hayes, K. Alter, C. Zampieri, C. Stanley, A. M. Innes, J. K. Mah, C. M. Grosmann, N. Bradley, D. Nguyen, A. R. Foley, C. E. Le Pichon, and C. G. Bönnemann. The Role of PIEZO2 in Human Mechanosensation. *N. Engl. J. Med.*, 375(14):1355–1364, October 2016.

[21] X. Chi, J. Kale, B. Leber, and D. W. Andrews. Regulating cell death at, on, and in membranes, sep 2014.

[22] A. Chimento, I. Casaburi, P. Avena, F. Trotta, A. De Luca, V. Rago, V. Pezzi, and R. Sirianni. Cholesterol and Its Metabolites in Tumor Growth: Therapeutic Potential of Statins in Cancer Treatment. *Frontiers in endocrinology*, 9(JAN), 2019.

[23] K. Cosentino and A. J. García-Sáez. Mitochondrial alterations in apoptosis, 2014.

[24] B. Coste, J. Mathur, M. Schmidt, T. J. Earley, S. Ranade, M. J. Petrus, A. E. Dubin, and A. Patapoutian. Piezo1 and piezo2 are essential components of distinct mechanically activated cation channels. *Science*, 330(6000):55–60, Oct. 2010.

[25] C. D. Cox, C. Bae, L. Ziegler, S. Hartley, V. Nikolova-Krstevski, P. R. Rohde, C.-A. Ng, F. Sachs, P. A. Gottlieb, and B. Martinac. Removal of the mechanoprotective influence of the cytoskeleton reveals PIEZO1 is gated by bilayer tension. *Nat. Commun.*, 7(1):10366, Jan. 2016.

[26] T. Crawford, A. Moshnikova, S. Roles, D. Weerakkody, M. DuPont, L. M. Carter, J. Shen, D. M. Engelman, J. S. Lewis, O. A. Andreev, and Y. K. Reshetnyak. pHLIP ICG for delineation of tumors and blood flow during fluorescence-guided surgery. *Scientific reports*, 10(1), dec 2020.

[27] M. Crimi and M. D. Esposti. Apoptosis-induced changes in mitochondrial lipids, apr 2011.

[28] I. M. Cristea and M. Degli Esposti. Membrane lipids and cell death: An overview, may 2004.

[29] M. Damaghi, J. W. Wojtkowiak, and R. J. Gillies. pH sensing and regulation in cancer. *Frontiers in physiology*, 4, 2013.

[30] T. Darden, D. York, and L. Pedersen. Particle mesh Ewald: An N·log(N) method for Ewald sums in large systems. *The Journal of Chemical Physics*, 98(12):10089–10092, 1993.

[31] V. Digiesi, R. Bandinelli, P. Bisceglie, and E. Santoro. Magnesium in tumoral tissues, in the muscle and serum of subjects suffering from neoplasia. *Biochemical medicine*, 29(3):360–363, 1983.

[32] J. Ding, B. H. Mooers, Z. Zhang, J. Kale, D. Falcone, J. McNichol, B. Huang, X. C. Zhang, C. Xing, D. W. Andrews, and J. Lin. After Embedding in membranes antiapoptotic bcl-xl protein binds both bcl-2 homology region 3 and helix 1 of proapoptotic bax protein to inhibit apoptotic mitochondrial permeabilization. *Journal of Biological Chemistry*, 289(17):11873–11896, apr 2014.

[33] F. W. Eckardt R, Carstens E. [Synthesis of new beta 1-receptor blockaders]. *Pharmazie*, 10(Oct 30):633–637, 1975.

[34] A. Edelstein, N. Amodaj, K. Hoover, R. Vale, and N. Stuurman. Computer control of microscopes using μmanager. *Curr. Protoc. Mol. Biol.*, 92(1):14.20.1—14.20.17, Oct. 2010.

[35] K. L. Ellefsen, J. R. Holt, A. C. Chang, J. L. Nourse, J. Arulmoli, A. H. Mekhdjian, H. Abuwarda, F. Tombola, L. A. Flanagan, A. R. Dunn, I. Parker, and M. M. Pathak. Myosin-II mediated traction forces evoke localized piezo1-dependent ca2 flickers. *Commun. Biol.*, 2(1):298, Aug. 2019.

[36] K. L. Ellefsen, B. Settle, I. Parker, and I. F. Smith. An algorithm for automated detection, localization and measurement of local calcium signals from camera-based imaging. *Cell Calcium*, 56(3):147–156, Sept. 2014.

[37] U. Essmann, L. Perera, M. L. Berkowitz, T. Darden, H. Lee, and L. G. Pedersen. A smooth particle mesh Ewald method. *The Journal of Chemical Physics*, 103(19):8577–8593, 1995.

[38] S. E. Feller, Y. Zhang, R. W. Pastor, and B. R. Brooks. Constant pressure molecular dynamics simulation: The Langevin piston method. *The Journal of Chemical Physics*, 103(11):4613–4621, 1995.

[39] J. Fendos, F. N. Barrera, and D. M. Engelman. Aspartate embedding depth affects pHLIP's insertion pKa. *Biochemistry*, 52(27):4595–4604, jul 2013.

[40] J. Ge, W. Li, Z. Qiancheng, N. Li, M. Chen, P. Zhi, R. Li, N. Gao, B. Xiao, and M. Yang. Architecture of the mammalian mechanosensitive Piezo1 channel. *Nature*, 527(7576):64–69, September 2015.

[41] L. A. Gillies and T. Kuwana. Apoptosis regulation at the mitochondrial outer membrane. *Journal of Cellular Biochemistry*, 115(4):632–640, 2014.

[42] R. Gnanasambandam, C. Ghatak, A. Yasmann, K. Nishizawa, F. Sachs, A. S. Ladokhin, S. I. Sukharev, and T. M. Suchyna. GsMTx4: Mechanism of inhibiting mechanosensitive ion channels. *Biophys. J.*, 112(1):31–45, Jan. 2017.

[43] Y. Golan and E. Sherman. Resolving mixed mechanisms of protein subdiffusion at the T cell plasma membrane. *Nat. Commun.*, 8(1):1–15, jun 2017.

[44] N. Granik, L. E. Weiss, E. Nehme, M. Levin, M. Chein, E. Perlson, Y. Roichman, and Y. Shechtman. Single-particle diffusion characterization by deep learning. *Biophys. J.*, 117(2):185–192, jul 2019.

[45] H. GrubmüLler, H. Heller, A. Windemuth, and K. Schulten. Generalized verlet algorithm for efficient molecular dynamics simulations with long-range interactions. *Molecular Simulation*, 6(1-3):121–142, 1991.

[46] S. A. Gudipaty, J. Lindblom, P. D. Loftus, M. J. Redd, K. Edes, C. F. Davey, V. Krishnegowda, and J. Rosenblatt. A Feedforward Mechanism Mediated by Mechanosensitive Ion Channel PIEZO1 and Tissue Mechanics Promotes Glioma Aggression. *Neuron*, 100(4):799–815.e7, November 2018.

[47] Y. R. Guo and R. MacKinnon. Structure-based membrane dome mechanism for piezo mechanosensitivity. *eLife*, 6:e33660, Dec. 2017.

[48] S. Z. Hanz, N. S. Shu, J. Qian, N. Christman, P. Kranz, M. An, C. Grewer, and W. Qiang. Protonation-Driven Membrane Insertion of a pH-Low Insertion Peptide. *Angewandte Chemie (International ed. in English)*, 55(40):12376–12381, sep 2016.

[49] C. R. Harris, K. J. Millman, S. J. van der Walt, R. Gommers, P. Virtanen, D. Cournapeau, E. Wieser, J. Taylor, S. Berg, N. J. Smith, R. Kern, M. Picus, S. Hoyer, M. H. van Kerkwijk, M. Brett, A. Haldane, J. F. del Río, M. Wiebe, P. Peterson, P. Gérard-Marchant, K. Sheppard, T. Reddy, W. Weckesser, H. Abbasi, C. Gohlke, and T. E. Oliphant. Array programming with NumPy. *Nature*, 585(7825):357–362, sep 2020.

[50] C. A. Haselwandter and R. MacKinnon. Piezo's membrane footprint and its contribution to mechanosensitivity. *eLife*, 7:e41968, Nov. 2018.

[51] A. I. Hashim, X. Zhang, J. W. Wojtkowiak, G. V. Martinez, and R. J. Gillies. Imaging pH and metastasis. *NMR in biomedicine*, 24(6):582–591, jul 2011.

[52] W. He, H. Song, Y. Su, L. Geng, B. J. Ackerson, H. B. Peng, and P. Tong. Dynamic heterogeneity and non-gaussian statistics for acetylcholine receptors on live cell membrane. *Nat. Comm.*, 7(1), May 2016.

[53] J. A. Helmuth, C. J. Burckhardt, P. Koumoutsakos, U. F. Greber, and I. F. Sbalzarini. A novel supervised trajectory segmentation algorithm identifies distinct types of human adenovirus motion in host cells. *J. Struct. Biol.*, 159(3):347–358, sep 2007.

[54] R. Z. Hill, M. C. Loud, A. E. Dubin, B. Peet, and A. Patapoutian. PIEZO1 transduces mechanical itch in mice. *Nature*, 607(7917):104–110, June 2022.

[55] F. Höfling and T. Franosch. Anomalous transport in the crowded world of biological cells. *Rep. Prog. Phys.*, 76(4):046602, Mar. 2013.

[56] J. R. Holt, W.-Z. Zeng, E. L. Evans, S.-H. Woo, S. Ma, H. Abuwarda, M. Loud, A. Patapoutian, and M. M. Pathak. Spatiotemporal dynamics of PIEZO1 localization controls keratinocyte migration during wound healing. *eLife*, 10:e65415, Sept. 2021.

[57] J. Huang, S. Rauscher, G. Nawrocki, T. Ran, M. Feig, B. L. De Groot, H. Grubmüller, and A. D. MacKerell. CHARMM36m: an improved force field for folded and intrinsically disordered proteins. *Nature methods*, 14(1):71–73, dec 2017.

[58] W. Humphrey, A. Dalke, and K. Schulten. VMD: Visual molecular dynamics. *Journal of Molecular Graphics*, 14(1):33–38, feb 1996.

[59] J. F. Hunt, P. Rath, K. J. Rothschild, and D. M. Engelman. Spontaneous, pH-dependent membrane insertion of a transbilayer alpha-helix. *Biochemistry*, 36(49):15177–15192, dec 1997.

[60] J. D. Hunter. Matplotlib: A 2d graphics environment. *Comput. Sci. Eng.*, 9(3):90–95, 2007.

[61] K. Jacobson, P. Liu, and B. C. Lagerholm. The lateral organization and mobility of plasma membrane components. *Cell*, 177(4):806–819, May 2019.

[62] K. Jacobson, E. D. Sheets, and R. Simson. Revisiting the fluid mosaic model of membranes. *Science*, 268(5216):1441–1442, June 1995.

[63] G. James, D. Witten, T. Hastie, and R. Tibshirani. Statistical learning. In *Springer Texts in Statistics*, pages 15–57. Springer US, 2021.

[64] J. Janczura, P. Kowalek, H. Loch-Olszewska, J. Szwabiński, and A. Weron. Classification of particle trajectories in living cells: Machine learning versus statistical testing hypothesis for fractional anomalous diffusion. *Phys. Rev. E*, 102(3):032402, sep 2020.

[65] N. Jankovsky, A. Caulier, J. Demagny, C. Guitton, S. Djordjevic, D. Lebon, H. Ouled-Haddou, V. Picard, and L. Garçon. Recent advances in the pathophysiology of PIEZO1-related hereditary xerocytosis. *Am. J. Hematol.*, 96(8):1017–1026, May 2021.

[66] S. Jo, X. Cheng, S. M. Islam, L. Huang, H. Rui, A. Zhu, H. S. Lee, Y. Qi, W. Han, K. Vanommeslaeghe, A. D. MacKerell, B. Roux, and W. Im. CHARMM-GUI PDB manipulator for advanced modeling and simulations of proteins containing nonstandard residues. In *Advances in Protein Chemistry and Structural Biology*, volume 96, pages 235–265. Academic Press Inc., jan 2014.

[67] S. Jo, T. Kim, V. G. Iyer, and W. Im. CHARMM-GUI: A web-based graphical user interface for CHARMM. *Journal of Computational Chemistry*, 29(11):1859–1865, aug 2008.

[68] S. Jo, J. B. Lim, J. B. Klauda, and W. Im. CHARMM-GUI membrane builder for mixed bilayers and its application to yeast membranes. *Biophysical Journal*, 97(1):50–58, jul 2009.

[69] W. L. Jorgensen, J. Chandrasekhar, J. D. Madura, R. W. Impey, and M. L. Klein. Comparison of simple potential functions for simulating liquid water. *The Journal of Chemical Physics*, 79(2):926–935, aug 1983.

[70] J. Kale, E. J. Osterlund, and D. W. Andrews. BCL-2 family proteins: Changing partners in the dance towards death, 2018.

[71] A. G. Karabadzhak, D. Weerakkody, D. Wijesinghe, M. S. Thakur, D. M. Engelman, O. A. Andreev, V. S. Markin, and Y. K. Reshetnyak. Modulation of the pHLIP transmembrane helix insertion pathway. *Biophysical journal*, 102(8):1846–1855, apr 2012.

[72] M. J. Katz and E. B. George. Fractals and the analysis of growth paths. *Bull. Math. Biol.*, 47(2):273–286, Mar. 1985.

[73] E. Kepten, I. Bronshtein, and Y. Garini. Improved estimation of anomalous diffusion exponents in single-particle tracking experiments. *Phys. Rev. E*, 87(5):052713, may 2013.

[74] J. B. Klauda, R. M. Venable, J. A. Freites, J. W. O'Connor, D. J. Tobias, C. Mondragon-Ramirez, I. Vorobyov, A. D. MacKerell, and R. W. Pastor. Update of the CHARMM All-Atom Additive Force Field for Lipids: Validation on Six Lipid Types. *Journal of Physical Chemistry B*, 114(23):7830–7843, jun 2010.

[75] P. Kowalek, H. Loch-Olszewska, and J. S. Szwabi´nski. Classification of diffusion modes in single-particle tracking data: Feature-based versus deep-learning approach. *Phys. Rev. E*, 100:32410, 2019.

[76] A. Kyrychenko, V. Vasquez-Montes, M. B. Ulmschneider, and A. S. Ladokhin. Lipid headgroups modulate membrane insertion of pHLIP peptide. *Biophysical journal*, 108(4):791–794, feb 2015.

[77] A. S. Ladokhin. Distribution analysis of depth-dependent fluorescence quenching in membranes: a practical guide. *Methods in enzymology*, 278:462–473, 1997.

[78] A. S. Ladokhin. Measuring membrane penetration with depth-dependent fluorescence quenching: Distribution analysis is coming of age. *Biochimica et Biophysica Acta (BBA) - Biomembranes*, 1838(9):2289–2295, sep 2014.

[79] A. S. Ladokhin, S. Jayasinghe, and S. H. White. How to measure and analyze tryptophan fluorescence in membranes properly, and why bother? *Analytical biochemistry*, 285(2):235–245, oct 2000.

[80] A. S. Ladokhin, A. Kyrychenko, M. V. Rodnin, and V. Vasquez-Montes. Conformational switching, refolding and membrane insertion of the diphtheria toxin translocation domain. *Methods in enzymology*, 649:341, jan 2021.

[81] A. S. Ladokhin and S. H. White. Folding of amphipathic α-helices on membranes: Energetics of helix formation by melittin. *Journal of Molecular Biology*, 285(4):1363–1369, jan 1999.

[82] B. Leber, J. Lin, and D. W. Andrews. Embedded together: The life and death consequences of interaction of the Bcl-2 family with membranes, may 2007.

[83] J. Lee, D. S. Patel, J. Ståhle, S. J. Park, N. R. Kern, S. Kim, J. Lee, X. Cheng, M. A. Valvano, O. Holst, Y. A. Knirel, Y. Qi, S. Jo, J. B. Klauda, G. Widmalm, and W. Im. CHARMM-GUI Membrane Builder for Complex Biological Membrane Simulations with Glycolipids and Lipoglycans. *Journal of chemical theory and computation*, 15(1):775–786, jan 2019.

[84] A. H. Lewis and J. Grandl. Mechanical sensitivity of piezo1 ion channels can be tuned by cellular membrane tension. *eLife*, 4:e12088, Dec. 2015.

[85] J. Li, B. Hou, S. Tumova, K. Muraki, A. Bruns, M. J. Ludlow, A. Sedo, A. J. Hyman, L. McKeown, R. S. Young, N. Y. Yoldasheva, Y. Majeed, L. A. Wilson, B. Rode, M. A. Bailey, H. R. Kim, Z. Fu, D. A. L. Carter, J. Bilton, H. Imrie, P. Ajuh, T. N. Dear, R. M. Cubbon, M. T. Kearney, K. R. Prasad, P. C. Evans, J. F. X. Ainscough, and D. J. Beech. Piezo1 integration of vascular architecture with physiological force. *Nature*, 515(7526):279–282, August 2014.

[86] R. A. Lippert, C. Predescu, D. J. Ierardi, K. M. Mackenzie, M. P. Eastwood, R. O. Dror, and D. E. Shaw. Accurate and efficient integration for molecular dynamics simulations at constant temperature and pressure. *Journal of Chemical Physics*, 139(16), oct 2013.

[87] E. London. Microreview how bacterial protein toxins enter cells: the role of partial unfoiding in membrane translocation. *Molecular microbiology*, 6(22):3277–3282, 1992.

[88] V. Lukacs, J. Mathur, R. Mao, P. Bayrak-Toydemir, M. Procter, S. M. Cahalan, H. J. Kim, M. Bandell, N. Longo, R. W. Day, D. A. Stevenson, A. Patapoutian, and B. L. Krock. Impaired PIEZO1 function in patients with a novel autosomal recessive congenital lymphatic dysplasia. *Nat. Comm.*, 6(1):6:8329, Sept. 2015.

[89] D. S. Martin, M. B. Forstner, and J. A. Käs. Apparent subdiffusion inherent to single particle tracking. *Biophys. J.*, 83(4):2109–2117, Oct. 2002.

[90] J. C. Martinou and R. J. Youle. Mitochondria in Apoptosis: Bcl-2 Family Members and Mitochondrial Dynamics, jul 2011.

[91] G. J. Martyna, M. L. Klein, and M. Tuckerman. Nosé-Hoover chains: The canonical ensemble via continuous dynamics. *The Journal of Chemical Physics*, 97(4):2635–2643, 1992.

[92] G. J. Martyna, D. J. Tobias, and M. L. Klein. Constant pressure molecular dynamics algorithms. *The Journal of Chemical Physics*, 101(5):4177–4189, aug 1994.

[93] L. D. Mayer, M. J. Hope, and P. R. Cullis. Vesicles of variable sizes produced by a rapid extrusion procedure. *BBA - Biomembranes*, 858(1):161–168, jun 1986.

[94] R. Metzler, J.-H. Jeon, and A. Cherstvy. Non-brownian diffusion in lipid membranes: Experiments and simulations. *Biochim. Biophys. Acta*, 1858(10):2451–2467, Oct. 2016.

[95] T. Moldoveanu, A. V. Follis, R. W. Kriwacki, and D. R. Green. Many players in BCL-2 family affairs, mar 2014.

[96] N. Monnier, S.-M. Guo, M. Mori, J. He, P. Lénárt, and M. Bathe. Bayesian approach to MSD-based analysis of particle motion in live cells. *Biophys. J.*, 103(3):616–626, Aug. 2012.

[97] A. Mosqueira, P. A. Camino, and F. J. Barrantes. Cholesterol modulates acetylcholine receptor diffusion by tuning confinement sojourns and nanocluster stability. *Sci. Rep.*, 8(1), Aug. 2018.

[98] S. W. Muchmore, M. Sattler, H. Liang, R. P. Meadows, J. E. Harlan, H. S. Yoon, D. Nettesheim, B. S. Chang, C. B. Thompson, S. L. Wong, S. C. Ng, and S. W. Fesik. X-ray and NMR structure of human Bcl-xL, an inhibitor of programmed cell death. *Nature*, 381(6580):335–341, may 1996.

[99] G. Muñoz-Gil, M. A. Garcia-March, C. Manzo, J. D. Martín-Guerrero, and M. Lewenstein. Single trajectory characterization via machine learning. *New J. Phys.*, 22(1):013010, jan 2020.

[100] S. E. Murthy, M. C. Loud, I. Daou, K. L. Marshall, F. Schwaller, J. Kühnemund, A. G. Francisco, W. T. Keenan, A. E. Dubin, G. R. Lewin, and A. Patapoutian. The mechanosensitive ion channel Piezo2 mediates sensitivity to mechanical pain in mice. *Sci. Transl. Med.*, 10(462):aat9897, October 2018.

[101] M. Musial-Siwek, A. Karabadzhak, O. A. Andreev, Y. K. Reshetnyak, and D. M. Engelman. Tuning the insertion properties of pHLIP. *Physics Faculty Publications*, 1798(6):1041–1046, jan 2010.

[102] G. L. Nicolson. The fluid—mosaic model of membrane structure: Still relevant to understanding the structure, function and dynamics of biological membranes after more than 40years. *Biochim. Biophys. Acta*, 1838(6):1451–1466, June 2014.

[103] K. Nonomura, V. Lukacs, D. T. Sweet, L. M. Goddard, A. Kanie, T. Whitwam, S. S. Ranade, T. Fujimori, M. L. Kahn, and A. Patapoutian. Mechanically activated ion channel PIEZO1 is required for lymphatic valve formation. *Proc. Natl. Acad. Sci. U.S.A.*, 115(50):12817–12822, October 2018.

[104] S. A. Otieno, S. Z. Hanz, B. Chakravorty, A. Zhang, L. M. Klees, M. An, and W. Qiang. PH-dependent thermodynamic intermediates of pHLIP membrane insertion determined by solid-state NMR spectroscopy. *Proceedings of the National Academy of Sciences of the United States of America*, 115(48):12194–12199, nov 2018.

[105] C. N. Pace, G. R. Grimsley, and J. M. Scholtz. Protein Ionizable Groups: pK Values and Their Contribution to Protein Stability and Solubility *. *Journal of Biological Chemistry*, 284:13285–13289, 2009.

[106] S. Pahari, L. Sun, and E. Alexov. Database tool Database tool PKAD: a database of experimentally measured pKa values of ionizable groups in proteins: a database of experimentally measured pKa values of ionizable groups in proteins. *The Journal of Biological Databases and Curation*, 2019:1–7, 2019.

[107] M. M. Pathak, J. L. Nourse, T. Tran, J. Hwe, J. Arulmoli, D. T. T. Le, E. Bernardis, L. A. Flanagan, and F. Tombola. Stretch-activated ion channel piezo1 directs lineage choice in human neural stem cells. *Proc. Natl. Acad. Sci. U.S.A.*, 111(45):16148–16153, Oct. 2014.

[108] F. Pedregosa, G. Varoquaux, A. Gramfort, V. Michel, B. Thirion, O. Grisel, M. Blondel, P. Prettenhofer, R. Weiss, V. Dubourg, J. Vanderplas, A. Passos, D. Cournapeau,

M. Brucher, M. Perrot, and D. Édouardand. Scikit-learn: Machine Learning in Python. *J. Mach. Learn. Res.*, 12:2825–2830, 2011.

[109] M. D. Peraro and F. G. Van Der Goot. Pore-forming toxins: Ancient, but never really out of fashion. *Nature Reviews Microbiology*, 14(2):77–92, feb 2016.

[110] J. C. Phillips, R. Braun, W. Wang, J. Gumbart, E. Tajkhorshid, E. Villa, C. Chipot, R. D. Skeel, L. Kalé, and K. Schulten. Scalable molecular dynamics with NAMD, 2005.

[111] H. D. Pinholt, S. S. Bohr, J. F. Iversen, W. Boomsma, and N. S. Hatzakis. Single-particle diffusional fingerprinting: A machine-learning framework for quantitative analysis of heterogeneous diffusion. *Proc. Natl. Acad. Sci. U.S.A.*, 118(31):e2104624118, aug 2021.

[112] N. Popgeorgiev, L. Jabbour, and G. Gillet. Subcellular localization and dynamics of the Bcl-2 family of proteins, feb 2018.

[113] Y. Qi, X. Cheng, J. Lee, J. V. Vermaas, T. V. Pogorelov, E. Tajkhorshid, S. Park, J. B. Klauda, and W. Im. CHARMM-GUI HMMM Builder for Membrane Simulations with the Highly Mobile Membrane-Mimetic Model, nov 2015.

[114] V. Rajani, G. Carrero, D. E. Golan, G. de Vries, and C. W. Cairo. Analysis of molecular diffusion by first-passage time variance identifies the size of confinement zones. *Biophys. J.*, 100(6):1463–1472, Mar. 2011.

[115] K. Raltchev, J. Pipercevic, and F. Hagn. Production and Structural Analysis of Membrane-Anchored Proteins in Phospholipid Nanodiscs. *Chemistry - A European Journal*, 24(21):5493–5499, apr 2018.

[116] S. S. Ranade, Z. Qiu, S.-H. Woo, S. S. Hur, S. E. Murthy, S. M. Cahalan, J. Xu, J. Mathur, M. Bandell, B. Coste, Y.-S. J. Li, S. Chien, and A. Patapoutian. Piezo1, a mechanically activated ion channel, is required for vascular development in mice. *Proc. Natl. Acad. Sci. U.S.A.*, 111(28):10347–10352, June 2014.

[117] S. S. Ranade, S.-H. Woo, A. E. Dubin, R. A. Moshourab, C. Wetzel, M. Petrus, J. Mathur, V. Bégay, B. Coste, J. Mainquist, A. J. Wilson, A. G. Francisco, K. Reddy, Z. Qiu, J. N. Wood, G. R. Lewin, and A. Patapoutian. Piezo2 is the major transducer of mechanical forces for touch sensation in mice. *Nature*, 516(7529):121–125, December 2014.

[118] Y. K. Reshetnyak, O. A. Andreev, U. Lehnert, and D. M. Engelman. Translocation of molecules into cells by pH-dependent insertion of a transmembrane helix. *Proceedings of the National Academy of Sciences of the United States of America*, 103(17):6460–6465, apr 2006.

[119] Y. K. Reshetnyak, O. A. Andreev, M. Segala, V. S. Markin, and D. M. Engelman. Energetics of peptide (pHLIP) binding to and folding across a lipid bilayer membrane. *Proceedings of the National Academy of Sciences of the United States of America*, 105(40):15340–15345, oct 2008.

[120] Y. K. Reshetnyak, A. Moshnikova, O. A. Andreev, and D. M. Engelman. Targeting Acidic Diseased Tissues by pH-Triggered Membrane-Associated Peptide Folding. *Frontiers in Bioengineering and Biotechnology*, 8:335, apr 2020.

[121] Y. K. Reshetnyak, M. Segala, O. A. Andreev, and D. M. Engelman. No Title. *Biophysical Journal*, 93(7), 2007.

[122] P. Ridone, E. Pandzic, M. Vassalli, C. D. Cox, A. Macmillan, P. A. Gottlieb, and B. Martinac. Disruption of membrane cholesterol organization impairs the activity of PIEZO1 channel clusters. *J. Gen. Physiol.*, 152(8):e201912515, June 2020.

[123] S. Riedl, B. Rinner, M. Asslaber, H. Schaider, S. Walzer, A. Novak, K. Lohner, and D. Zweytick. In search of a novel target - phosphatidylserine exposed by non-apoptotic tumor cells and metastases of malignancies with poor treatment efficacy. *Biochimica et biophysica acta*, 1808(11):2638–2645, nov 2011.

[124] L. O. Romero, A. E. Massey, A. D. Mata-Daboin, F. J. Sierra-Valdez, S. C. Chauhan, J. F. Cordero-Morales, and V. Vásquez. Dietary fatty acids fine-tune piezo1 mechanical response. *Nat. Commun.*, 10(1):1200, Mar. 2019.

[125] J. P. Ryckaert, G. Ciccotti, and H. J. Berendsen. Numerical integration of the cartesian equations of motion of a system with constraints: molecular dynamics of n-alkanes. *Journal of Computational Physics*, 23(3):327–341, 1977.

[126] P. Ryzhov, Y. Tian, Y. Yao, A. A. Bobkov, W. Im, and F. M. Marassi. Conformational States of the Cytoprotective Protein Bcl-xL. *Biophysical Journal*, 119(7):1324–1334, oct 2020.

[127] K. Saotome, S. E. Murthy, J. M. Kefauver, T. Whitwam, A. Patapoutian, and A. B. Ward. Structure of the mechanically activated ion channel piezo1. *Nature*, 554(7693):481–486, Dec. 2017.

[128] M. J. Saxton. Lateral diffusion in an archipelago. Single-particle diffusion. *Biophys. J.*, 64(6):1766–1780, jun 1993.

[129] M. J. Saxton and K. Jacobson. SINGLE-PARTICLE TRACKING:applications to membrane dynamics. *Annu. Rev. Biophys. Biomol. Struct.*, 26(1):373–399, June 1997.

[130] H. L. Scott, F. A. Heberle, J. Katsaras, and F. N. Barrera. Phosphatidylserine Asymmetry Promotes the Membrane Insertion of a Transmembrane Helix. *Biophysical journal*, 116(8):1495–1506, apr 2019.

[131] E. Sezgin, I. Levental, S. Mayor, and C. Eggeling. The mystery of membrane organization: composition, regulation and roles of lipid rafts. *Nat. Rev. Mol. Cell Biol.*, 18(6):361–374, Mar. 2017.

[132] Y. Shan, J. L. Klepeis, M. P. Eastwood, R. O. Dror, and D. E. Shaw. Gaussian split Ewald: A fast Ewald mesh method for molecular simulation. *Journal of Chemical Physics*, 122(5), 2005.

[133] D. E. Shaw, J. P. Grossman, J. A. Bank, B. Batson, J. A. Butts, J. C. Chao, M. M. Deneroff, R. O. Dror, A. Even, C. H. Fenton, A. Forte, J. Gagliardo, G. Gill, B. Greskamp, C. R. Ho, D. J. Ierardi, L. Iserovich, J. S. Kuskin, R. H. Larson, T. Layman, L. S. Lee, A. K. Lerer, C. Li, D. Killebrew, K. M. Mackenzie, S. Y. H. Mok, M. A. Moraes, R. Mueller, L. J. Nociolo, J. L. Peticolas, T. Quan, D. Ramot, J. K. Salmon, D. P. Scarpazza, U. Ben Schafer, N. Siddique, C. W. Snyder, J. Spengler, P. T. P. Tang, M. Theobald, H. Toma, B. Towles, B. Vitale, S. C. Wang, and C. Young. Anton 2: Raising the Bar for Performance and Programmability in a Special-Purpose Molecular Dynamics Supercomputer. In *International Conference for High Performance Computing, Networking, Storage and Analysis, SC*, volume 2015, pages 41–53. IEEE Computer Society, jan 2014.

[134] H. Shen, L. J. Tauzin, R. Baiyasi, W. Wang, N. Moringo, B. Shuang, and C. F. Landes. Single Particle Tracking: From Theory to Biophysical Applications. *Chem. Rev.*, 117(11):7331–7376, jun 2017.

[135] N. S. Shu, M. S. Chung, L. Yao, M. An, and W. Qiang. Residue-specific structures and membrane locations of pH-low insertion peptide by solid-state nuclear magnetic resonance. *Nature Communications 2015 6:1*, 6(1):1–10, jul 2015.

[136] R. Simson, B. Yang, S. E. Moore, P. Doherty, F. S. Walsh, and K. A. Jacobson. Structural mosaicism on the submicron scale in the plasma membrane. *Biophys. J.*, 74(1):297–308, Jan. 1998.

[137] G. Slaybaugh, D. Weerakkody, D. M. Engelman, O. A. Andreev, and Y. K. Reshetnyak. Kinetics of pHLIP peptide insertion into and exit from a membrane. *Proceedings of the National Academy of Sciences of the United States of America*, 117(22), jun 2020.

[138] M. P. Stelling, J. M. Motta, M. Mashid, W. E. Johnson, M. S. Pavão, and N. P. Farrell. Metal ions and the extracellular matrix in tumor migration. *The FEBS journal*, 286(15):2950–2964, 2019.

[139] A. Strasser, S. Cory, and J. M. Adams. Deciphering the rules of programmed cell death to improve therapy of cancer and other diseases, sep 2011.

[140] Y. Subburaj, K. Cosentino, M. Axmann, E. Pedrueza-Villalmanzo, E. Hermann, S. Bleicken, J. Spatz, and A. J. García-Sáez. Bax monomers form dimer units in the membrane that further self-assemble into multiple oligomeric species. *Nature Communications*, 6, aug 2015.

[141] W. Sun, S. Chi, Y. Li, S. Ling, Y. Tan, Y. Xu, F. Jiang, J. Li, C. Liu, G. Zhong, D. Cao, X. Jin, D. Zhao, X. Gao, Z. Liu, B. Xiao, and Y. Li. The mechanosensitive piezo1 channel is required for bone formation. *eLife*, 8:e47454, July 2019.

[142] A. A. Svoronos, R. Bahal, M. C. Pereira, F. N. Barrera, J. C. Deacon, M. Bosenberg, D. Dimaio, P. M. Glazer, and D. M. Engelman. Tumor-Targeted, Cytoplasmic Delivery of Large, Polar Molecules Using a pH-Low Insertion Peptide. *Molecular pharmaceutics*, 17(2):461–471, feb 2020.

[143] R. Syeda, M. N. Florendo, C. D. Cox, J. M. Kefauver, J. S. Santos, B. Martinac, and A. Patapoutian. Piezo1 channels are inherently mechanosensitive. *Cell Rep.*, 17(7):1739–1746, Nov. 2016.

[144] R. Syeda, J. Xu, A. E. Dubin, B. Coste, J. Mathur, T. Huynh, J. Matzen, J. Lao, D. C. Tully, I. H. Engels, H. Michael Petrassi, A. M. Schumacher, M. Montal, M. Bandell, and A. Patapoutian. Chemical activation of the mechanotransduction channel Piezo1. *eLife*, 4:e07369, may 2015.

[145] M. Szczot, J. Liljencrantz, N. Ghitani, A. Barik, R. Lam, J. H. Thompson, D. Bharucha-Goebel, D. Saade, A. Necaise, S. Donkervoort, A. R. Foley, T. Gordon, L. Case, M. C. Bushnell, C. G. Bönnemann, and A. T. Chesler. PIEZO2 mediates injury-induced tactile pain in mice and humans. *Sci. Transl. Med.*, 10(462):eaat9892, October 2018.

[146] W. Szlasa, I. Zendran, A. Zalesińska, M. Tarek, and J. Kulbacka. Lipid composition of the cancer cell membrane. *Journal of bioenergetics and biomembranes*, 52(5):321–342, oct 2020.

[147] L. T. H. Tan, K. G. Chan, P. Pusparajah, W. L. Lee, L. H. Chuah, T. M. Khan, L. H. Lee, and B. H. Goh. Targeting membrane lipid a potential cancer cure? *Frontiers in Pharmacology*, 8(12):1–6, jan 2017.

[148] T. T. Tapmeier, A. Moshnikova, J. Beech, D. Allen, P. Kinchesh, S. Smart, A. Harris, A. McIntyre, D. M. Engelman, O. A. Andreev, Y. K. Reshetnyak, and R. J. Muschel. The pH low insertion peptide pHLIP Variant 3 as a novel marker of acidic malignant lesions. *Proceedings of the National Academy of Sciences of the United States of America*, 112(31):9710–9715, aug 2015.

[149] V. H. Teixeira, D. Vila-Viçosa, P. B. Reis, and M. MacHuqueiro. PKa Values of Titrable Amino Acids at the Water/Membrane Interface. *Journal of Chemical Theory and Computation*, 12(3):930–934, mar 2016.

[150] W. S. Trimble and S. Grinstein. Barriers to the free diffusion of proteins and lipids in the plasma membrane. *J. Cell Biol.*, 208(3):259–271, Feb. 2015.

[151] Y. Tsujimoto, J. Cossman, E. Jaffe, and C. M. Croce. Involvement of the bcl-2 gene in human follicular lymphoma. *Science*, 228(4706):1440–1443, jun 1985.

[152] M. Tuckerman, B. J. Berne, and G. J. Martyna. Reversible multiple time scale molecular dynamics. *The Journal of Chemical Physics*, 97(3):1990–2001, aug 1992.

[153] B. Ugarte-Uribe and A. J. García-Sáez. Apoptotic foci at mitochondria: In and around bax pores, jun 2017.

[154] T. Utsugi, A. J. Schroit, J. Connor, nD Bucana, and I. J. Fidler. Elevated Expression of Phosphatidylserine in the Outer Membrane Leaflet of Human Tumor Cells and Recognition by Activated Human Blood Monocytes1. *Cancer Research*, 1991.

[155] G. Vaisey, P. Banerjee, A. J. North, C. A. Haselwandter, and R. Mackinnon. Piezo1 as a force-through-membrane sensor in red blood cells. *bioRxiv*, Aug. 2022.

[156] C. Vander Linden and C. Corbet. Therapeutic Targeting of Cancer Stem Cells: Integrating and Exploiting the Acidic Niche. *Frontiers in oncology*, 9(MAR), 2019.

[157] V. Vasquez-Montes, J. Gerhart, K. E. King, D. Thévenin, and A. S. Ladokhin. Comparison of lipid-dependent bilayer insertion of pHLIP and its P20G variant. *Biochimica et biophysica acta. Biomembranes*, 1860(2):534–543, feb 2018.

[158] V. Vasquez-Montes, A. Kyrychenko, M. Vargas-Uribe, M. V. Rodnin, and A. S. Ladokhin. Conformational Switching in Bcl-xL: Enabling Non-Canonic Inhibition of Apoptosis Involves Multiple Intermediates and Lipid Interactions. *Cells*, 9(3):539, feb 2020.

[159] V. Vasquez-Montes, M. V. Rodnin, A. Kyrychenko, and A. S. Ladokhin. Lipids modulate the BH3-independent membrane targeting and activation of BAX and Bcl-xL. *Proceedings of the National Academy of Sciences of the United States of America*, 118(37), sep 2021.

[160] V. Vasquez-Montes, M. Vargas-Uribe, N. K. Pandey, M. V. Rodnin, R. Langen, and A. S. Ladokhin. Lipid-modulation of membrane insertion and refolding of the apoptotic inhibitor Bcl-xL, jul 2019.

[161] P. Virtanen, R. Gommers, T. E. Oliphant, M. Haberland, T. Reddy, D. Cournapeau, E. Burovski, P. Peterson, W. Weckesser, J. Bright, S. J. van der Walt, M. Brett, J. Wilson, K. J. Millman, N. Mayorov, A. R. J. Nelson, E. Jones, R. Kern, E. Larson, C. J. Carey, İ. Polat, Y. Feng, E. W. Moore, J. VanderPlas, D. Laxalde, J. Perktold, R. Cimrman, I. Henriksen, E. A. Quintero, C. R. Harris, A. M. Archibald, A. H. Ribeiro, F. Pedregosa, P. van Mulbregt, and SciPy 1.0 Contributors. SciPy 1.0: Fundamental Algorithms for Scientific Computing in Python. *Nat. Methods*, 17:261–272, 2020.

[162] T. Wagner, A. Kroll, C. R. Haramagatti, H. G. Lipinski, and M. Wiemann. Classification and segmentation of nanoparticle diffusion trajectories in cellular micro environments. *PLoS ONE*, 12(1):e0170165, jan 2017.

[163] C. Wang and R. J. Youle. The role of mitochondria in apoptosis, dec 2009.

[164] M. L. Waskom. seaborn: statistical data visualization. *J. Open Source Softw.*, 6(60):3021, 2021.

[165] D. Weerakkody, A. Moshnikova, M. S. Thakur, V. Moshnikova, J. Daniels, D. M. Engelman, O. A. Andreev, and Y. K. Reshetnyak. Family of pH (low) insertion peptides for tumor targeting. *Proceedings of the National Academy of Sciences of the United States of America*, 110(15):5834–5839, apr 2013.

[166] A. Weron, J. Janczura, E. Boryczka, T. Sungkaworn, and D. Calebiro. Statistical testing approach for fractional anomalous diffusion classification. *Phys. Rev. E*, 99(4), Apr. 2019.

[167] Wes McKinney. Data Structures for Statistical Computing in Python. In Stéfan van der Walt and Jarrod Millman, editors, *Proceedings of the 9th Python in Science Conference*, pages 56 – 61, 2010.

[168] J. M. White and G. R. Whittaker. Fusion of Enveloped Viruses in Endosomes. *Traffic (Copenhagen, Denmark)*, 17(6):593–614, jun 2016.

[169] T. D. Wijerathne, A. D. Ozkan, and J. J. Lacroix. Yoda1's energetic footprint on piezo1 channels and its modulation by voltage and temperature. *Proc. Natl. Acad. Sci. U.S.A.*, 119(29):e2202269119, July 2022.

[170] W. C. Wimley and S. H. White. Designing transmembrane alpha-helices that insert spontaneously. *Biochemistry*, 39(15):4432–4442, apr 2000.

[171] F. I. Wolf, J. A. Maier, A. Nasulewicz, C. Feillet-Coudray, M. Simonacci, A. Mazur, and A. Cittadini. Magnesium and neoplasia: from carcinogenesis to tumor growth and progression or treatment. *Archives of biochemistry and biophysics*, 458(1):24–32, feb 2007.

[172] S.-H. Woo, V. Lukacs, J. C. de Nooij, D. Zaytseva, C. R. Criddle, A. Francisco, T. M. Jessell, K. A. Wilkinson, and A. Patapoutian. Piezo2 is the principal mechanotransduction channel for proprioception. *Nat. Neurosci.*, 18(12):1756–1762, December 2015.

[173] E. L. Wu, X. Cheng, S. Jo, H. Rui, K. C. Song, E. M. Dávila-Contreras, Y. Qi, J. Lee, V. Monje-Galvan, R. M. Venable, J. B. Klauda, and W. Im. CHARMM-GUI membrane builder toward realistic biological membrane simulations, oct 2014.

[174] Y. Wu, H. W. Huang, and G. A. Olah. Method of oriented circular dichroism. *Biophysical journal*, 57(4):797–806, 1990.

[175] L. C. Wyatt, A. Moshnikova, T. Crawford, D. M. Engelman, O. A. Andreev, and Y. K. Reshetnyak. Peptides of pHLIP family for targeted intracellular and extracellular delivery of cargo molecules to tumors. *Proceedings of the National Academy of Sciences of the United States of America*, 115(12):E2811–E2818, mar 2018.

[176] M. Yao, A. Tijore, D. Cheng, J. V. Li, A. Harihan, B. Martinac, G. T. V. Nhieu, C. D. Cox, and M. Sheetz. Force-dependent recruitment of Piezo1 drives focal adhesion maturation and calcium entry in normal but not tumor cells. *bioRxiv*, aug 2022.

[177] Y. Yao, L. M. Fujimoto, N. Hirshman, A. A. Bobkov, A. Antignani, R. J. Youle, and F. M. Marassi. Conformation of BCL-XL upon membrane integration. *Journal of Molecular Biology*, 427(13):2262–2270, may 2015.

[178] Y. Yao and F. M. Marassi. Reconstitution and Characterization of BCL-2 Family Proteins in Lipid Bilayer Nanodiscs. In *Methods in Molecular Biology*, volume 1877, pages 233–246. Humana Press Inc., 2019.

[179] R. J. Youle and A. Strasser. The BCL-2 protein family: Opposing activities that mediate cell death, jan 2008.

[180] M. Zasloff. Antimicrobial peptides of multicellular organisms. *Nature 2002 415:6870*, 415(6870):389–395, jan 2002.

[181] W.-Z. Zeng, K. L. Marshall, S. Min, I. Daou, M. W. Chapleau, F. M. Abboud, S. D. Liberles, and A. Patapoutian. PIEZOs mediate neuronal sensing of blood pressure and the baroreceptor reflex. *Science*, 362(6413):464–467, October 2018.

[182] Q. Zhao, H. Zhou, S. Chi, Y. Wang, J. Wang, J. Geng, K. Wu, W. Liu, T. Zhang, M.-Q. Dong, J. Wang, X. Li, and B. Xiao. Structure and mechanogating mechanism of the Piezo1 channel. *Nature*, 554(7693):487–492, January 2018.

[183] Z. Zhao, C. Li, B. Song, J. Sun, X. Fu, F. Yang, H. Wang, and B. Yan. pH low insertion peptide mediated cell division cycle-associated protein 1 -siRNA transportation for prostatic cancer therapy targeted to the tumor microenvironment. *Biochemical and Biophysical Research Communications*, 503(3):1761–1767, sep 2018.

[184] R. F. Zwaal, P. Comfurius, and E. M. Bevers. Surface exposure of phosphatidylserine in pathological cells. *Cellular and molecular life sciences : CMLS*, 62(9):971–988, may 2005.